NAVAL POSTGRADUATE SCHOOL

Monterey, California

THESIS

EFFECT OF CANARD OSCILLATIONS ON THE
VORTICAL FLOWFIELD
OF A X-31A-LIKE FIGHTER AIRCRAFT MODEL

by

Liu, Da-Ming

March 1992

Thesis Advisor: S. K. Hebbar
Co-Advisor: M. F. Platzer

REPORT DOCUMENTATION PAGE

1a. REPORT SECURITY CLASSIFICATION	1b. RESTRICTIVE MARKINGS
2a. SECURITY CLASSIFICATION AUTHORITY	3. DISTRIBUTION/AVAILABILITY OF REPORT Approved for public release; distribution is unlimited.
2b. DECLASSIFICATION/DOWNGRADING SCHEDULE	
4. PERFORMING ORGANIZATION REPORT NUMBER(S)	5. MONITORING ORGANIZATION REPORT NUMBER(S)
6a. NAME OF PERFORMING ORGANIZATION Naval Postgraduate School; 6b. OFFICE SYMBOL (If applicable) AA	7a. NAME OF MONITORING ORGANIZATION Naval Postgraduate School
6c. ADDRESS (City, State, and ZIP Code) Monterey, CA 93943-5000	7b. ADDRESS (City, State, and ZIP Code) Monterey, CA 93943-5000
8a. NAME OF FUNDING/SPONSORING ORGANIZATION; 8b. OFFICE SYMBOL (If applicable)	9. PROCUREMENT INSTRUMENT IDENTIFICATION NUMBER
8c. ADDRESS (City, State, and ZIP Code)	10. SOURCE OF FUNDING NUMBERS: Program Element No. / Project No / Task No. / Work Unit Accession Number

11. TITLE (Include Security Classification)
Effect of Canard Oscillations on the Vortical Flowfield of a X-31A-like Fighter Aircraft Model.(Unclassified)

12. PERSONAL AUTHOR(S) Liu, Da-Ming

13a. TYPE OF REPORT	13b. TIME COVERED	14. DATE OF REPORT (year, month, day)	15. PAGE COUNT
Master's Thesis	From To	MARCH 1992	129

16. SUPPLEMENTARY NOTATION
The views expressed in this thesis are those of the author and do not reflect the official policy or position of the Department of Defense or the U.S. Government.

17. COSATI CODES

FIELD	GROUP	SUBGROUP

18. SUBJECT TERMS (continue on reverse if necessary and identify by block number)
High angle of attack aerodynamic, effect of pitch rate and canard oscillation s vortex breakdown , flow visualization by dye injection, X-31A-like fighter aircraft model

19. ABSTRACT (continue on reverse if necessary and identify by block number)
A flow visualization investigation was carried out in the Naval Postgraduate School water tunnel using dye injection technique to study the effects of oscillating a close-coupled canard on a 2.3% scale model of a X-31A-like fighter aircraft. This investigation focussed primarily on the effects of canard oscillations on the breakdown characteristics of the wing root vortex for both static and dynamic conditions of the model at zero sideslip angle. The main results of this first of a kind water tunnel visualization suggest that for the static conditions of the model the low frequency canard oscillations tend todestabilize/augment wing vortex core, i.e., promote/delay bursting of wing vortex. the dynamic tests indicate that the large amplitude low frequency oscillations of the canard interac favorably with the wing vortical flowfield to delay vortex bursting during both pitch-up and pitch-down motions.

20. DISTRIBUTION/AVAILABILITY OF ABSTRACT ☒ UNCLASSIFIED/UNLIMITED ☐ SAME AS REPORT ☐ DTIC USERS	21. ABSTRACT SECURITY CLASSIFICATION UNCLASSIFIED
22a. NAME OF RESPONSIBLE INDIVIDUAL S. K. Hebbar	22b. TELEPHONE (Include Area code) (408) 646-2997; 22c. OFFICE SYMBOL AA/HB

Effect of Canard Oscillations on the Vortical Flowfield of a X-31A-Like Fighter Aircraft Model

by

Liu, Da-Ming
Lieutenant Commander, R.O.C. Navy
B.S., Chung Cheng Institute of Technology ,1981

Submitted in partial fulfillment
of the requirements for the degree of

MASTER OF SCIENCE IN AERONAUTICAL ENGINEERING

from the

NAVAL POSTGRADUATE SCHOOL
March 1992

Author: Liu, Da-Ming (劉達明)
Liu, Da-Ming

Approved by:
S.K. Hebbar, Thesis Advisor

M. F. Platz
M.F. Platzer, Co-Advisor

Daniel J Collins
D. Collins, Chairman
Department of Aeronautics and Astronautics

ABSTRACT

A flow visualization investigation was carried out in the Naval Postgraduate School water tunnel using dye injection technique to study the effects of oscillating a close-coupled canard on a 2.3% scale model of a X-31A-like fighter aircraft. This investigation focussed primarily on the effects of canard oscillations on the breakdown characteristics of the wing root vortex for both static and dynamic conditions of the model at zero sideslip angle. The main results of this <u>first</u> of a kind water tunnel visualization data suggest that for the static conditions of the model the low frequency/ high frequency canard oscillations tend to destabilize/ augment wing vortex core, i.e., promote/ delay bursting of the wing vortex. The dynamic tests indicate that the large amplitude low frequency oscillations of the canard interact favorably with the wing vortical flowfield to delay vortex bursting during both pitch-up and pitch-down motions.

TABLE OF CONTENTS

ACKNOWLEDGEMENT

This thesis was sponsored by Naval Air System Command, the Naval Postgraduate School, and the Naval Air Development Center in support of ongoing investigation of canard-configured fighter aircraft model.

My gratitude goes to my thesis advisor, Professor S.K. Hebbar, and co-advisor, Professor M.F. Platzer, for their guidance, encouragement and patience throughout the course of this project.

I would like to thank the ROCNAVY for providing the opportunity to study at NPS.

I would also like to thank the many people at the Naval Postgraduate School who provided the services and expertise necessary for this reserach. In particular:

Mr. Al McGuire, Aeronautics & Astronautics Dept.

Mr. Mitch Nichols, Photo Lab

Mr. John Moulton, Aeronautics metal shop

Mr. Ron Ramaker, Aeronautics model shop

Mr. Jack King, Aeronautics Lab

Finally, I would like to take this opportunity to express my deepest gratitude to my wife Hui-Chiung for her encouragement and self sacrifice in support of my efforts.

I. INTRODUCTION

A. BACKGROUND

The canard configuration has become popular in the design of advanced combat aircraft since there can be significant aerodynamic advantages from such a layout. For a close-coupled canard there is a strong aerodynamic interaction between the canard and the wing which affects not only the longitudinal characteristics but may also influence the lateral and directional stability of the aircraft, especially at high angles of attack. Interaction between the flow around the forebody and the canard may also have a significant effect. Both these effects are likely to depend on the shape and the incidence of the canard [Ref.1].

There are actually two distinct classes of canard: the control-canard and the lifting canard (Fig.1). In the control-canard configuration, the wing carries most of the lift, and the canard is used primarily for control (as is an aft tail). In the United States, the Grumman X-29 aircraft and the Navy's X-31A research demonstrator aircraft use control-canards.

A lifting-canard configuration uses both the wing and the canard to provide lift under normal flight conditions. This requires that the aircraft center of gravity be well forward of the normal location with respect to the wing when compared to an aft-tailed aircraft. A lifting-canard will usually have a higher aspect ratio and greater airfoil camber than a control-canard, to reduce the canard's drag-due-to-lift. The SAAB Viggen, the

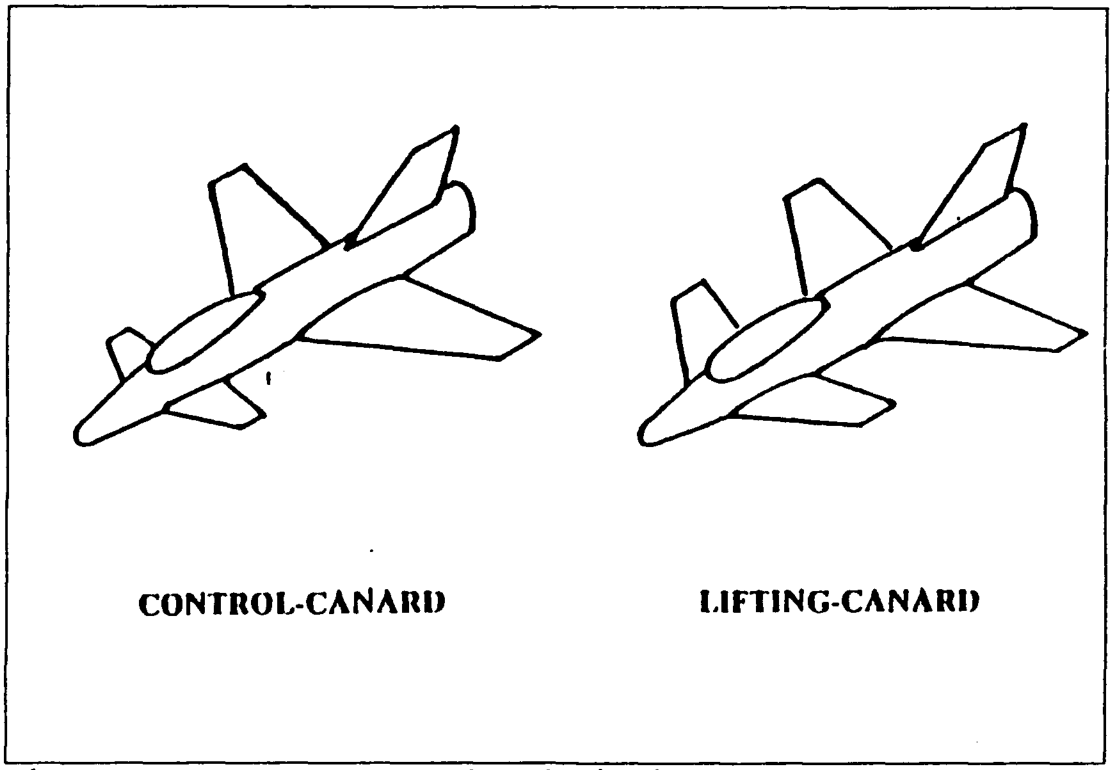

Figure 1. Control-Canard and Lifting-Canard

Israeli Lavi and the new European Fighter Aircraft EFA use lifting-canards.

The X-29 configuration is highly unstable in pitch with the canard included but is actually about neutral in stability with the canard off. This implies that the canard normally operates at nearly zero angle of attack, and thus carries little of the aircraft's weight. This is accomplished by a sophisticated, computerized flight control system that changes the angle of the canard in response to gusts.

Rockwell International Corporation and Messerschmitt-Boelkow-Blohm (MBB) designed and built the X-31A aircraft which uses movable canards. Its purpose is to demonstrate enhanced fighter maneuverability for the U.S. Navy (Fig.2). Test flights were begun in 1990, first at Rockwell's facilities and later at the Naval Air test center.

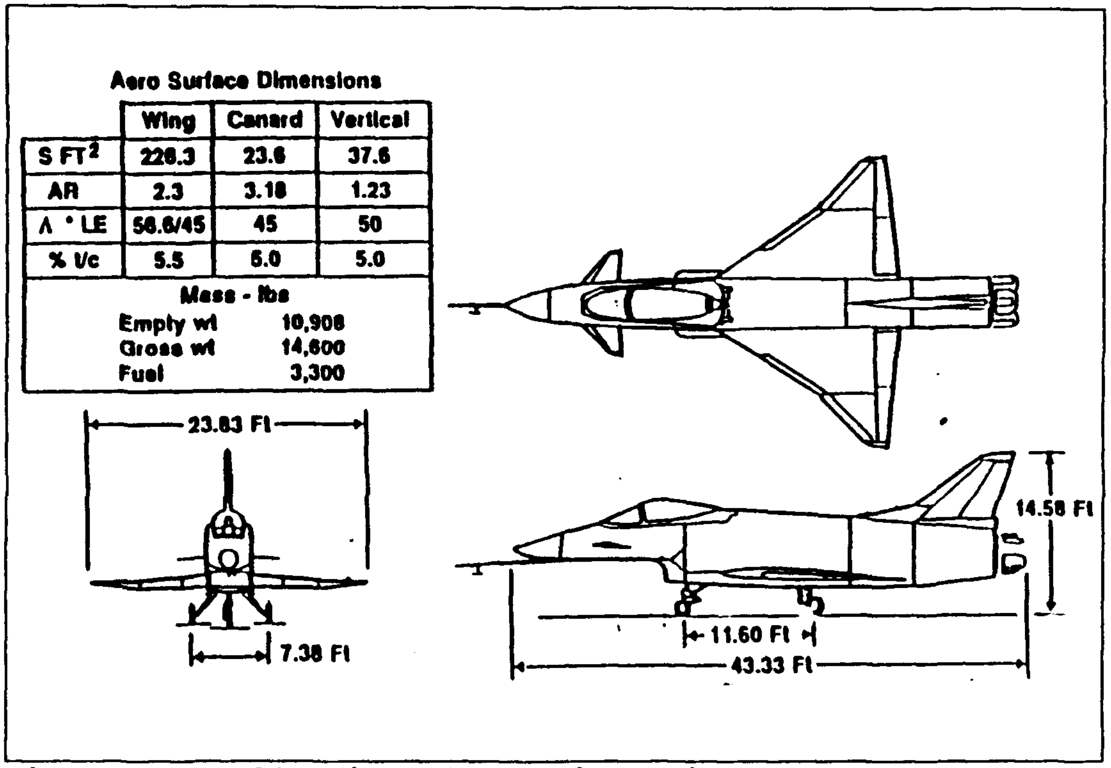

Figure 2. X-31A Aircraft Configuration

The use of canard configuration as a potential method for improved aerodynamic performance has received considerable attention in recent years, both experimentally and computationally. Increased agility through the use of a close-coupled canard configuration for enhanced lift has been the subject of growing scientific interest and practical aeronautical application. The favorable interference effect between the vortex systems of the canard and the wing in a close-coupled canard configration has been well recognized and demonstrated [Refs. 2 & 3]. Another area of increased interest for lift enhancement involves interactions between an oscillating close-coupled canard and the flow field of the main wing.

B. OSCILLATING CANARD

There is considerable interest in unsteady flows produced by small amplitude oscillations of the canard. Ashworth, Mouch and Luttges [Ref. 4] carried out visualization and anemometry analyses of forced unsteady flows about an X-29 model. Mouch, McLaughlin and Ashworth [Ref. 5] investigated the flowfield around the tandem wing of an X-29 model in the wake of an oscillating canard. The local velocity above and below the wing was measured with the canard oscillating and compared to the cases with the canard static. The flow visualization shows that the canard tip vortex has a greater effect on the flow over the tandem wing than the leading edge vortex. The quantitative data confirms that the largest velocity fluctuations are behind the canard tip. Thus, the tip vortex and not the leading edge vortex dominates the flowfield in the vicinity of the tandem wing.

Huyer and Luttges [Ref. 6] studied the flowfield interaction between the unsteady wake of an oscillating canard upstream of a static wing and the flowfield of the wing itself. A NACA 0015 airfoil was used for both the canard and the main wing. The main wing was mounted coplanar to the canard and 0.5 chord lengths downstream. Angles of attack of 10 and 20 degrees were used for the main wing. The mean canard deflection angle was +/- 10 degrees. The canard was oscillated about the quarter chord with periods of 156 and 105 msec (coresponding to frequencies of 6.4 Hz and 9.5 Hz). It was found that the dynamic stall vortex from the oscillating canard energized the boundary layer of the main wing which resulted in flow reattachment at angles of attack far exceeding static

stall angles for the main wing. But the amount of enhanced lift was not quantified. No comparison was made to the case of a static canard.

C. STATEMENT OF PURPOSE

It is thus clear from the previous work of others that the data available on the influence of canard oscillations on the flow characteristics of the main wing is extremely limited. The flow physics of the oscillating-canard wing configuration is still not sufficiently understood and documented. Of special significance is the understanding of the effect of canard oscillations on the vortex development under rapid maneuvering conditions envisioned for the X-31A aircraft. The recent investigation [Refs. 7 - 9] carried out at the Naval Postgraduate School (NPS) as part of enhanced fighter maneuverability research program was the first of its kind undertaken to characterize the flowfield around a static-canard configured fighter aircraft model comparable to the X-31A undergoing dynamic pitching and sideslipping motions.

The objective of this investigation is therefore to study the influence of an oscillating canard on a X-31A-like model in both static and dynamic conditions. Specifically, the wing root vortex breakdown characteristics are investigated in the NPS water tunnel using dye injection flow visualization technique.

II. EXPERIMENTIAL APPARATUS

A. WATER TUNNEL

The flow visualization water tunnel facility at the Naval Postgraduate School was designed by Eidetics, Inc., Torrance,California, and installed in late 1988. Figure 3 shows the layout of the water tunnel. It is described below briefly and more details may be found in [Refs. 9 & 10].

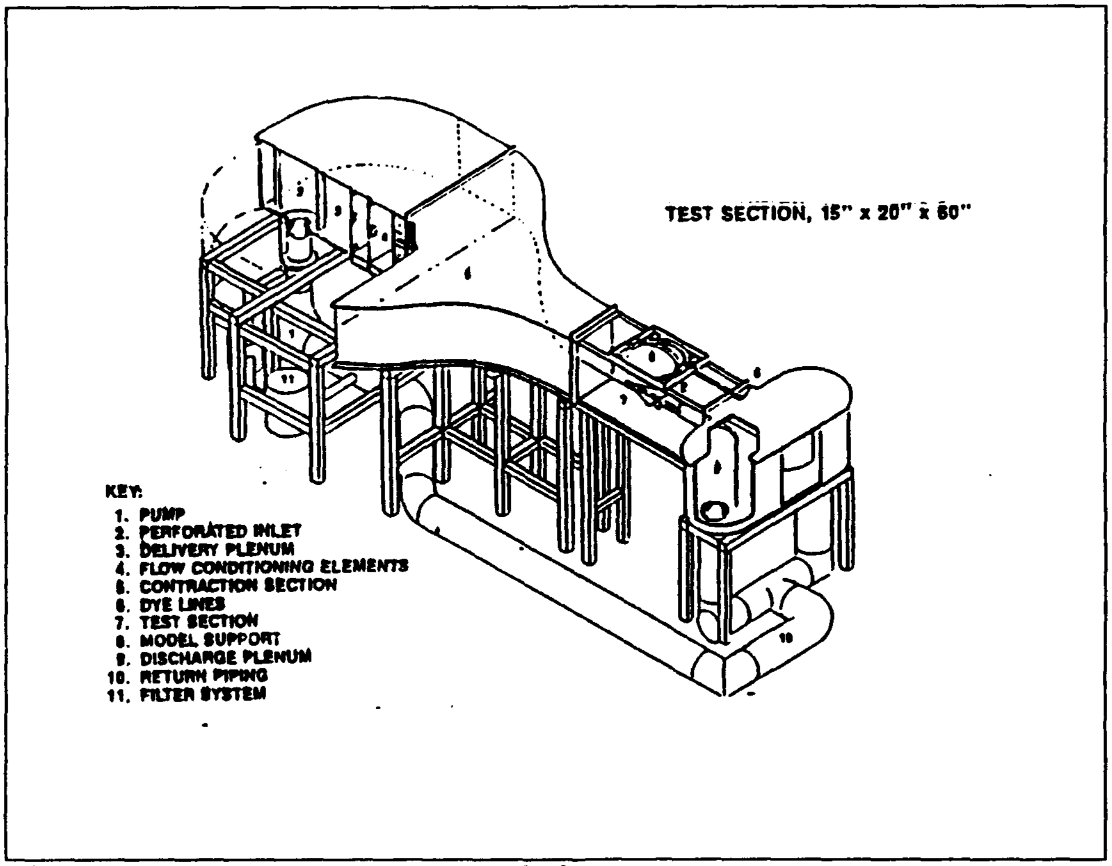

Figure 3. Water Tunnel Facility at NPS

The NPS water tunnel is a closed circuit facility for studying a wide range of aerodynamic and fluid dynamic phenomena. Its key design features are high flow quality, horizontal orientation and continuous operation. The test section is 15 inches wide, 20 inches high, and 60 inches long. The model attitude in pitch and yaw is adjusted with two servo motors. Each motor has a high/low rate switch and could be controlled by a remote control. The high pitch rate and low pitch rate correspond to 4.6 deg/sec and 2.3 deg/sec, respectively.

B. X-31A-LIKE MODEL

A simplified 2.3% scale model of the X-31A-like fighter aircraft with an oscillating canard was used in this investigation (Fig. 4). The model has a slightly different configuration than the actual X-31A aircraft; in particular it does not have a vertical tail and a canopy. It has a double delta wing and a delta canard. The canard is essentially a flat plate airfoil made of plastic (Fig.5). The horizontal and vertical distances of the quarter-chord point of the canard root chord from the quarter-chord point of the wing root chord are 47.7% and 7.95% of the wing root chord, respectively. The canard is oscillated at a desired amplitude by means of a flexible shaft driven by a small DC motor through a speed reduction gear unit (Fig. 6) mounted on the model C-strut support. A rechargeable battery drives the motor whose speed is controlled by a potentiometer. The mean deflection angle of the canard (δ) can be varied from -25^0 to $+25^0$. The canard can be oscillated at two nominal frequencies - a low value of 1.6 Hz and a high value of 10 Hz. With the mean deflection angle of the canard set at 0^0 at either of these frequencies,

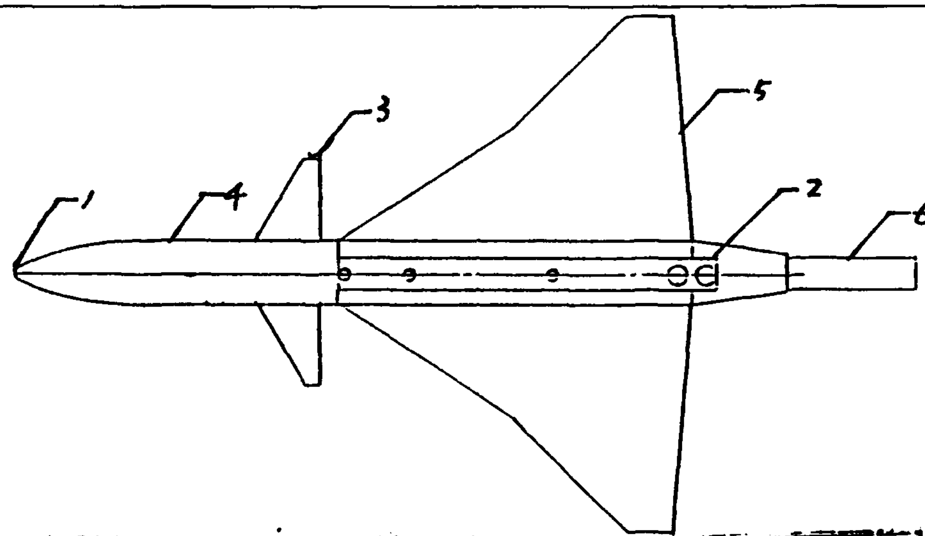

1	NOSE	4	FUSELAGE
2	TOP/BOTTOM PLATE	5	WING
3	CANARD	6	STING/TAIL CONE

Figure 4. X-31A-Like Aircraft Model

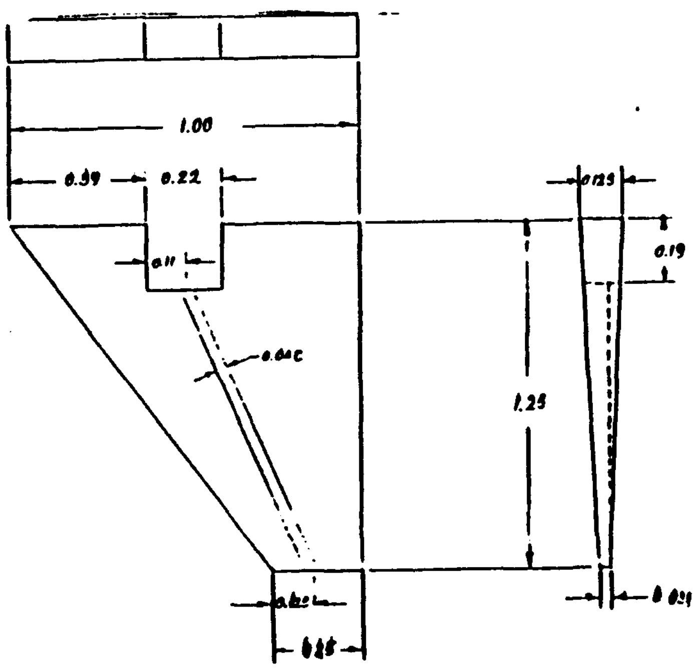

Figure 5. Canard Configuration

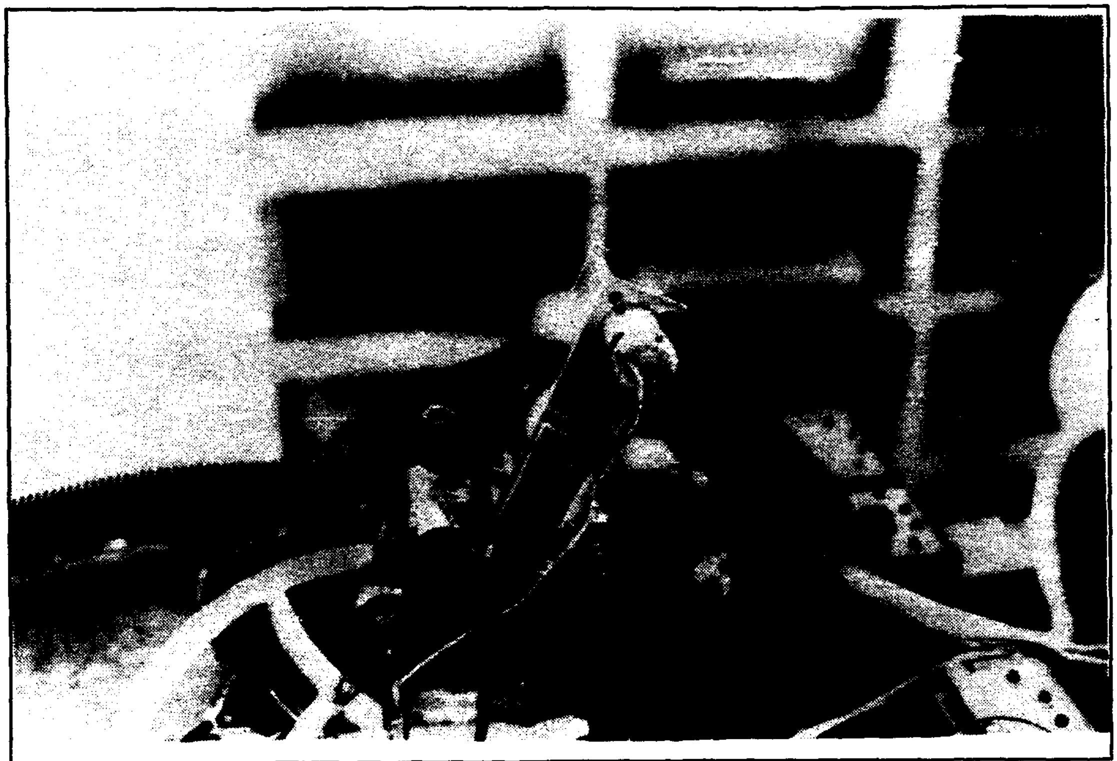

Figure 6. Speed Reduction and Gearbox Assembly

the canard amplitude (δ_a) can be varied upto +/- 25^0. Key dimensions of the model are listed below:

1. Total length = 12.0 in.
2. Span (wing, canard)= 8.0 in., 3.5 in.
3. Sweep angle (wing, canard)= 58°/46°, 37°
4. Wing chord= 5.5 in.(root), 2.5 in.(mid), 0.53 in. (tip)
5. Wing area= 19.3 in^2.
6. Canard chord= 1.0 in.(root), 0.25 in.(tip)
7. Canard area= 1.565 in^2.
8. Area ratio (canard/ wing)= 8.11%

In this investigation, the focus was on the development and bursting of vortices shed from the root of the wing. Therefore, only canard tip ports and wing-root dye- tubes were used. There were two dye-injection ports on the upper surface of the canard and two dye tubes located on the bottom surface of the wing with the tip at the leading edge of the root chord (Fig.7). Dyes were delivered from the pressurized dye supply system and injected through the dye ports/dye tubes.

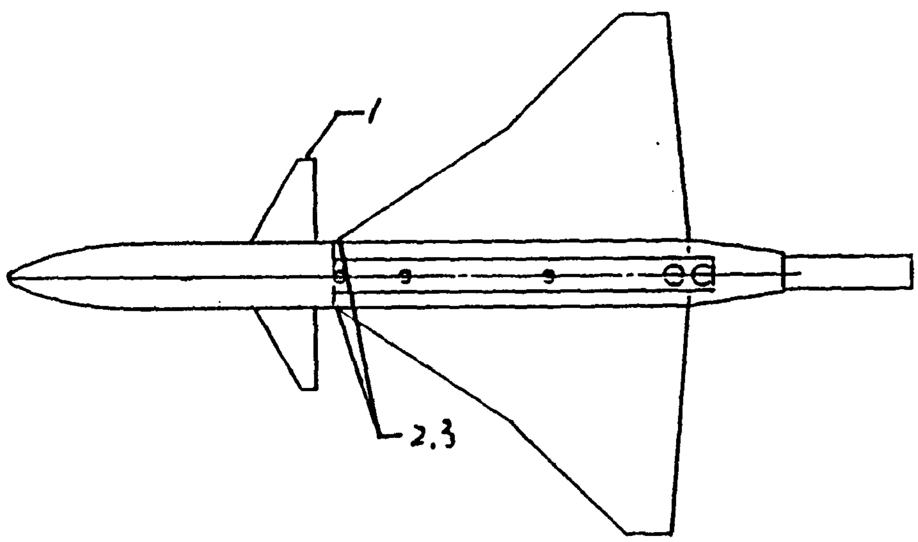

NO.	LOCATION	COLOR
1	CANARD ROOT	RED
2	WING ROOT	BLUE
3	WING ROOT	YELLOW

Figure 7. Dye Injection Location on the X-31A-Like Model

It must be noted here that there were some minor differences between the X-31A-like model used in this investigation and that used by Kim [Ref 9.]. The latter canard was made of aluminum with a 12%-thick double circular arc symmetric airfoil section had a fixed deflection angle of 2^0, and was located a little closer to the wing (43.18%).

C. MODEL MOUNTING

It was important to insure that the model was mounted horizontally in the water tunnel with zero pitch, zero yaw, and zero roll angle. The model mounting in the test section was achieved in the following way. First, the canard was located in the desired position with respect to the wing. The model with an extension bar was then attached to the sting holder on the model support base by using a small hexagonal head screw. The model was introduced into the water surface by lowering the model support base to its horizontal position and the model horizontality was checked visually by the timing and degree of wetting on both wing surfaces. To assure zero pitch angle, the centerline of the model (fuselage) was aligned with the freestream (tunnel centerline) by using spacers as needed between the model support base and the top of the test section frame. Finally, zero yaw angle was checked by setting the model nose equidistant from either side wall of the test section and observing symmetric dye lines from both wing surfaces at zero pitch angle. The zero roll angle was checked by locating the left and right wing tip at the same height from the bottom surface of the water tunnel. The axis of rotation for the pitch motion was located 8.45 inches aft of the nose.

III. EXPERIMENTIAL PROCEDURE

A. EXPERIMENTS

The flow velocity in the water tunnel was kept nearly constant at 0.25 ft/sec which corresponds to a nominal Reynolds number of 10,200 (based on wing root chord of the model). Although the flow Reynolds number in the water tunnel is very low, studies by other researchers [Refs. 11-13] have indicated that water tunnel data on the burst locations of vortices shed off sharp leading edges compare very favorably with the data from flight and ground tests.

The experimental program was carried out for various test conditions listed in Table 1.

B. REDUCED PITCH RATE SIMULATION

In real flight situations, an aircraft always has unsteady state conditions, especially at high angles of attack where the flow tends to separate from the wing surface. When an aircraft has input of dynamic motion (ie., pitch up/pitch down) or of natural disturbances (ie. wind shear,gust) the resulting unsteady conditions will have major effect on the stability of the aircraft.

The unsteady motion of a pitching aircraft with an oscillating canard may be characterized using two non-dimensional parameters,namely a reduced pitch rate K for the aircraft and a reduced frequency K_c for the canard. These are defined

Table I. Test Matrix for Experimental Program

CANARD	MODEL	MODEL PITCH RATE(DEG/SEC)	CANARD FREQUENCY (NOMINAL)
STATIC (DEFLECTION $\delta=0^0$,+/-5^0,+/-10^0,+/-15^0,+/-20^0,+/-25^0)	STATIC (0^0 TO 50^0AOA)	-------	-------
DYNAMIC (AMPLITUDE= +/-5^0,$\delta=0^0$)	STATIC (0^0 TO 50^0AOA)	-------	1.6 Hz
DYNAMIC (AMPLITUDE= +/- 5^0,$\delta=0^0$)	STATIC (0^0 TO 50^0AOA)	-------	10.0 Hz
DYNAMIC (AMPLITUDE= +/- 25^0,$\delta=0^0$)	STATIC (0^0 TO 50^0AOA)	-------	1.6 Hz
DYNAMIC (AMPLITUDE= +/- 25^0,$\delta=0^0$)	STATIC (0^0 TO 50^0AOA)	-------	10.0 Hz
STATIC (MEAN DEFLECTION $\delta=0^0$)	DYNAMIC (0^0 TO 50^0 AOA 50^0 TO 0^0 AOA)	2.3, 4.6	-------
DYNAMIC (AMPLITUDE $\delta_{a=}$ +/- 5^0 $\delta=0^0$)	DYNAMIC (0^0 TO 50^0 AOA 50^0 TO 0^0 AOA)	2.3, 4.6	1.6 Hz
DYNAMIC (AMPLITUDE $\delta_{a=}$ +/- 5^0 $\delta=0^0$)	DYNAMIC (0^0 TO 50^0 AOA 50^0 TO 0^0 AOA)	2.3, 4.6	10 Hz
DYNAMIC (AMPLITUDE $\delta_{a=}$ +/- 25^0 $\delta=0^0$)	DYNAMIC (0^0 TO 50^0 AOA 50^0 TO 0^0 AOA)	2.3, 4.6	1.6 Hz
DYNAMIC (AMPLITUDE $\delta_{a=}$ +/- 25^0 $\delta=0^0$)	DYNAMIC (0^0 TO 50^0 AOA 50^0 TO 0^0 AOA)	2.3, 4.6	10 Hz

as follows:

$$K=\frac{\dot{\alpha}L}{2U_{\infty}} \tag{1}$$

$$K_c=\frac{\omega C}{2U_{\infty}} \tag{2}$$

where

K: model reduced pitch rate, non-dimensional

$\dot{\alpha}$: pitch rate, rad/sec

L: characteristic length of the model, ft

U_{∞}: freestream velocity, ft/sec

K_c: canard reduced frequency, non-dimensional

ω: canard oscillation frequency, rad/sec

C: characteristic length of the canard, ft

The non-dimensional parameter K can be calculated by equation (1). Table II lists the reduced pitch rates for the model and the full scale aircraft.

The non-dimensional parameter K_c can be calculated by equation (2). The values of K_c as a reference parameter for the oscillating canard are listed in Table III.

Table II. Reduced Pitch Rate Parameter for the Model

Pitch rate	α(rad/sec)	Length(ft)	U_∞(ft/sec)	K
Model low pitch rate	0.040	1	0.25	0.08
Model high pitch rate	0.080	1	0.25	0.16
Full scale X-31A Aircraft	0.700	43.33	253.35	0.06

* The model pitch-axis was located at 8.45 inches aft of the nose.

Table III. Reduced Frequency Parameter for the Canard

Canard Frequency	ω(rad/sec)	Canard root chord (ft)	U_∞(ft/sec)	K_c
Low Rate 1.6 Hz	10.1	0.083	0.25	1.7
High Rate 10 Hz	62.8	0.083	0.25	10.4

C. DATA ACQUISITION AND REDUCTION

The data collection was accomplished using two 35-mm cameras that gave simultaneous sideview and topview of the vortical flow field originating off the wing root of the X-31A-like model. A professional Sony video camera and a 8-mm Sony home video camera were also used to record the flowfield over the model during static and dynamic conditions. The method of photography is decribed in section D.

The vortex burst locations for the case of static model and static canard were visually determined from the photographs, and the videotape recordings used to cross

check these locations. For the dynamic case (with either the model pitching or the canard oscillating) it was difficult to identify the vortex burst location on the photographs and therefore video playback was used extensively for this purpose supported by occasional direct observation in the water tunnel. The determination of burst location was impossible in the dynamic case with high pitch rate and the canard oscillating at 10 Hz.

For this investigation all measurements were made on the starboard side of the model using the leading edge of the wing root chord as the reference point. The measurements were made with utmost care and consistency, and scaled for non-dimensionalization using the wing root chord. Some degree of imprecision may be present in the reduced data due to the difficulty in determining vortex burst locations particularly at high angles attack, high pitch rate and high canard frequency. During the static segment of the experiment, the bursting location fluctuated as much as +/- 0.25 inches. The bursting locations for static and dynamic conditions are listed in Table IV. (Appendix A)

D. METHOD OF PHOTOGRAPHY

A Minolta 5000i camera with depth card and all the automatic functions of focusing, shutter speed control, aperture control and ASA setting was used for taking topview pictures. The automatic focus function was used very effectively for topview pictures, particularly during the dynamic case, because the focusing was automatically adjusted as the angle of attack was changed.

The sideview pictures were taken by a Nikon 2000 camera with auto/manual shutter speed, manual focusing, and manual aperture control to provide the best exposure. The light was provided by four Smith-Victor 600 watt photographic lights, and a floodlight installed below the test section. For the sideview photographs two of the lights were placed at a distance of three feet and at a 45° angle from the test section. Other two photographic lights were placed below the test section. Figure 8 illustrates the lighting setup for the sideview and topview photographs. The same ligthing arrangement was

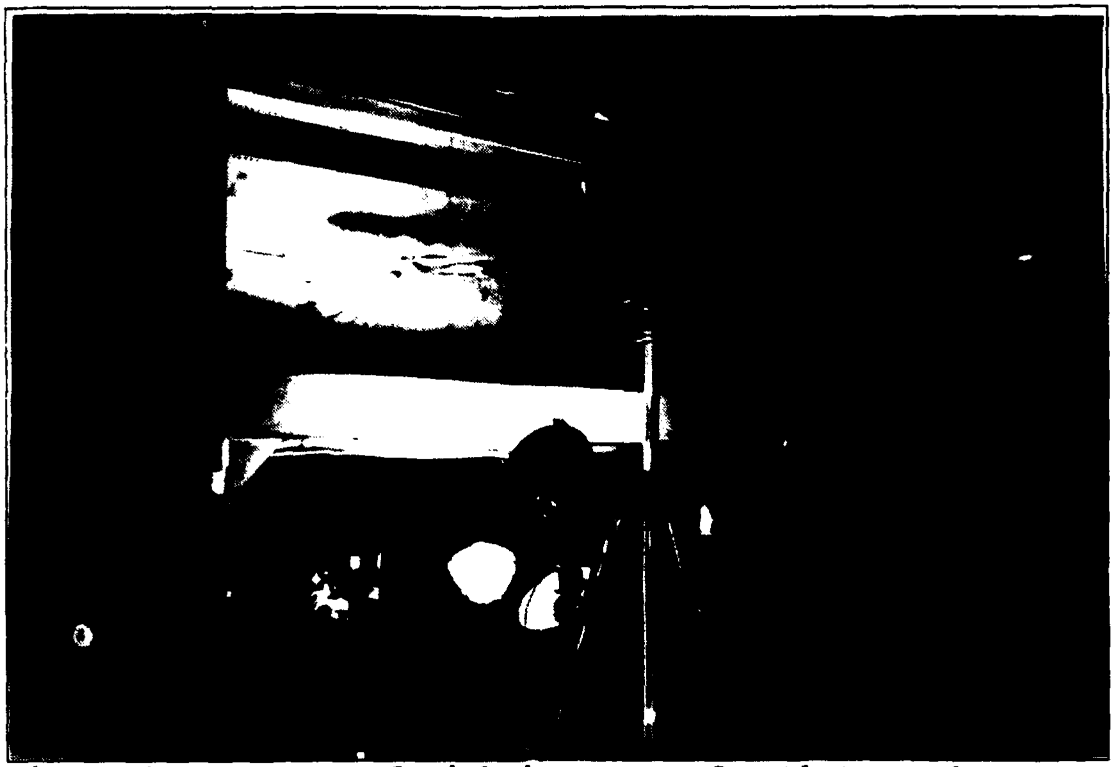

Figure 8. Camera and Lighting Setup for Photographs

used during videotaping of the vortical flow field on the model. The type of film used for all photographs was 35-mm black and white ASA 400 film. During the exposure of the

film, the sideview camera settings were as follows: ASA 400, aperture 11, shutter speed 250, with focusing on the centerline of the fuselage. The sideview camera was focused and the center of the camera field of view was aligned with the model pitch rotation axis. The topview camera settings were as follows: auto ASA setting (it read ASA 400 automatically), auto aperture, auto shutter speed, and auto focus. To know the angle of attack in the topview it was necessary to take both sideview and topview photographs simultaneously. This was accomplished by exposing the two cameras simultaneously using two remote shutter release cables.

IV. RESULTS AND DISCUSSION

The results of the investigation will be discussed with the aid of a series of flow visualization photographs and burst location plots. Several rolls of 35 mm black and white films were exposed and several hours of videotape recorded during the investigation. The experimental data on vortex burst location estimated from the flow visualization photographs and/or videotape recordings are tabulated in Appendix A (Table IV-IX). Selected flow visualization photographs are presented in Appendix B (Figures 9-81). Each figure shows two views of the flowfield taken simultaneously by the two 35-mm cameras, one in the sideview and the other in the topview (taken from below the test section of the water tunnel). The burst location plots derived from the burst location data are included in Appendix C (Figures 81-88).

First, some general comments will be made on the effects of angle of attack on the wing vortical flowfield visualized during the static condition with both the model and canard static. These results will be compared with those for the static conditions reported by Kim [Ref 9], where the canard configuration is different from the present configuration in respect of longitudinal location, deflection angle and shape (see section B, Chapter II). This will be followed by a discussion of the effects of canard (static deflection) angle on the wing root vortex burst location under static condition of the model. Next, the effects of canard oscillations on the static model will be discussed for a mean canard deflection

angle of 0^0. Finally, the effects of canard oscillations on the dynamic model will be discussed for two pitch-up motions with the mean canard deflection angle set at 0^0.

A. EFFECTS OF AOA ON THE WING FLOWFIELD OF X-31A- LIKE MODEL

Figures 9 - 17 show the effects of AOA on the wing vortical flowfield of the model with zero sideslip and 0^0 canard deflection. At 0^0 AOA, the flow over the wing surface is particularly smooth, attached and symmetric (Fig. 9). As the angle of attack is increased, the flow at the inner trailing edge of the wing progressively disperses outward to the tips, with no vortex developed yet. At 10^0 AOA, most of the flow has dispersed from the inboard of the wing surface to the outboard and along the leading edge (Fig. 10). With further increase in AOA, the dispersed flow fluctuates and starts to coil up into a vortex core shape with a maximum vortex core length on the wing surface. This vortex core is tigthly wound and extends aft downstream of the trailing edge until undergoing vortex core breakdown (bursting), usually signified by the stagnation of the core and abrupt expansion in its diameter. As the AOA is increased further, the vortex core bursting moves upstream over the wing surface (Figs. 11-16) and finally bursting occurs very close to the apex at about 50^0 AOA (Fig. 17). Note that the burst location has already crossed the trailing edge at AOA = 15^0 (Fig. 11). There observations of the vortex burst movement are qualitatively similar to those of Kim [Ref. 9] and Kwon [Ref. 7].

To summarize, in the AOA range $10^0 < \alpha < 50^0$ a pair of symmetric vortices develops over the wing surface and the burst location moves from the trailing edge to the apex. The effects of AOA on the bursting location of the wing root vortex core at zero

yaw angle are illustrated in Fig. 81. Also shown here for comparsion is the data from [Ref. 9]. Allowing for the minor differences in the canard configuration, the agreement between the data sets is considerd very good and lends credence to the repeatability of the flow visualization data. The slope of the burst location plot is seen to be steeper in the 15^0 to 30^0 AOA range than in the 30^0 to 50^0 range, suggesting nonuniform movement of the burst point with respect to the angle of attack.

B. EFFECTS OF STATIC CANARD DEFLECTION ANGLE ON THE WING FLOWFIELD OF THE STATIC MODEL

The effects of canard (static) deflection angle on the wing root vortex burst location under static condition of the model are presented in a series of photographs (Figs. 18-42) and burst location plots (Figs. 82 & 83). The canard deflection angle δ is varied from $+25^0$ to -25^0 (Table IV).

1. Effects of Postive Canard Deflection Angle

Figures 18-32 show the wing root vortex core length and bursting point at AOAs of $\alpha=20^0$, 30^0, and 40^0 for positive canard deflection angles of $\delta=5^0$, 10^0, 15^0, 20^0, and 25^0. At any given canard deflection angle, the effects of AOA on the wing vortical flowfield are qualitatively similar to those decribed earlier for the case of 0^0 canard deflection angle. Thus, the intial burst movement is quite rapid up to 30^0 AOA, after which it slows down as it approaches the apex. At any given AOA, the vortex core appears to burst earlier with increasing canard deflection angle. These effects are quantitatively illustrated in Figure 82. Compared with the 0^0 canard deflection case, the

burst location plots clearly indicate the unfavorable interference (earlier bursting) of positive deflection angle of the canard over the entire AOA range.

2. Effects of Negative Canard Deflection Angle

Figures 33-42 show the wing root vortex core length and bursting point at AOAs of $\alpha = 20^0$ and 30^0 for negative canard deflection angles of $\delta = -5^0$, -10^0, -15^0, -20^0, and -25^0. As before, the effects of AOA on the wing vortical flowfield are qualitatively similar to those described for the 0^0 and positive canard deflection angles. Figure 83 quantifies the effects of negative canard deflection angle on vortex burst location as a function of AOA. Once again these plots indicate the unfavorable interference (earlier bursting) caused by negative deflection angle of the canard. It appears that a negative deflection angle of the canard has slightly greater adverse effect than a positive deflection angle of the same magnitude. In terms of vortex burst response a 0^0-canard deflection angle appears to give better results.

C. Effects of Canard Oscillation on the Wing Flowfield of the Static Model

The effects of canard oscillations on the wing root vortex burst location under static condition of the model are presented in a series of photographs (Figs. 43-52) and burst location plots (Fig. 84). The canard was oscillated at two amplitudes ($\delta_a = +/- 5^0$ and $+/- 25^0$) each at a mean canard deflection angle of $\delta = 0^0$ but two frequencies of 1.6 Hz and 10 Hz corresponding to reduced frequencies of $K_C^* = 1.7$ and 10.4, respectively (Table V).

1. Effects of Small Amplitude Canard Oscillations

Figures 43-48 show the wing root vortex core length and bursting point at AOAs of at $\alpha=20^0$, 30^0, and 40^0 for small amplitude canard oscillations of δ_a=+/- 5^0 at two reduced frequencies of K_C=1.7 and 10.4. Comparing these figures with Figures 12, 14, and 16 ($\delta=0^0$, $K_C=0$), it is clear that the small amplitude low frequency oscillations tend to destabilize the vortex core, that is, cause early vortex bursting. On the other hand, the small amplitude high frequency oscillations appear to have a favorable interaction with the wing vortical flowfield resulting in a somewhat delayed vortex bursting. Figure 84 illustrates quantitatively the effects of canard oscillations on vortex burst location as function of AOA.

2. Effects of Large Amplitude Canard Oscillations

Figures 49-52 show the wing root vortex core length and bursting point at AOAs of $\alpha=20^0$ and 30^0 for large amplitude canard oscillations of δ_a= +/-25^0 at two reduced frequencies of K_C=1.7 and 10.4. Again comparing these figures with Figures 12, 14, and 16 ($\delta=0^0$, $K_C=0$), one can draw some qualitative conclusion on the effects of large amplitude low frequency oscillations: There is a marginally favorable interaction with the wing vortical flowfield. This effect is shown quantitatively as a functions of AOA in Fig. 84. In the case of large amplitude high frequency canard oscillations, it was not possible to visualize and determine the burst location from the photographs (Fig. 51-52) or videotape recordings because the vortex core appeared discrete with the dye spread all around. Therefore no conclusion can be drawn on the effects of large amplitude high frequency canard oscillations.

D. DYNAMIC EFFECTS OF AOA ON THE WING FLOWFIELD OF THE PITCHING MODEL WITH STATIC CANARD

Figures 53-63 present photographs taken during simple pitch-up and pitch-down motions at two reduced pitch rates with zero sideslip and static canard ($\delta = 0^0$). The corresponding burst location plots appear in Fig. 85. During the pitch-up and pitch-down motions, the model AOA was varied from 0^0 to 50^0 and 50^0 to 0^0, respectively, at two reduced pitch rates of K=0.08 and 0.16 (Table VI).

Figures 53-55 show the wing flowfields at instantaneous AOAs of $\alpha = 20^0$, 30^0, and 40^0 during simple pitch-up motion with K=0.08, while Figs 56-58 show corresponding flowfields for K=0.16. The wing flowfield during simple pitch-down motion for K=-0.08 is shown in Figs 59-60 for instantaneous AOAs of $\alpha = 30^0$ and 20^0, respectively. The corresponding flowfield for K=-0.16 is shown in Figs. 61-63 for instantaneous AOAs $\alpha =$ 40^0, 30^0 ,and 20^0, respectively. Comparison of these figures with Figs 12, 14, and 16 for the static case ($\delta = 0^0$, $K_C = 0$, $K = 0$) indicates clearly that the pitch-up motion causes delay in vortex bursting and this burst lag increases with pitch rate. The reverse is true for the pitch-down motion. In other words, the location of the wing root vortex burst point relative to the static case moves rearward with increasing pitch-up motion and forward with increasing pitch-down motion. These observations of the dynamic effect on the vortex burst location are in agreement with those of Hebbar et al.[Refs. 8,11].

These dynamic effects are shown quantitatively as a function of AOA in Fig. 85. Note that in these plots, the effects of pitch-down motion are not brought out strongly. It should be remarked here that considerable difficulty was experienced to determine burst

location, particularly for the pitch-down motion. Consequently, keeping in view the experimental uncertainty in the data, the trends in these plots may be taken to validate the above observations on dynamic effects.

E. EFFECTS OF CANARD OSCILLATIONS ON THE WING FLOWFIELD OF THE PITCHING MODEL

The effects of canard oscillations on the wing root vortex burst location during pitching motion of the model are presented in a series of photographs (Figs. 64-80) and burst location plots (Figs 86-88). As in the static case of the model, the canard was oscillated during the dynamic motion of the model at two amplitudes (δ_a=+/- 5^0 and +/- 25^0) each at a mean canard deflection angle of δ= 0^0 but two frequencies of 1.6 Hz and 10 Hz corresponding to the reduced frequencies of K_c= 1.7 and 10.4, respectively. The dynamic motion of the model consisted of simple pitch-up and pitch-down motions with the AOA varying from 0^0 to 50^0 and 50^0 to 0^0, respectively, at two reduced pitch rates of K=0.08 an 0.16. The vortex burst location data is listed in Tables VII-IX.

1. Effects of Small Amplitude Low Frequency Canard Oscillations

Figures 64-71 present selected photographs taken at instantaneous AOAs of α= 20^0, 30^0, 40^0 during dynamic motion of the model with small amplitude canard oscillations of δ_a=+/-5^0 at a reduced frequency of K_c= 1.7. Figure 86 illustrates quantitatively the effects of canard oscillations on vortex burst location as a function of AOA during pitching motions (see Table VII). Also shown plotted here is the burst plot for the static model with the static canard. A cursory comparison with this plot indicates some favorable

interference effects of canard oscillations during low pitch rates. To see clearly the effects of canard oscillations, it is necessary to compare the plots of Fig. 86 with the appropriate dynamic plots for the static canard case shown in Fig. 85. A careful observation reveals the fact that small amplitude, low frequency canard oscillations can lead to beneficial interference with the wing vortical flowfield (vortex burst delay) during low pitch rate but may adversely interfere (vortex burst advance) during high pitch rate.

2. Effects of Small Amplitude High Frequency Canard Oscillations

Figures 72-78 present selected photographs taken at instantaneous AOAs of α= 20^0 and 30^0 during dynamic motions of the model with small amplitude canard oscillations of δ_a=+/-5^0 at a reduced frequency of K_C=10.4. Figure 87 quantifies the effects of canard oscillations on vortex burst location as a function of AOA during pitching motions (see Table VIII). Also shown plotted here is the burst plot for the static model with the static canard. Although a cursory comparison with this plot may lead to some conclusions, a detailed comparison of the dynamic plots of Fig. 87 with the appropriate dynamic plots for the static canard shown in Fig. 85 is required to determine the effects of canard oscillations. Such a comparison would show that small amplitude high frequency oscillations can adversely affect the wing vortical flowfield during pitching motions in general, except for a possible favorable interference at high AOAs during high-rate pitch up motion.

3. Effects of Large Amplitude Low Frequency Canard Oscillations

Figures 79 and 80 present two photographs taken at the instantaneous AOA of α= 30^0 during pitch-up and pitch-down motion of the model, respectively, with large amplitude canard oscillations of δ_a=+/-25^0 at a reduced frequency of K_C=1.7. Figure 88 presents the effects of canard oscillations on vortex burst location as a function of AOA during pitching motion (see Table IX). The burst plot for the static model with the static canard is also included in Fig. 88 for a quick but crude comparison that indicates favorable interference effects of canard oscillations during dynamic motions. As pointed out earlier, it is , however, necessary to compare the dynamic plots of Fig. 88 with the appropriate dynamic plots for the static canard shown in Fig. 85. This comparison will confirm that large amplitude low frequency oscillations lead to favorable interference of the wing vortical flowfield (vortex burst delay) during the pitching motions (up or down).

4. Effects of Large Amplitude High Frequency Canard Oscillations

As mentioned before, both the visualization of vortex core length and the identification of burst point location in the flow visualization photographs and videotape recordings were rendered extremely difficult by the intermittent nature of the vortex core and the spread of the dye. No burst location plots could be constructed from the flow visualization data and therefore no conclusion could be drawn on the effects of large amplitude, high frequency canard oscillations during pitching motions of the model.

V. CONCLUSIONS AND RECOMMENDATIONS

A low speed flow visualization investigation was initiated to study the effects of oscillating a close-coupled canard on the wing vortex development and bursting phenomena on a 2.3% scale model of a X-31A-like fighter aircraft using dye injection in the NPS water tunnel. The main focus of this study was two-fold: First, to study the effects of canard oscillations on the wing vortical flowfield of the static model. Secondly, to study the effects of canard oscillations on the vortical flowfield of the model pitching at different rates. The water tunnel visualization data reported here is believed to be the <u>first</u> of its kind for a close-coupled canard-configured X-31A-like aircraft model in dynamic pitching motion. The major conclusions of this investigation are:

1. Static and dynamic effects (with static canard): As the angle of attack increases from 15^0 to 50^0, a pair of symmetric vortices develops and the burst location moves upstream, indicating that the separated flow region increases at higher AOAs. The dynamic tests indicate that the vortex burst lag increases with the pitch rate. These finding are in agreement with those of earlier investigators.
2. Effects of canard (static) deflection angle: Either positive or negative canard deflection angle leads to unfavorable interference with the vortical flowfield (early vortex bursting) over the entire AOA range tested. In terms of the vortex burst response, a 0^0-canard deflection angle yields optimum results.

3. Effects of canard oscillations on the static model: At small amplitudes, the low frequency canard oscillations tend to destabilize the wing vortex core (early bursting) whereas the high frequency oscillations delay vortex bursting. The large amplitude low frequency oscillations seem to have a marginally favorable effect on the wing vortical flowfield.

4. Effects of canard oscillations on the dynamic model: The dynamic tests indicate that the large amplitude, low frequency oscillations of the canard interact favorably with the wing vortical flowfield to delay vortex bursting during pitch-up or pitch-down motion. The small amplitude, low frequency oscillations tend to delay vortex bursting during low pitch rate motion only, whereas the high frequency oscillations in general tend to have an adverse effect on the vortical flowfield (early vortex bursting).

The following recommendations are made based on this investigation:

1. The investigation should be extended to study the effects of canard oscillations at other mean canard deflection angles.

2. The investigation should also be extended to study the effects of canard oscillations on a sideslipping model.

3. The flow visualization data should be compared with quantitative data from Laser Doppler Velocimetry (LDV) and checked against computational results.

LIST OF REFERENCES

1. O'Leary, C.O. and Weir, B., *The Effect of the Foreplanes on the Static and Dynamic Characteristics of a Combat Aircraft Model,* AGARD Conference Proceedings No.465, Oct. 1989.

2. Behrbohm, H., *Basic Low Speed Aerodynamics of the Short-Coupled Canard Configuration of Small Aspect Ratio,* SAAB TN 60, 1965.

3. Hummel, D., and Oelker, H-Chr., *Effects of Canard Position on the Aerodynamic Characteristics of a Close-Coupled Canard Configuration at Low Speed,* AGARD Conference Proceedings No.465, Oct. 1989.

4. Asworth,J., Mouch,T., and Luttges, M., *Visualization and Anemometry Analyses of Forced Unsteady Flows about an X-29 Model, AIAA Paper 88-2570, June 1988.*

5. Mouch, T., McLaughlin, T., and Ashworth, J., *Unsteady Flows Produced by Small Amplitude Oscillations of the Canard of an X-29 Model,* AIAA Paper 89-2229, July/Aug. 1989.

6. Huyer, S.A., and Luttges, M.W., *Unsteady Flow Interactions Between the Wake of an Oscillating Airfoil and a Stationary Trailing Airfoil,* AIAA Paper 88-2581, June 1988.

7. Kwon, H.M., *Water Tunnel Flow Visualization Studies of a Canard-Configured X-31A-Like Fighter Aircraft Model,* Master's Thesis, Naval Postgraduate School, Monterey, California, Sept. 1990.

8. Hebbar, S.K., Platzer, M.F., and Kwon, H.M., *Static and Dynamic Water Tunnel Flow Visualization Studies of a Canard Configured X-31A-Like Fighter Aircraft Model,* AIAA Paper 91-1629, June 1991.

9. Kim, C.H., *Flow Visualization Studies of a Sideslipping Canard-Configured X-31A-Like Fighter Aircraft Model,* Master's Thesis, Naval Postgraduate School, Monterey, California, Dec. 1991

10. User's Manual, *Flow Visualization Water Tunnel Operations Manual for Model 1520,* Eidetics International Inc., Torrance, California, 1988 (prepared for Naval Postgraduate School, Monterey, California).

11. Hebbar, S.K., Platzer, M.F. and Cavazos O.V., *A Water Tunnel Investigation of the Effects of Pitch Rate and Yaw on LEX Generated Vortices of an F/A-18 Fighter Aircraft Model,* AIAA Paper 91-0280, Jan. 1991.

12. Del Frate, J.H. and Zuniga, F.A. *In-Flight Flow Field Analysis on the NASA F-18 High Alpha Research Vehicle with Comparisons to Ground Facility Data,* AIAA Paper 90-0231, Jan. 1990.

13. Manor, D., Miller, L., and Wentz, W.H. Jr., *Static and Dynamic Water Tunnel Tests of Slender Wings and Wing-Body Configuration at Extreme Angle of Attack,* AIAA Paper 90-3027-CP, Aug. 1990.

APPENDIX A. EXPERIMENTAL RESULTS (TABLES)

Table IV. % Non-dimensional Vortex Core Length with both Model and Canard Static (K=0, K_C=0) for Various Canard Deflection Angels

AOA(deg) δ(deg)	15	20	25	30	35	40	45
0	79.5	67.6	31.8	19	13.6	9.1	8.2
5	77.2	65.9	29.5	18.1	13.6	8	7.2
10	72.7	59	29.5	15.9	9.1	*	*
15	70.4	59	25	15.9	6.82	*	*
20	68.1	58.5	25	11.3	4.5	*	*
25	63.6	57.9	20.4	9.1	*	*	*
-5	70.5	56.8	31.8	15.9	9.1	4.54	*
-10	68.1	52.5	29.5	13.6	9.1	*	*
-15	68.1	50	27	11.3	9.1	4.5	*
-20	64	50	25	11.3	9.1	*	*
-25	60	40	13.6	11.3	9.1	6.8	*

* Vortex Tracking and/or Burst Identification was not Possible

Table V. % Non-Dimensional Vortex Core Length for Static Model with Oscillating Canard (K=0, $\delta=0^0$)

AOA (deg)	$\delta=0^0$ $K_C=0$	$\delta_a=+/-5^0$ $K_C=1.7$	$\delta_a=+/-5^0$ $K_C=10.4$	$\delta_a=+/-25^0$ $K_C=1.7$	$\delta_a=+/-25^0$ $K_C=10.4$
15	79.5	75	*	*	*
20	67.6	56.8	63.6	*	*
25	31.8	36.3	50	40.9	*
30	19	18.3	27.2	22.7	*
35	13.6	13.6	13.6	13.6	*
40	9.1	11.3	9.1	9.1	*
45	8.2				

* Vortex Tracking and/or Burst Identification was not Possible

Table VI. % Non-Dimsional Vortex Core Length for Pitching Model with Static Canard Static ($\delta=0^0$)

AOA (deg)	K=0	K=0.08	K=-0.08	K=0.16	K=-0.16
15	79.5				
20	67.6	63	41	*	45.4
25	31.8				
30	19	41	22.7	60	18.1
35	13.6				
40	9.1	18.1	9.1	18.1	*
45	8.2				
50		4.5	4.5	4.5	*

* Vortex Tracking and/or burst indentification was not Possible

Table VII. % Non-dimensional Vortex Core Length for the Pitching Model with Small Amplitude, Low Frequency Oscillations of the Canard (δ=0^0 δ_a=+/-5^0, K_C=1.7)

AOA (deg)	K=0	K=0.16	K=-0.16	K=0.08	K=-0.08
15	75				
20	56.8	36.3	27.2	*	*
25	36.3				
30	18.2	13.6	18.1	45.4	31.8
35	13.6				
40	13.6	9.1	13.6	18.1	22.7
45					
50		4.5	4.5	4.5	9.1

* Vortex Tracking and/or Burst Identification was not Possible

Table VIII. % Non-dimensional Vortex Core Length for the Pitching Model with Small Amplitude, High Frequency Oscillations of the Canard (δ=0^0, δ_a=+/-5^0, K_C=10.4)

AOA (deg)	K=0	K=0.08	K=-0.08	K=0.16	K=-0.16
20	63.6	36.3	18.1	45.4	27.2
25	50				
30	27.2	13.6	13.6	27.2	13.6
40	9.1	9.1	4.5	18.1	9.1
50		4.5	4.5	9.1	4.5

* Vortex Tracking and/or Burst Identification was not Possible

Table IX. % Non-dimensional Vortex Core Length for the Pitching Model with Large Amplitude, Low Frequency Oscillations of the Canard ($\delta=0^0$, $\delta_a=+/-25^0$, $K_C=1.7$)

AOA (deg)	K=0	K=0.16	K=-0.16	K=0.08	K=-0.08
25	41				
30	22.7	28.2	31.8	40	45
35	13.6				
40	9.1	22.7	20	22.7	35
50		9.1		9.1	13.6

APPENDIX B. EXPERIMENTIAL RESULTS (PHOTOGRAPHS)

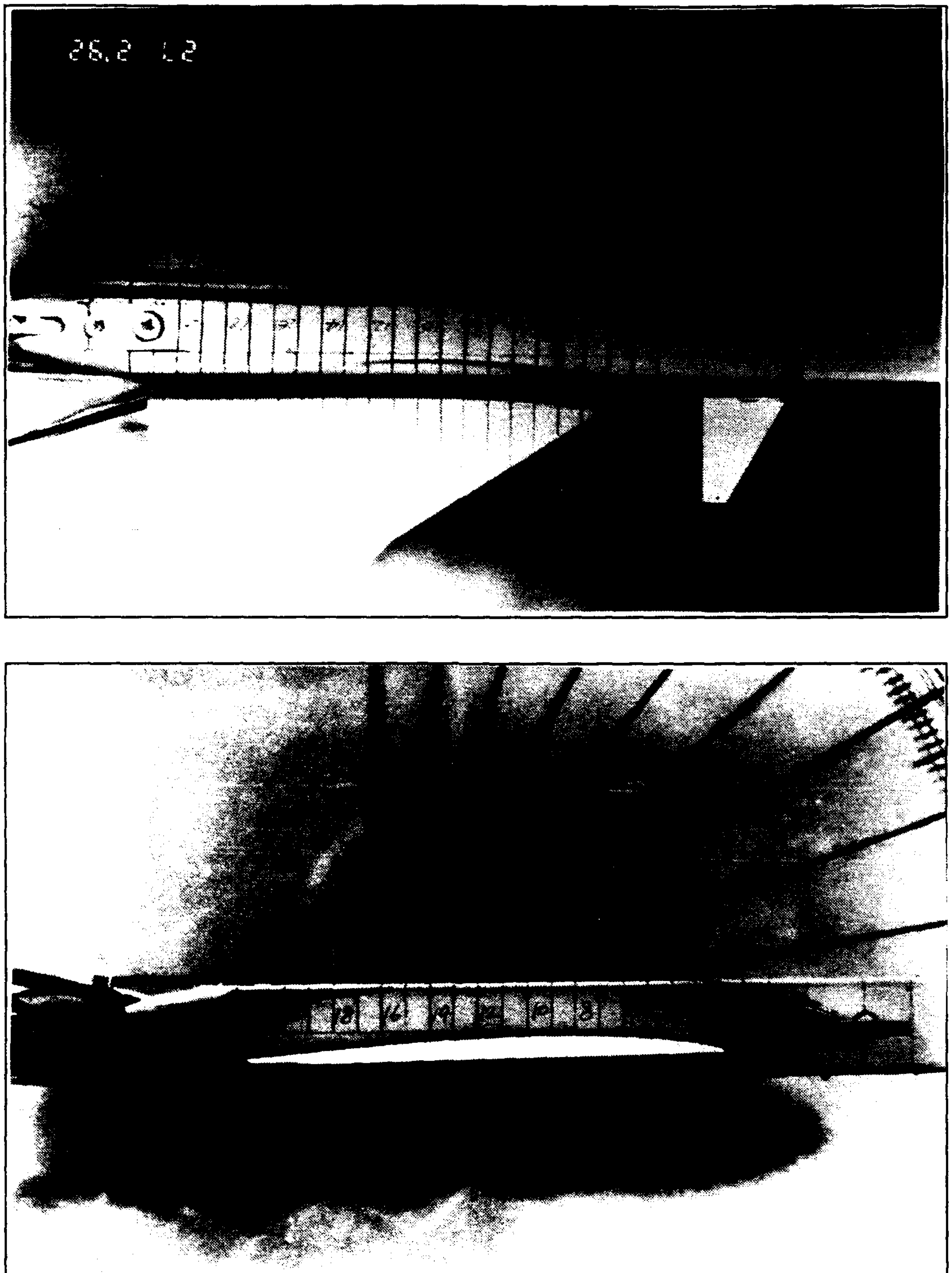

Figure 9. Wing Root Vortex Flow, Static Case, $\alpha=0°$, $\delta=0°$.

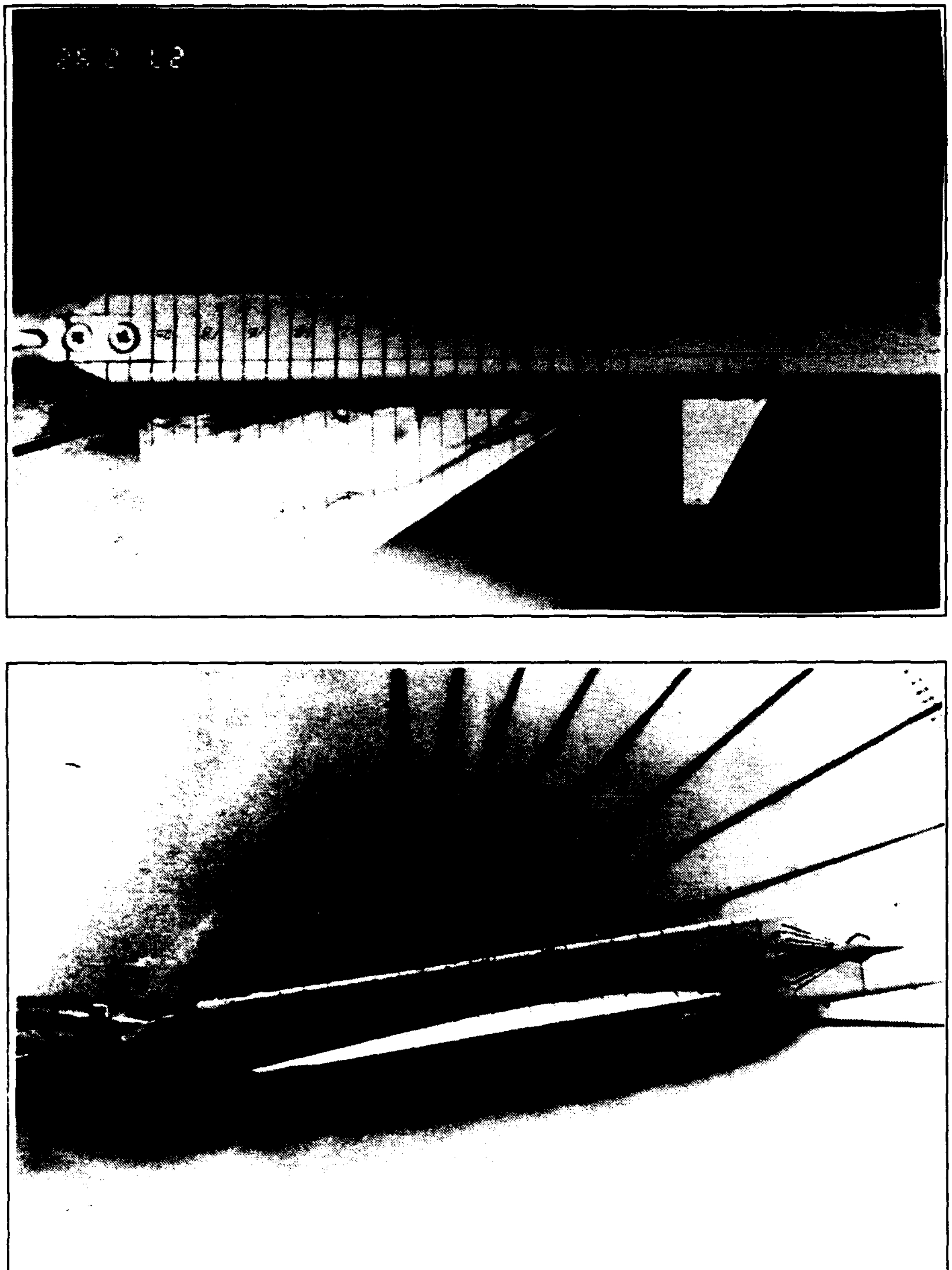

Figure 10. Wing Root Vortex Flow, Static Case $\alpha=10^\circ$, $\delta=0^\circ$

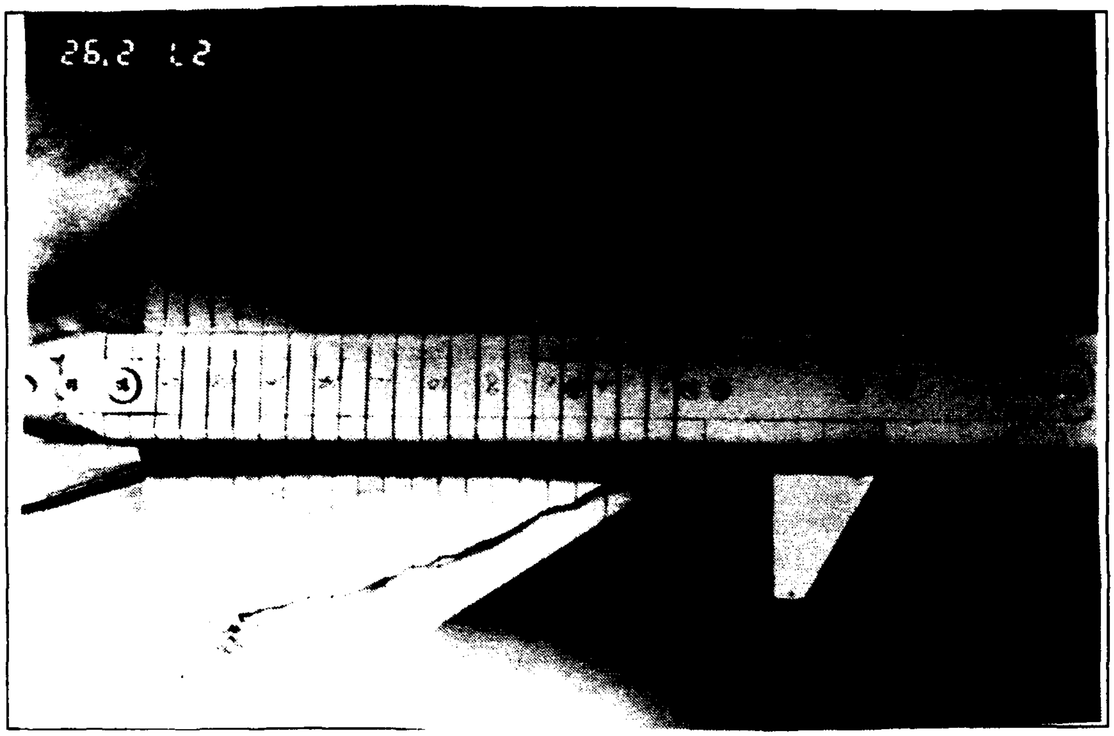

Figure 11. Wing Root Vortex Flow, Static case, $\alpha=15^{\circ}$, $\delta=0^{\circ}$

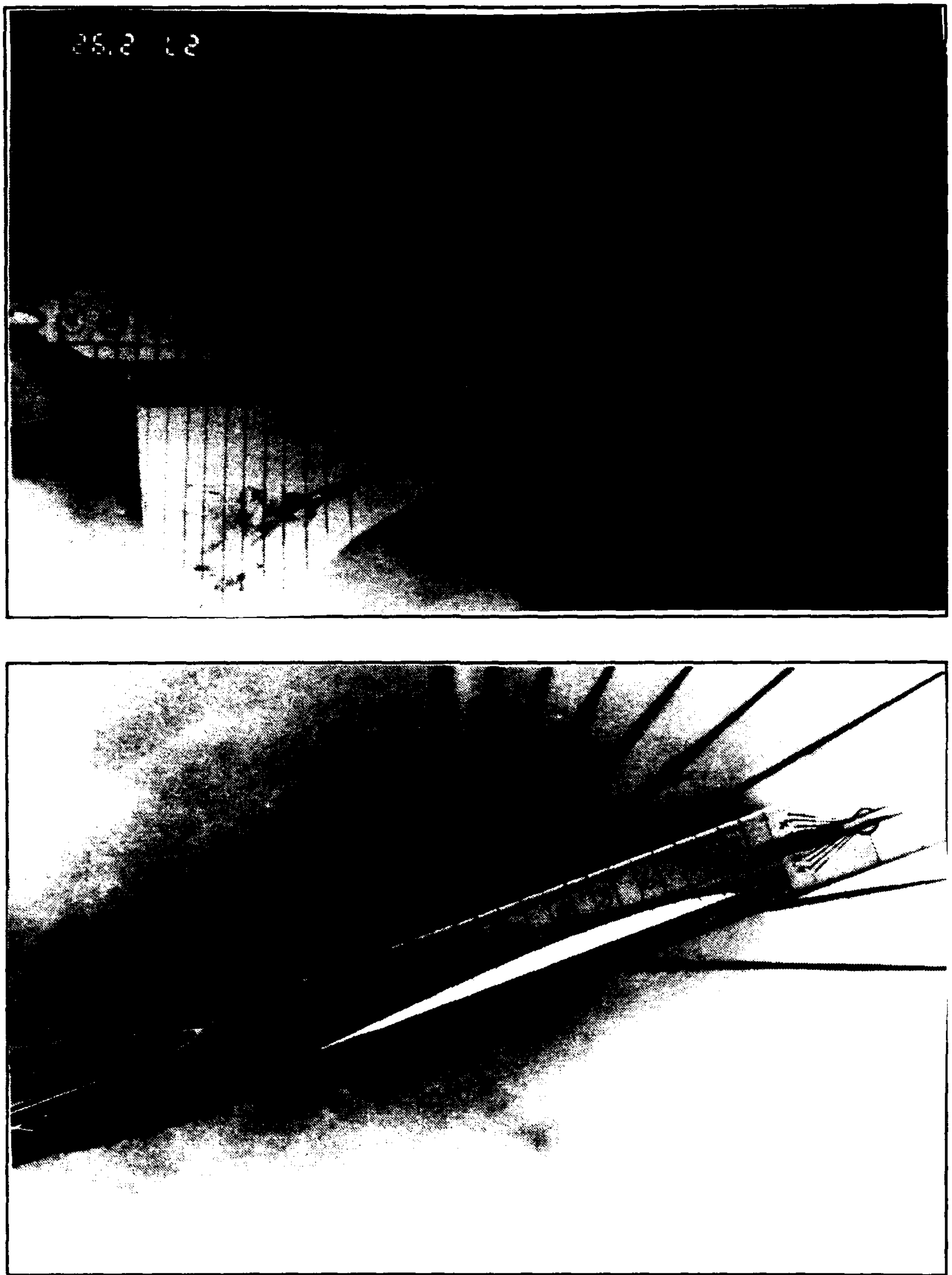

Figure 12. Wing Root Vortex Flow, Static Flow, $\alpha=20^0$, $\delta=0^0$

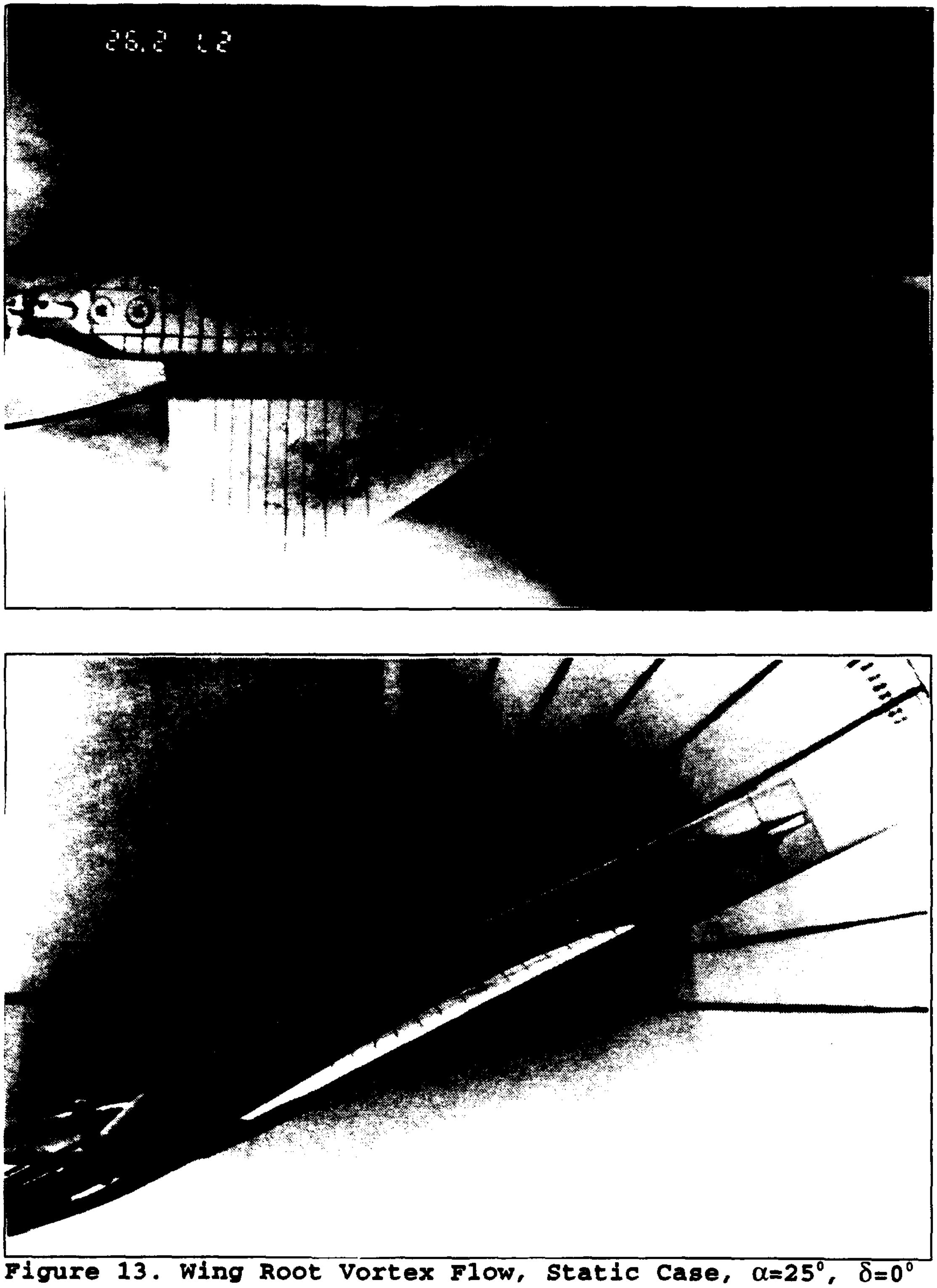

Figure 13. Wing Root Vortex Flow, Static Case, $\alpha=25^{\circ}$, $\delta=0^{\circ}$

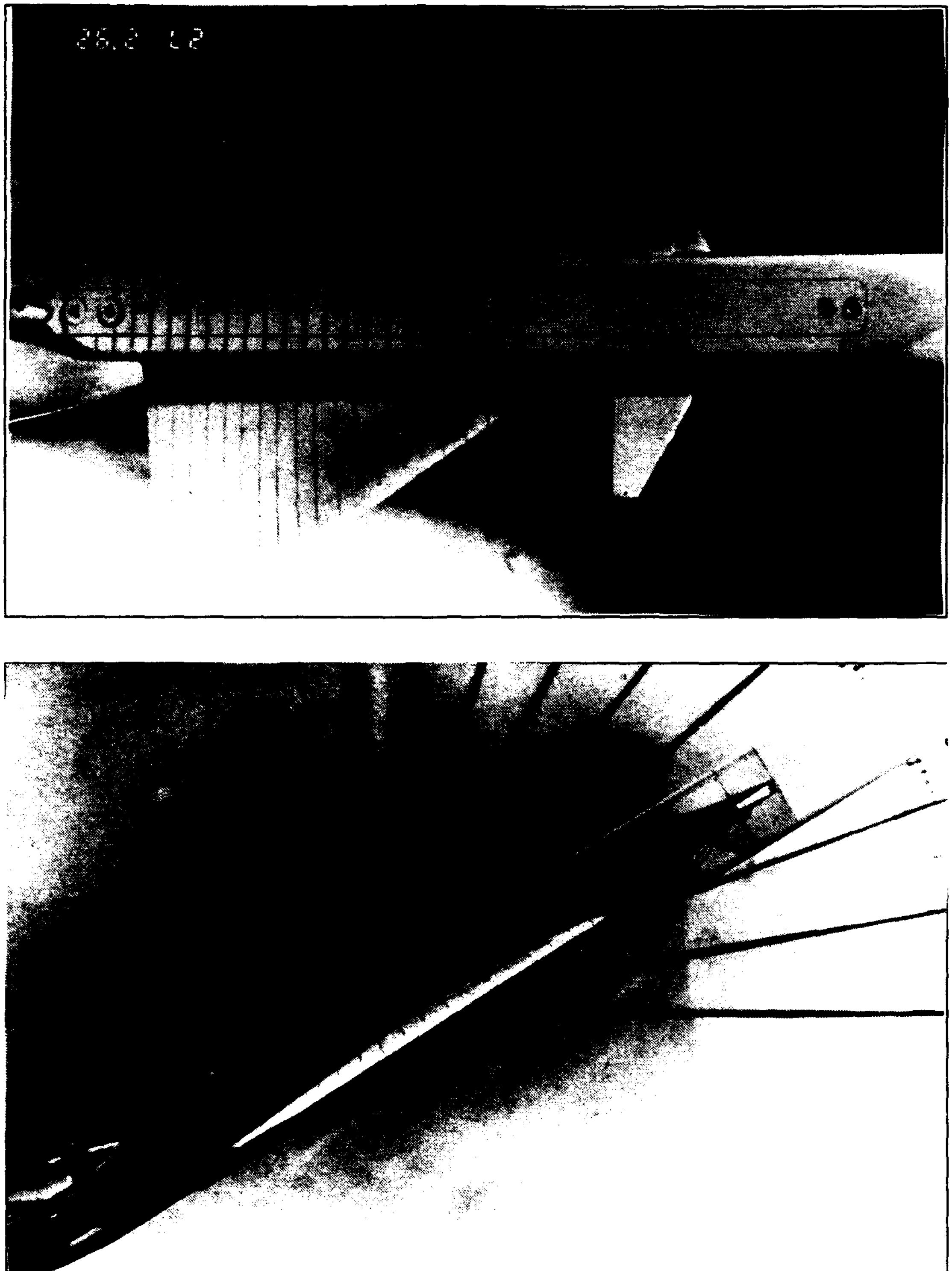

Figure 14. Wing Root Vortex Flow, Static Case, $\alpha=30^\circ$, $\delta=0^\circ$

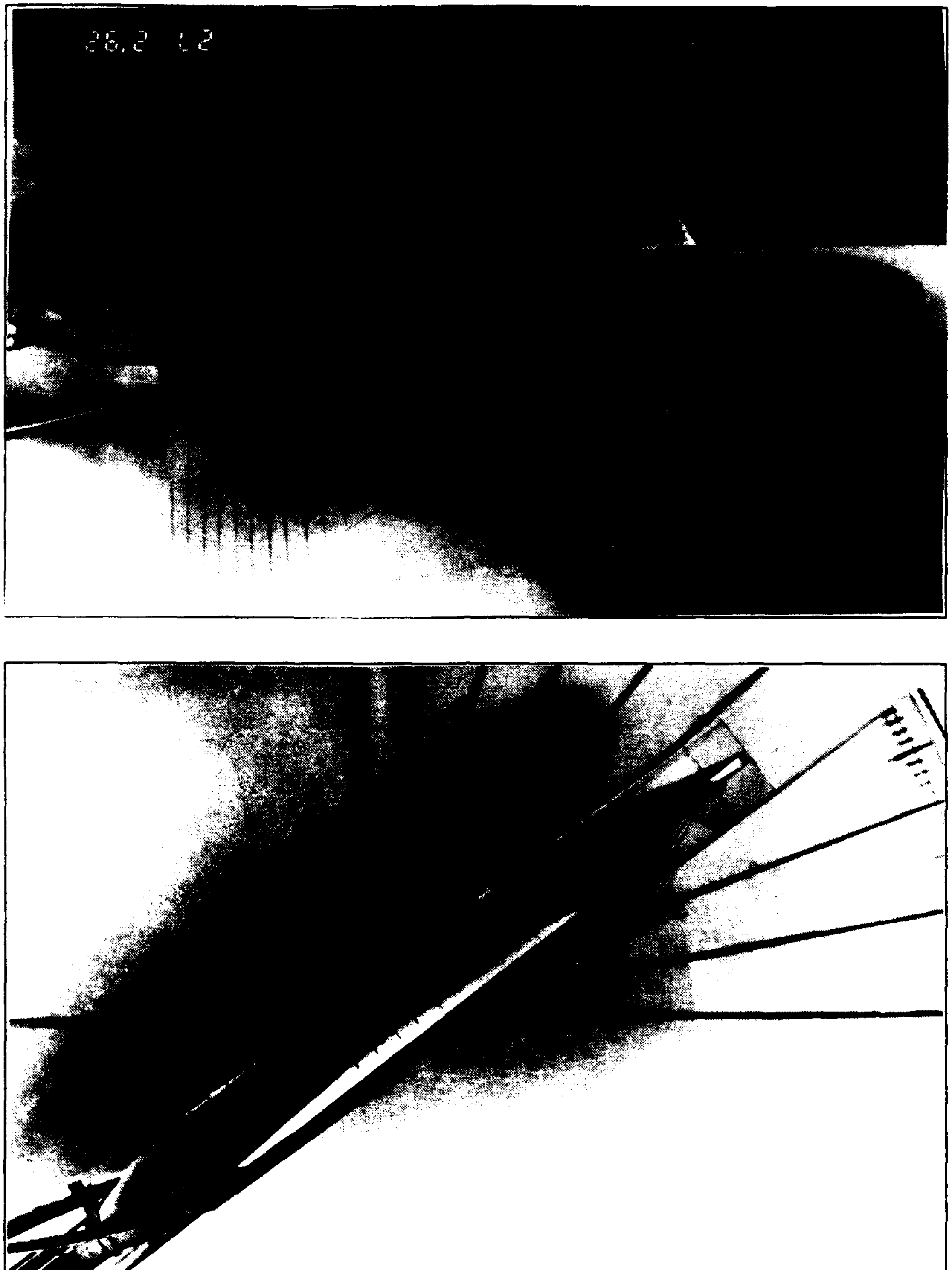

Figure 15. Wing Root Vortex Flow, Static Case, α=35°, δ=0°

Figure 16. Wing Root Vortex Flow, Static Case, $\alpha=40^{\circ}$, $\delta=0^{\circ}$

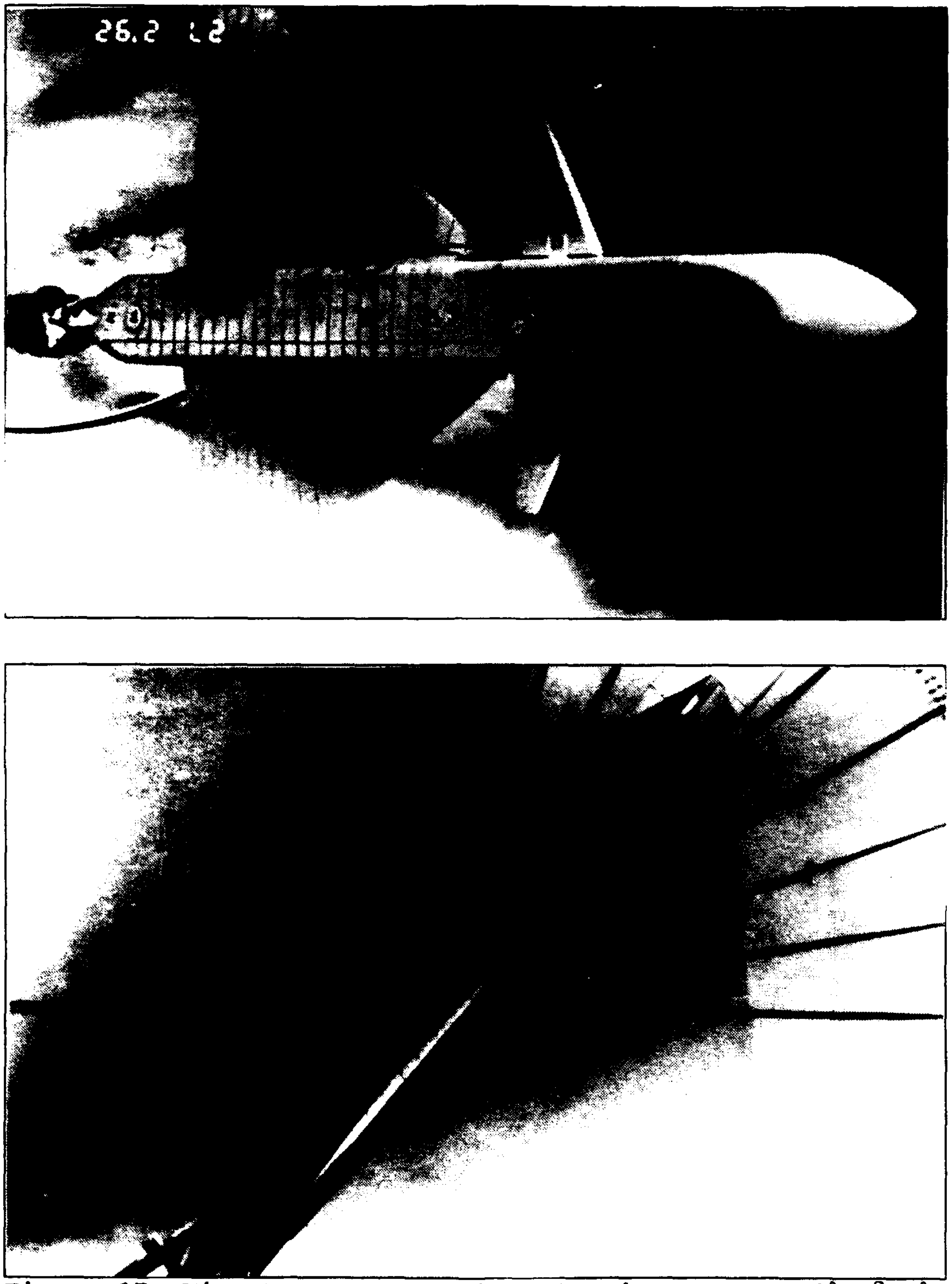

Figure 17. Wing Root Vortex Flow, Static Case, $\alpha=50^{\circ}$, $\delta=0^{\circ}$

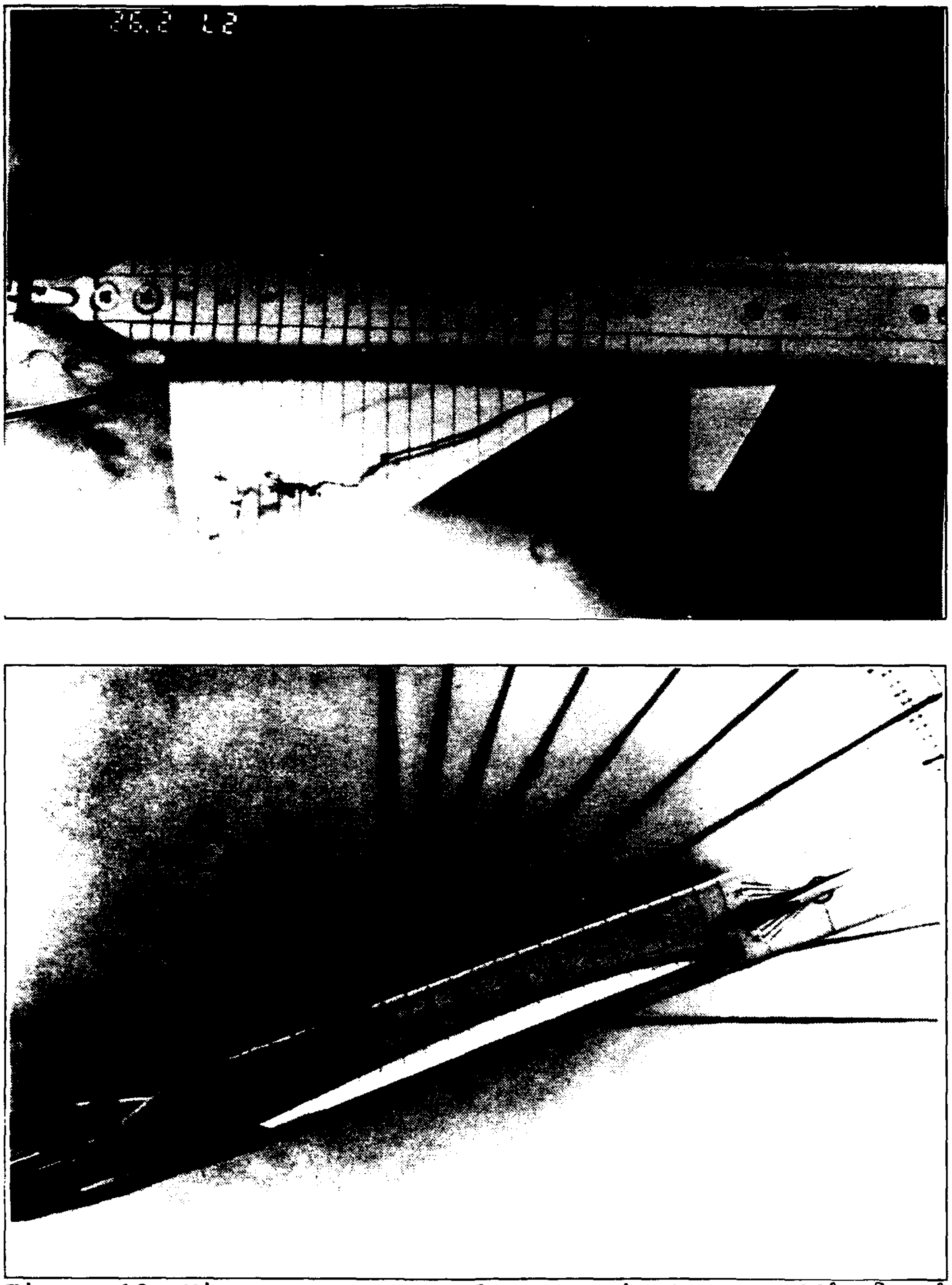

Figure 18. Wing Root Vortex Flow, Static Case, $\alpha=20^{\circ}$, $\delta=+5^{\circ}$

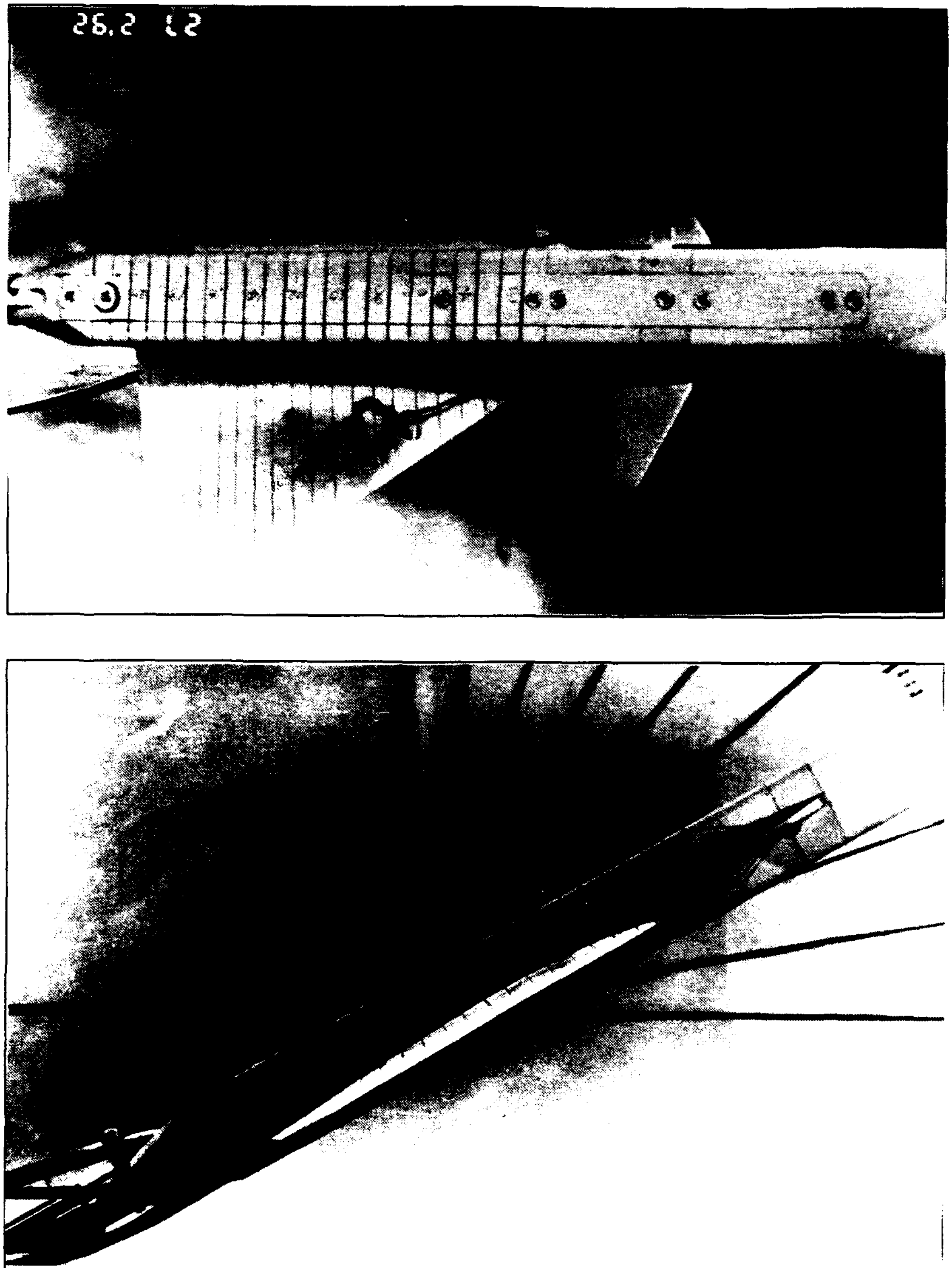

Figure 19. Wing Root Vortex Flow, Static Case, $\alpha=30^0$, $\delta=+5^0$

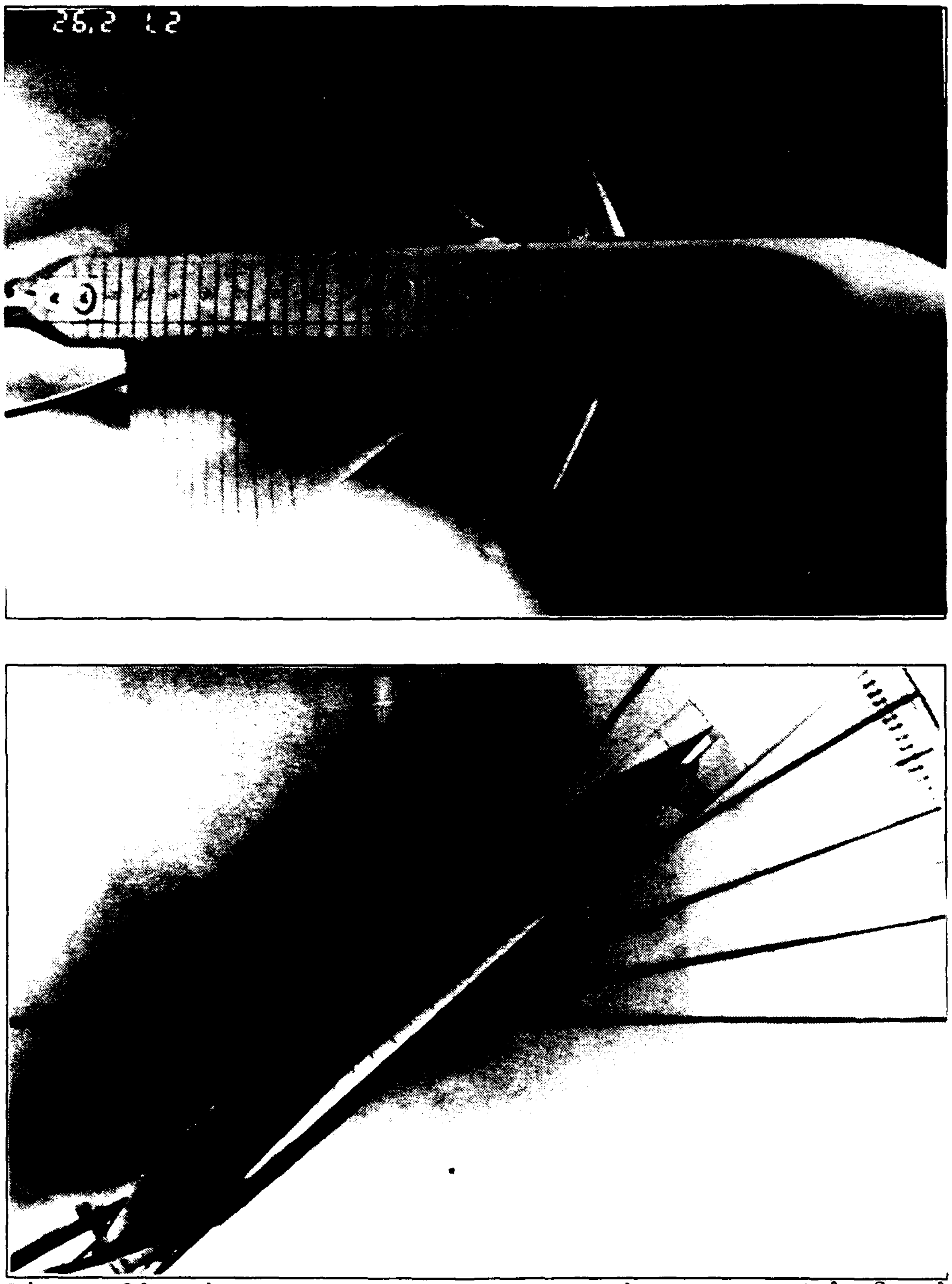

Figure 20. Wing Root Vortex Flow, Static Case, $\alpha=40^{\circ}$, $\delta=+5^{\circ}$

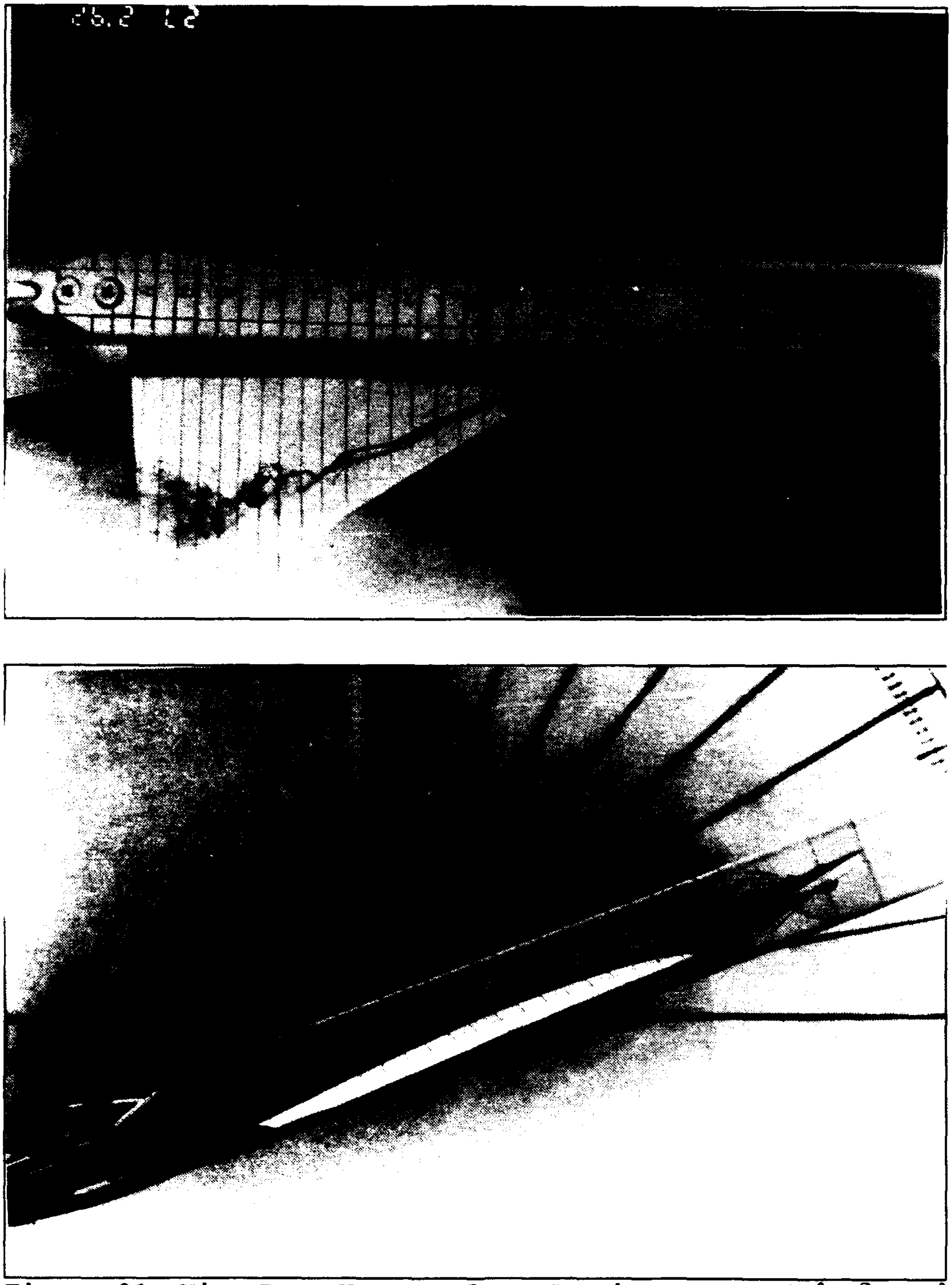

Figure 21. Wing Root Vortex Flow, Static Case, $\alpha=20^{\circ}$, $\delta=+10^{\circ}$

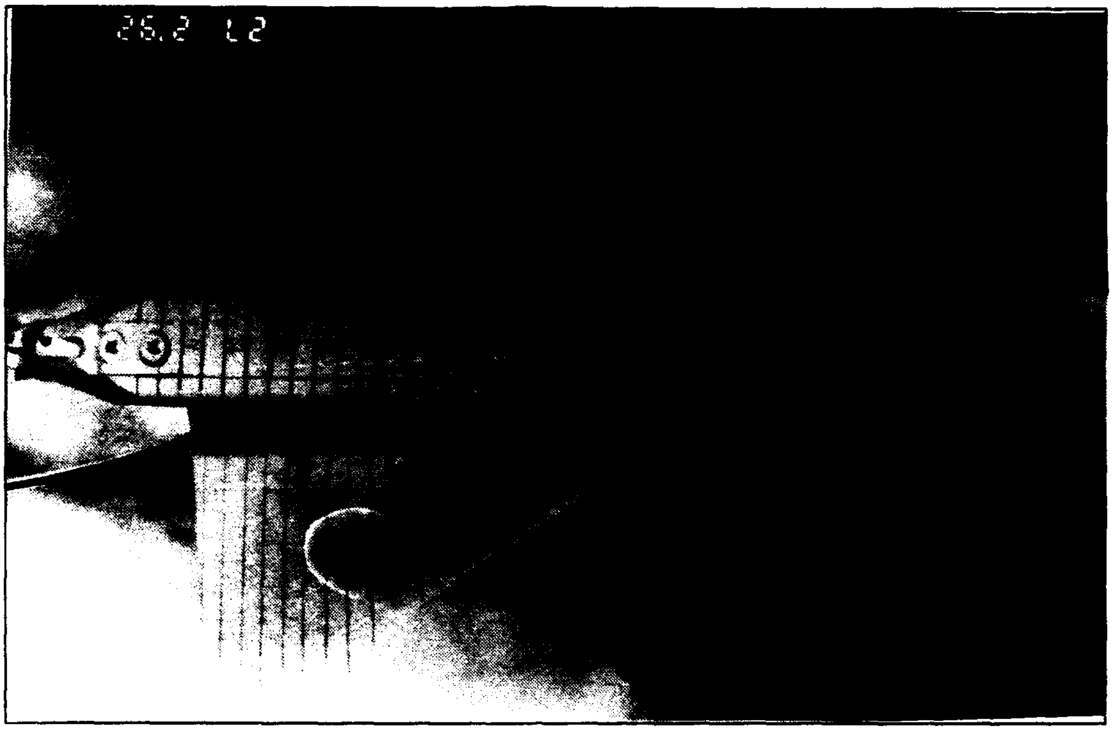

Figure 22. Wing Root Vortex Flow, Static Case, $\alpha=30^{\circ}$, $\delta=+10^{\circ}$

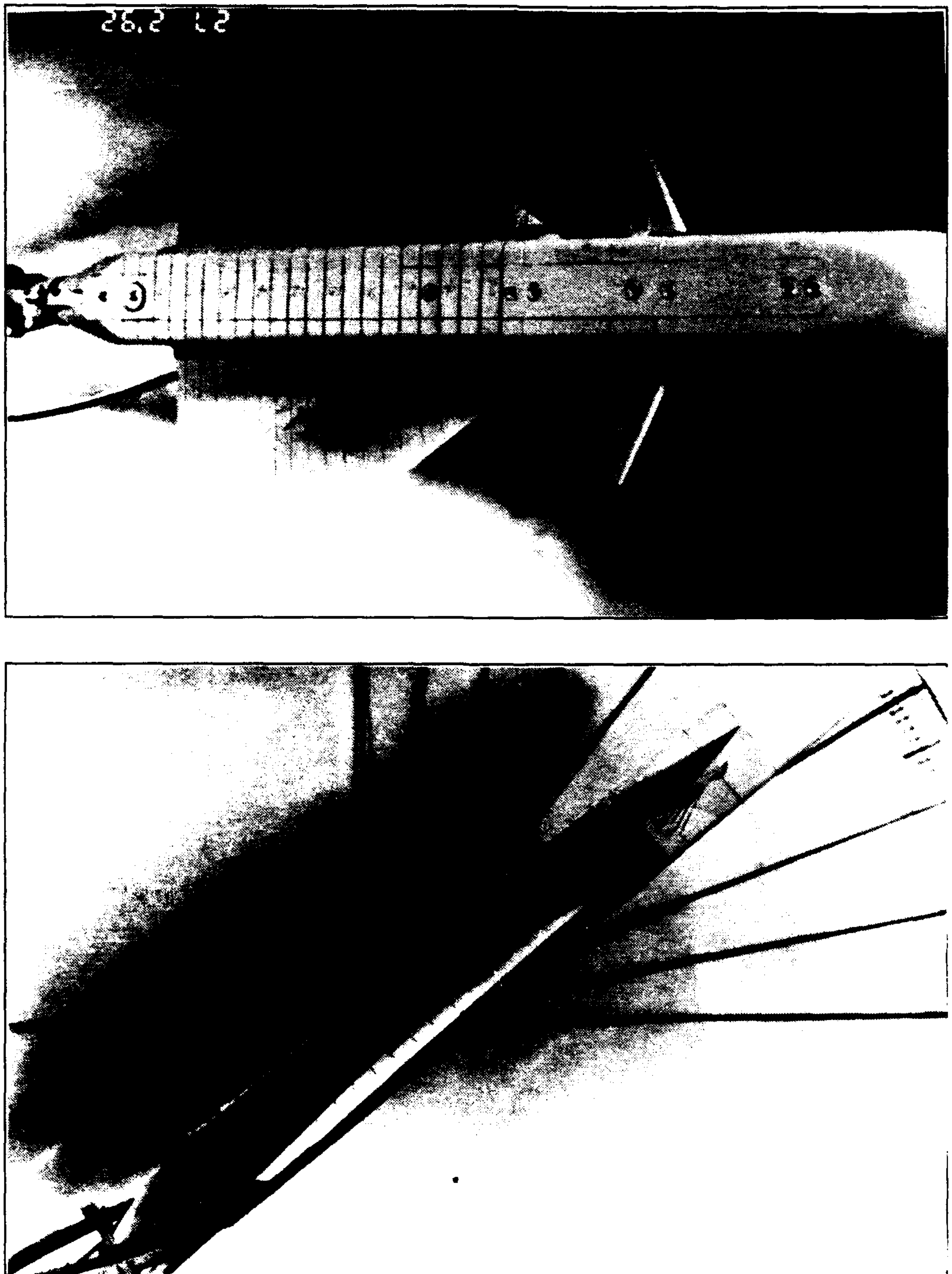

Figure 23. Wing Root Vortex Flow, Static Case, $\alpha=40^{\circ}$, $\delta=+10^{\circ}$

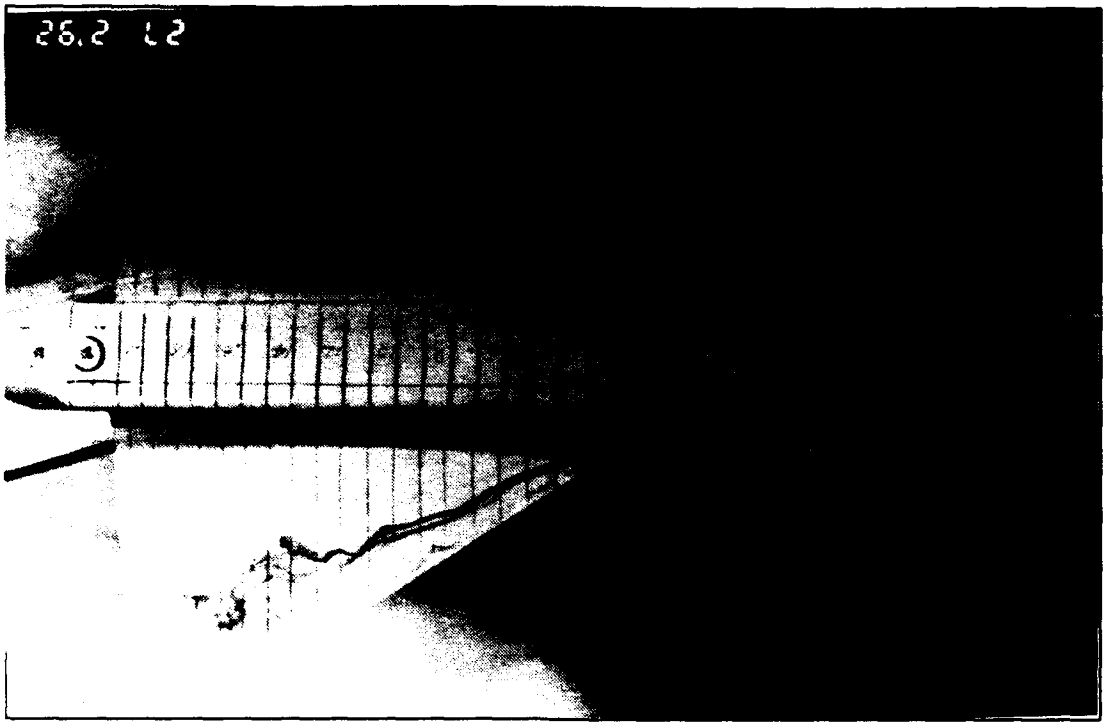

Figure 24. Wing Root Vortex Flow, Static Case, $\alpha=20^{\circ}$, $\delta=+15^{\circ}$

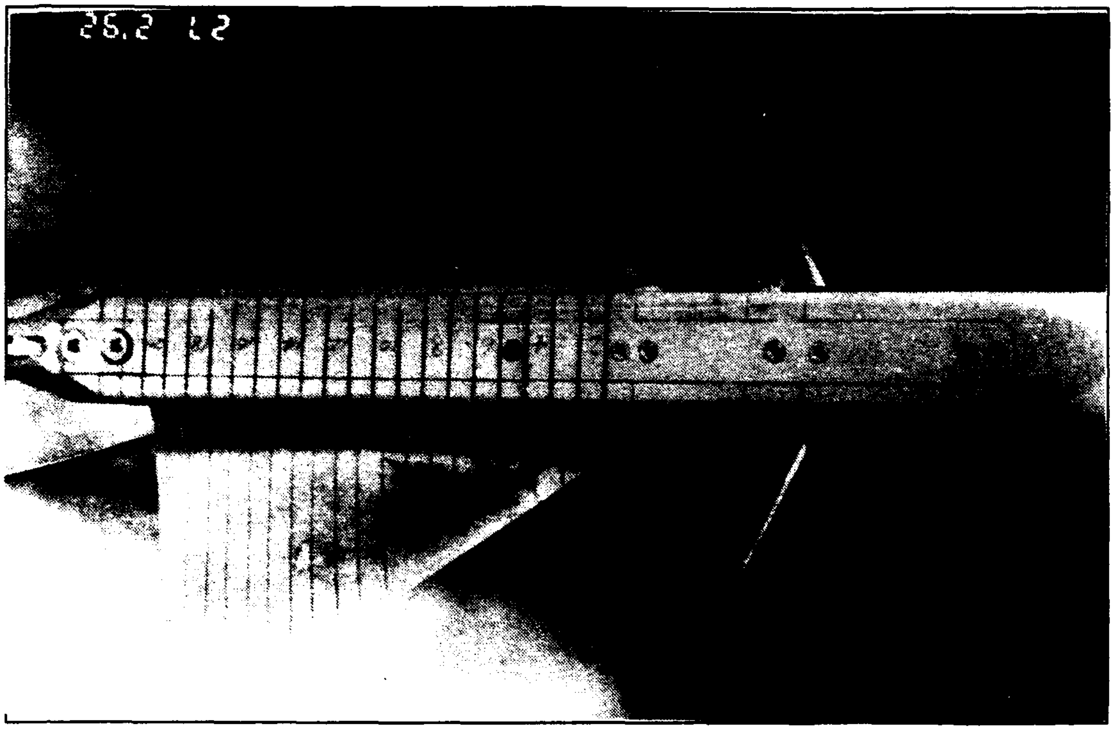

Figure 25. Wing Root Vortex Flow, Static Case, $\alpha=30^{\circ}$, $\delta=+15^{\circ}$

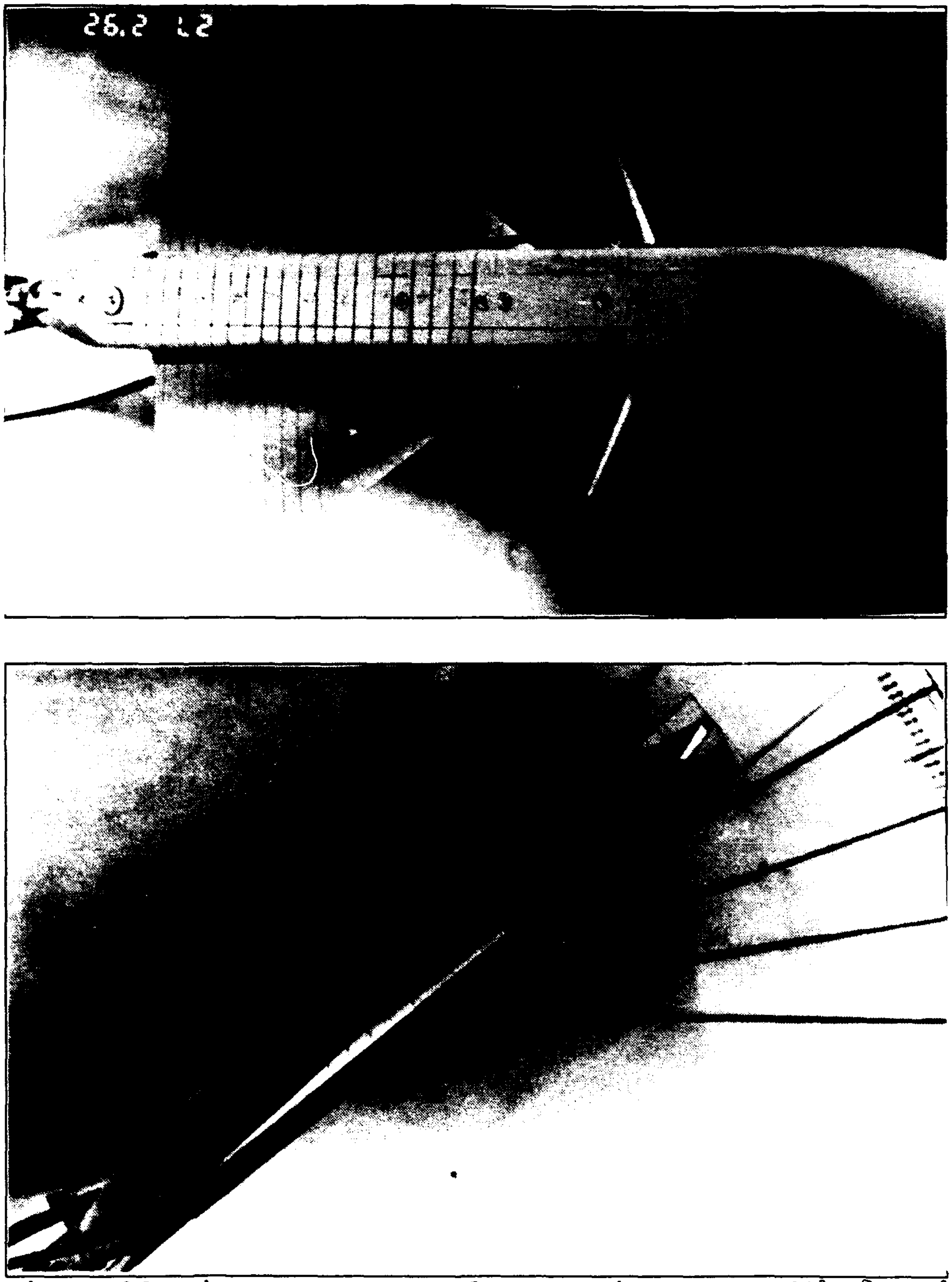

Figure 26. Wing Root Vortex Flow, Static Case, $\alpha=40^{\circ}$, $\delta=+15^{\circ}$

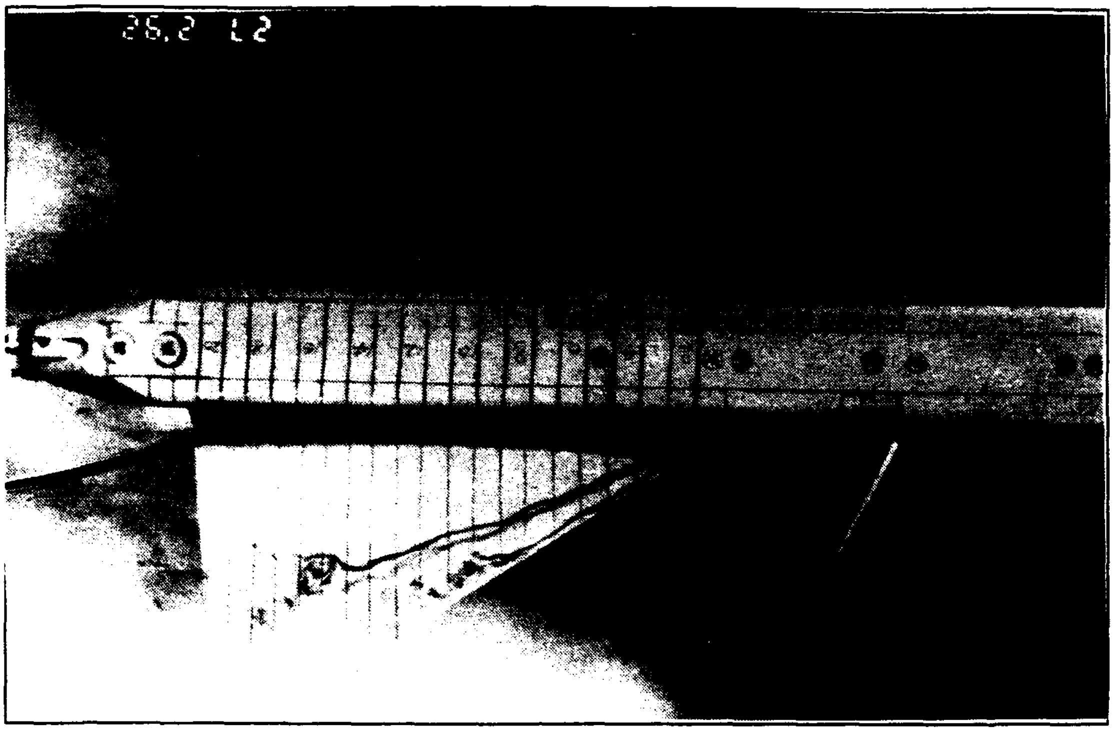

Figure 27. Wing Root Vortex Flow, Static Case, $\alpha=20^{\circ}$, $\delta=+20^{\circ}$

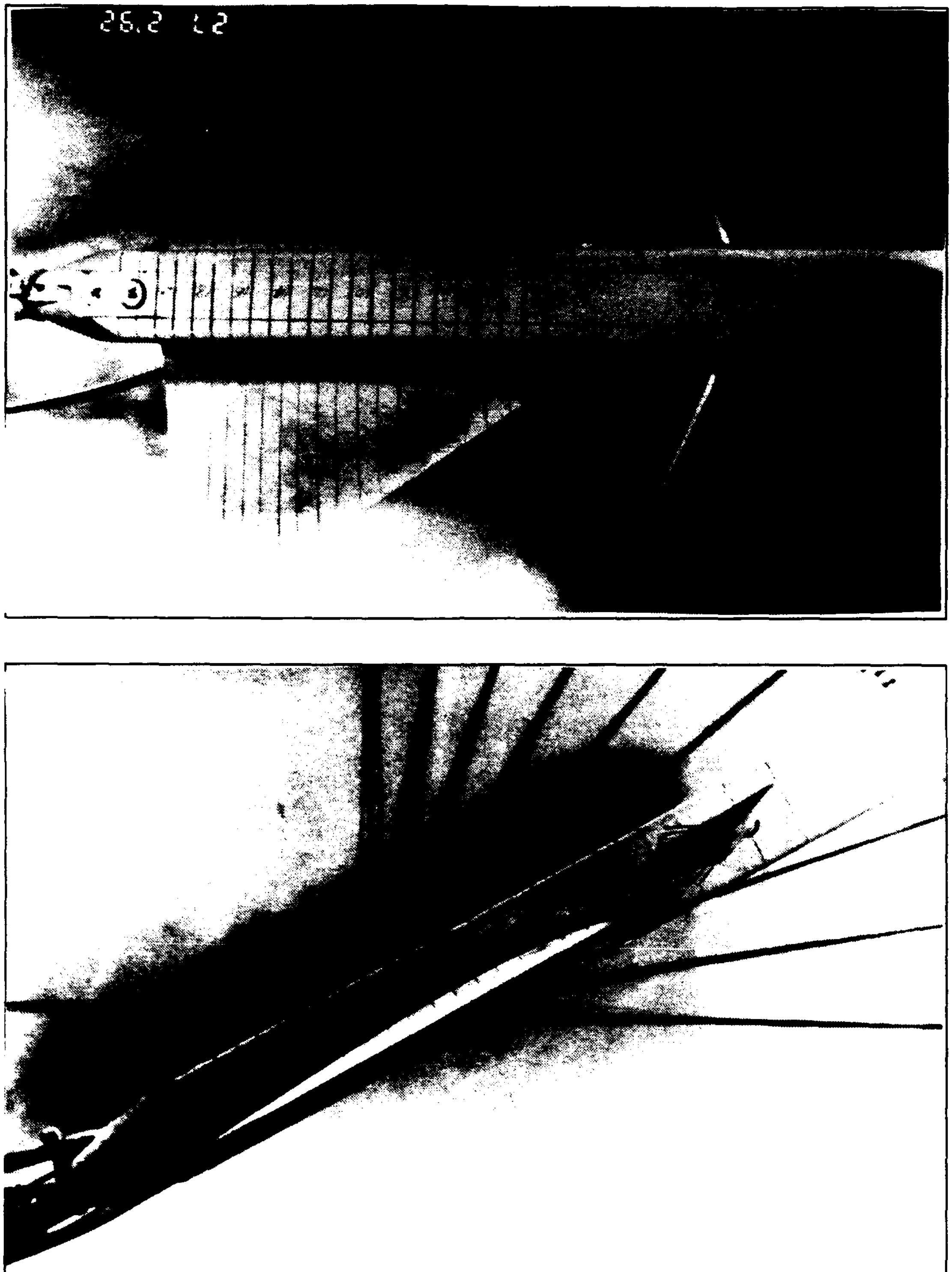

Figure 28. Wing Root Vortex Flow, Static Case, $\alpha=30^{\circ}$, $\delta=+20^{\circ}$

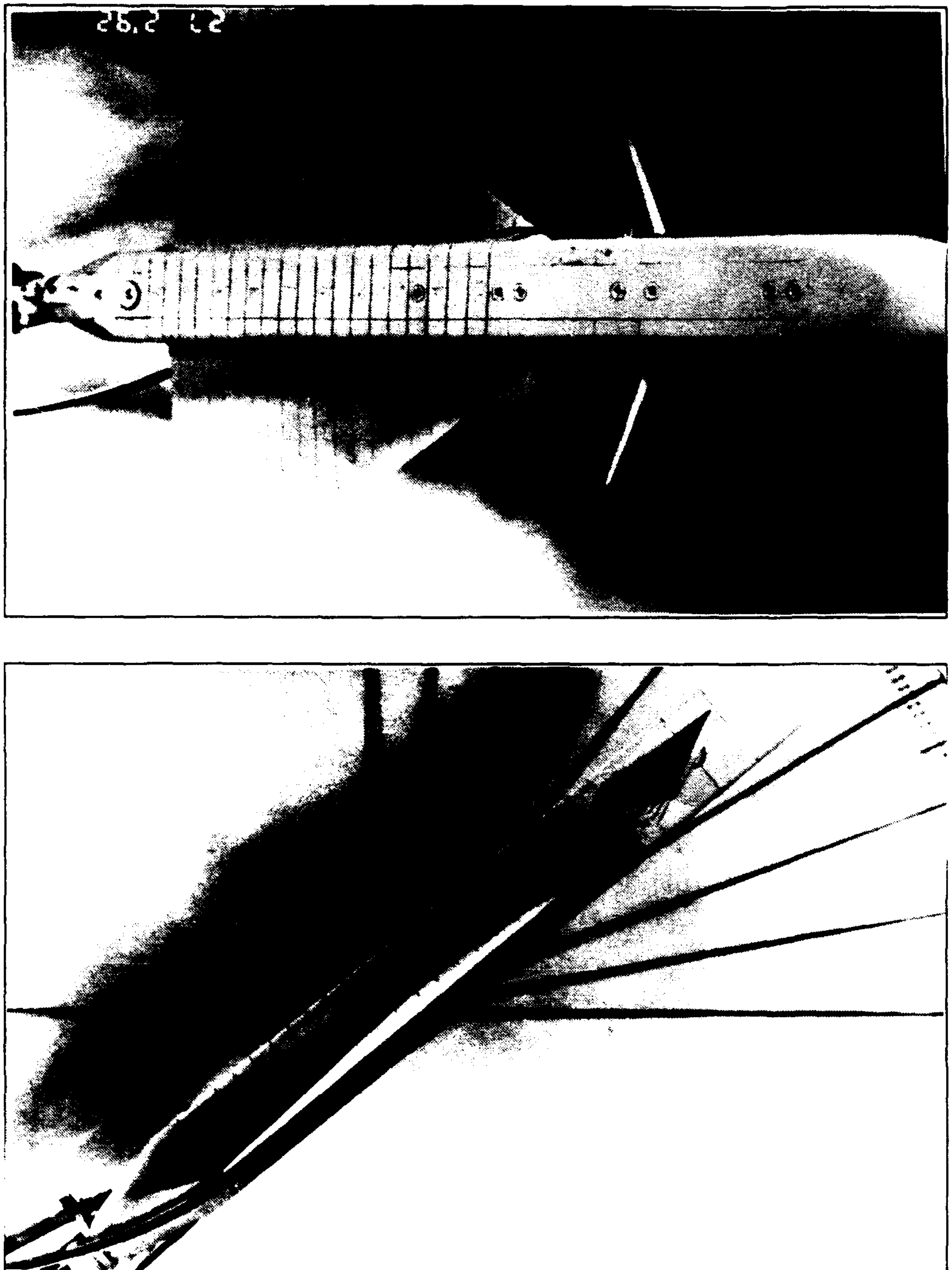

Figure 29. Wing Root Vortex Flow, Static Case, $\alpha=40^{\circ}$, $\delta=+20^{\circ}$

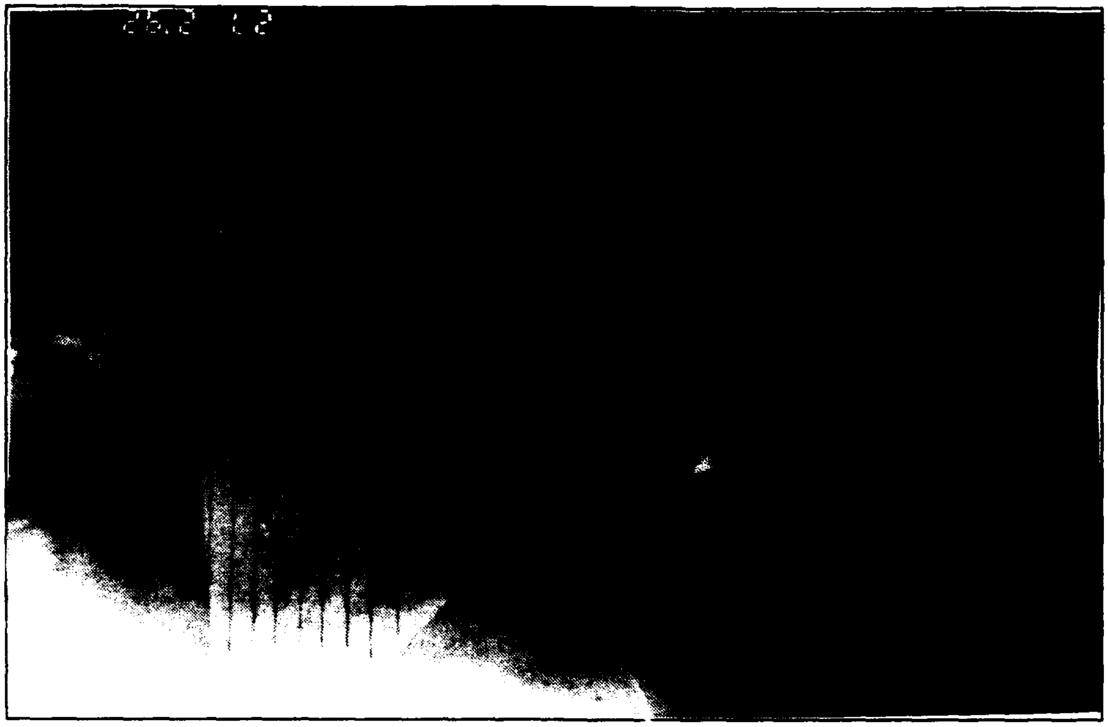

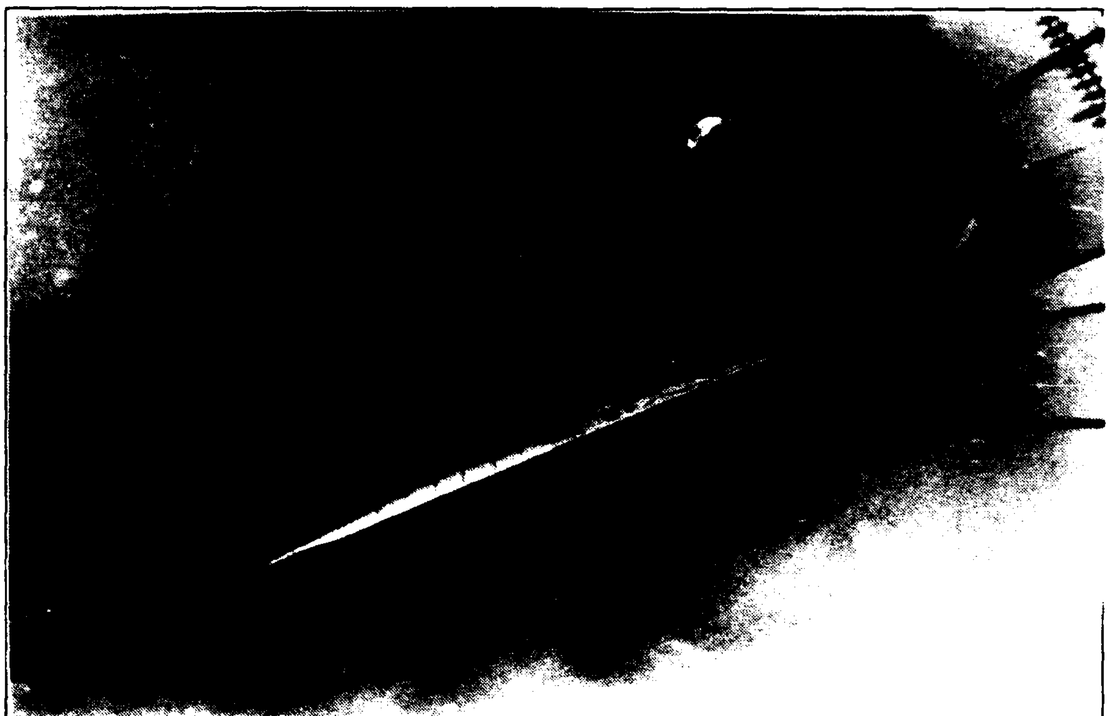

Figure 30. Wing Root Vortex Flow, Static Case, $\alpha=20^{\circ}$, $\delta=+25^{\circ}$

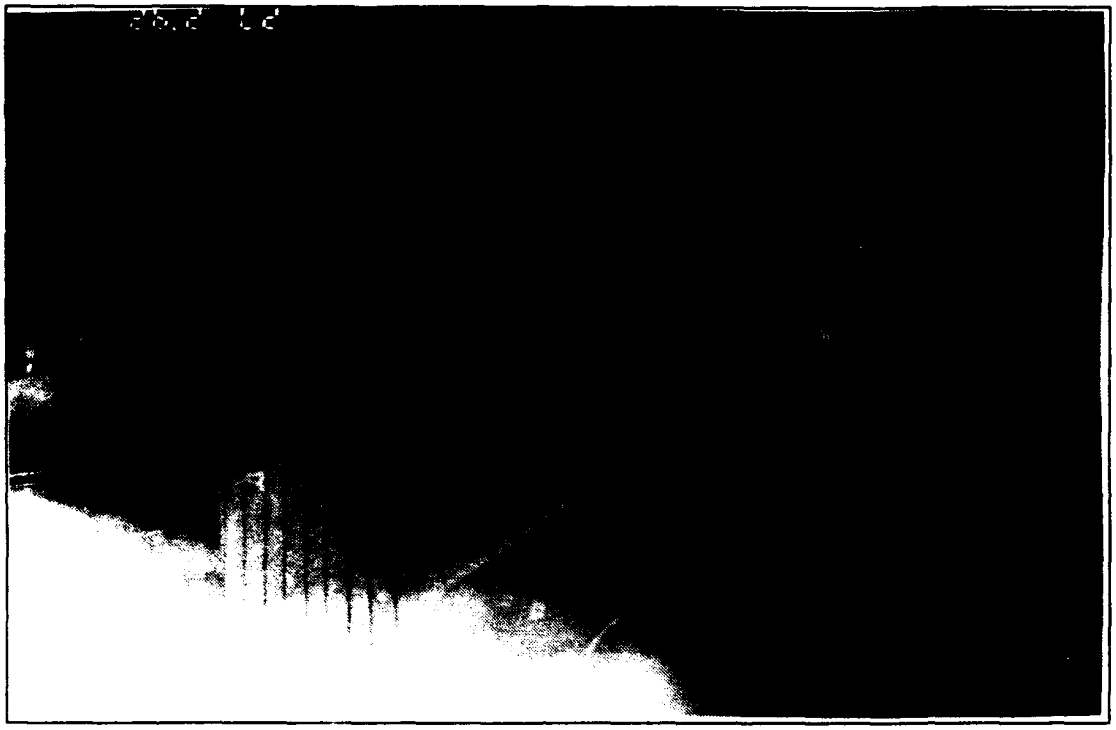

Figure 31. Wing Root Vortex Flow, Static Case, $\alpha=30^\circ$, $\delta=+25^\circ$

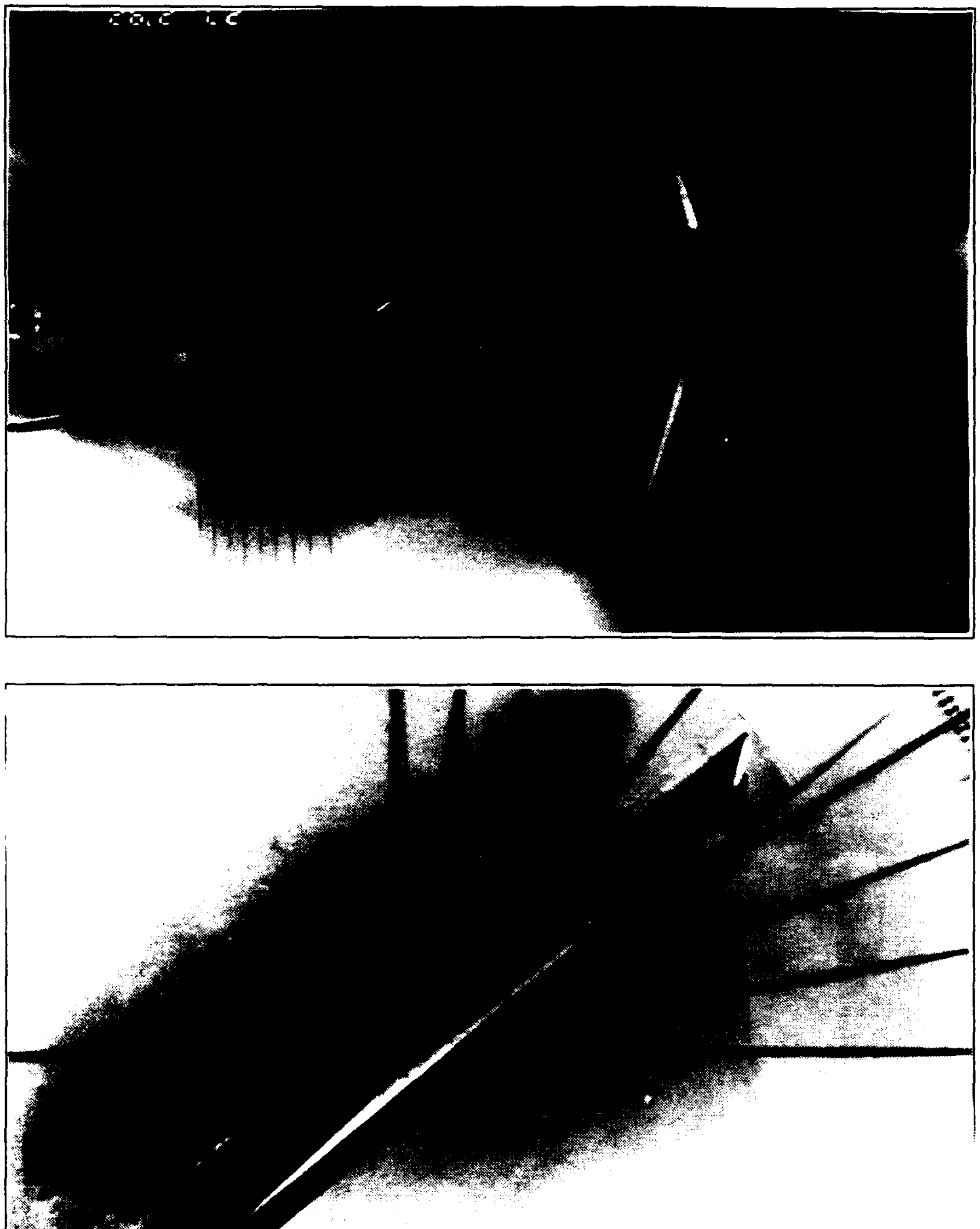

Figure 32. Wing Root Vortex Flow, Static Case, $\alpha=40^{0}$, $\delta=+25^{0}$

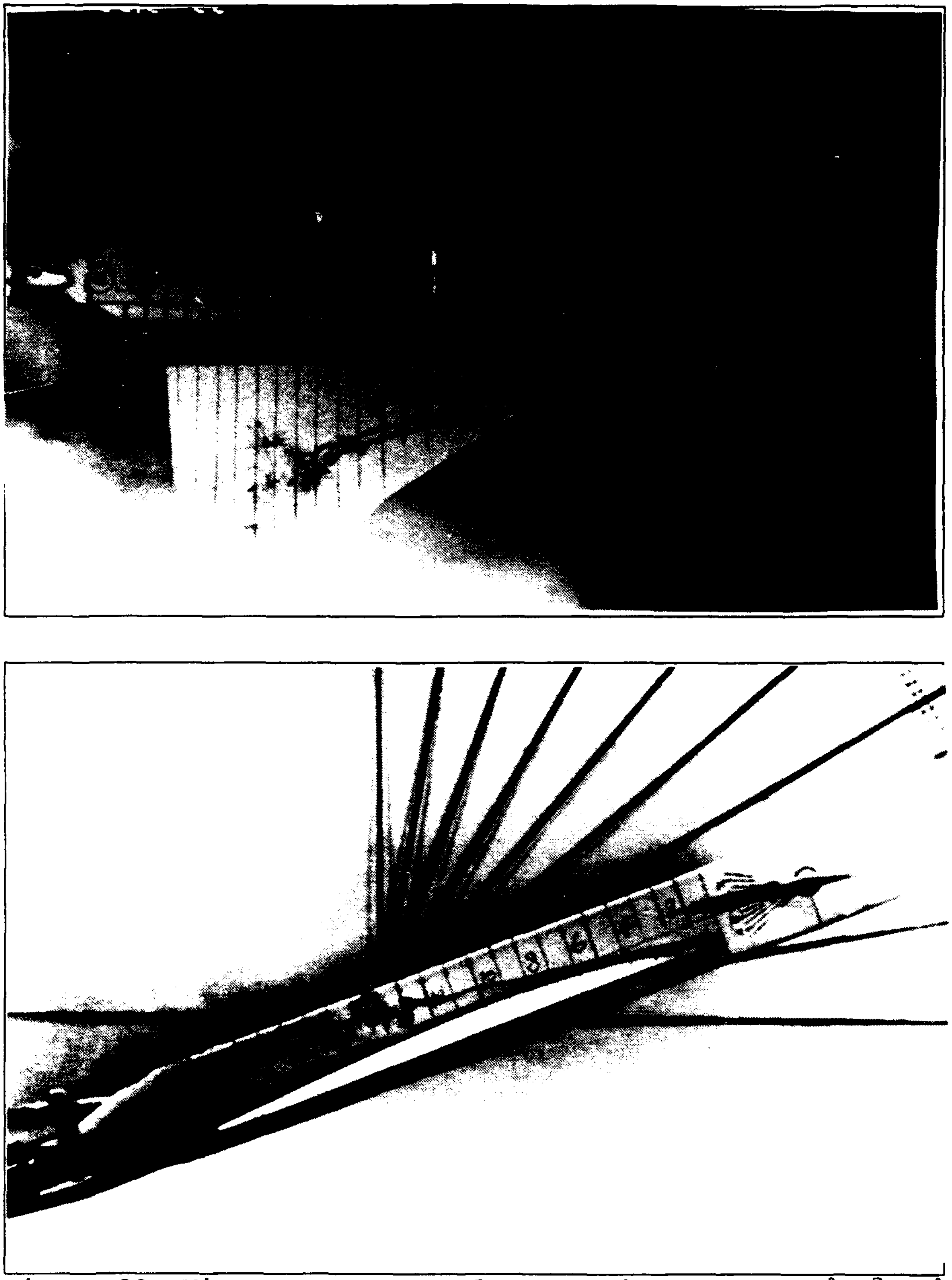

Figure 33. Wing Root Vortex Flow, Static Case, $\alpha=20^{\circ}$, $\delta=-5^{\circ}$

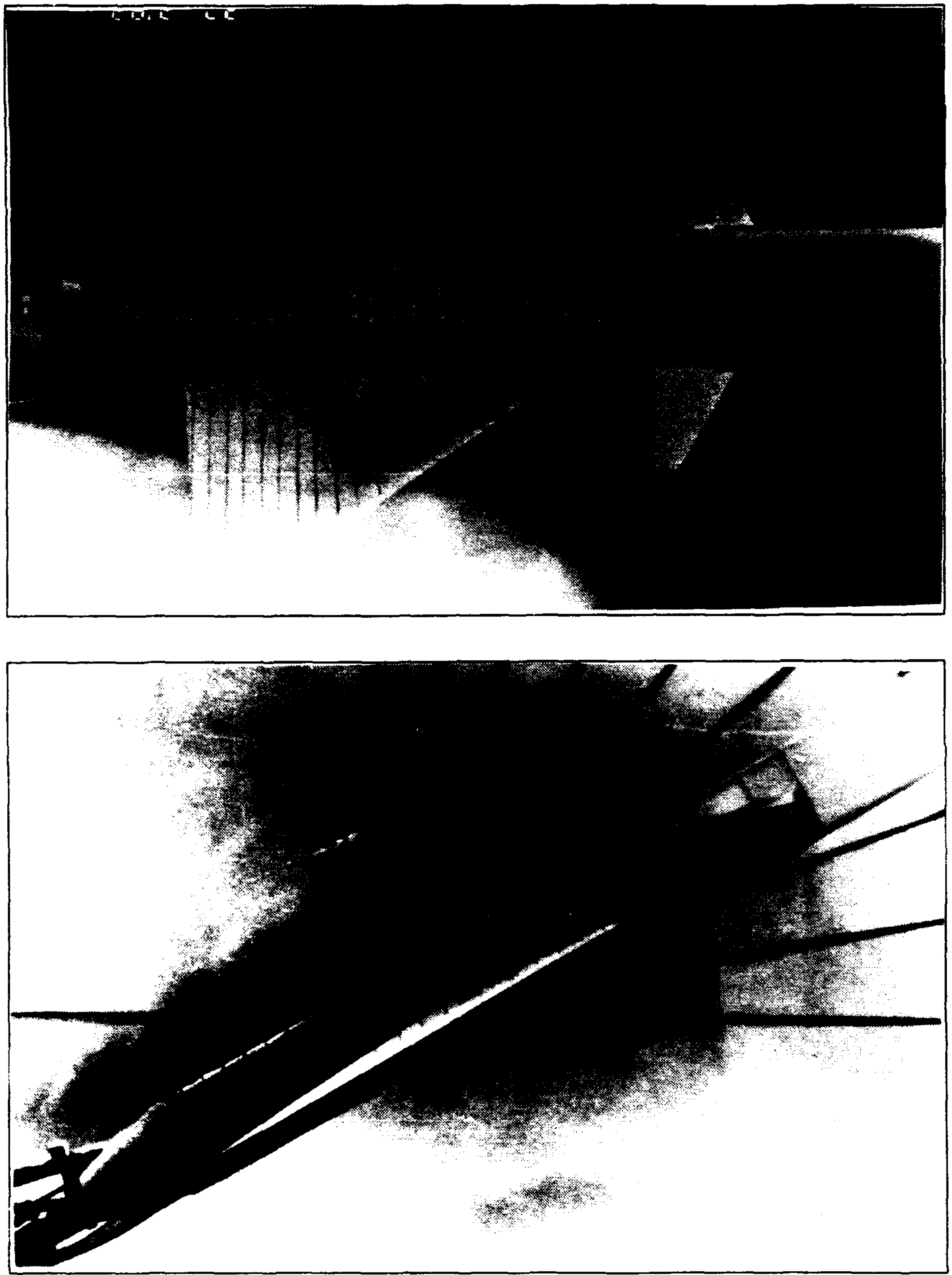

Figure 34. Wing Root Vortex Flow, Static Case, $\alpha=30^{\circ}$, $\delta=-5^{\circ}$

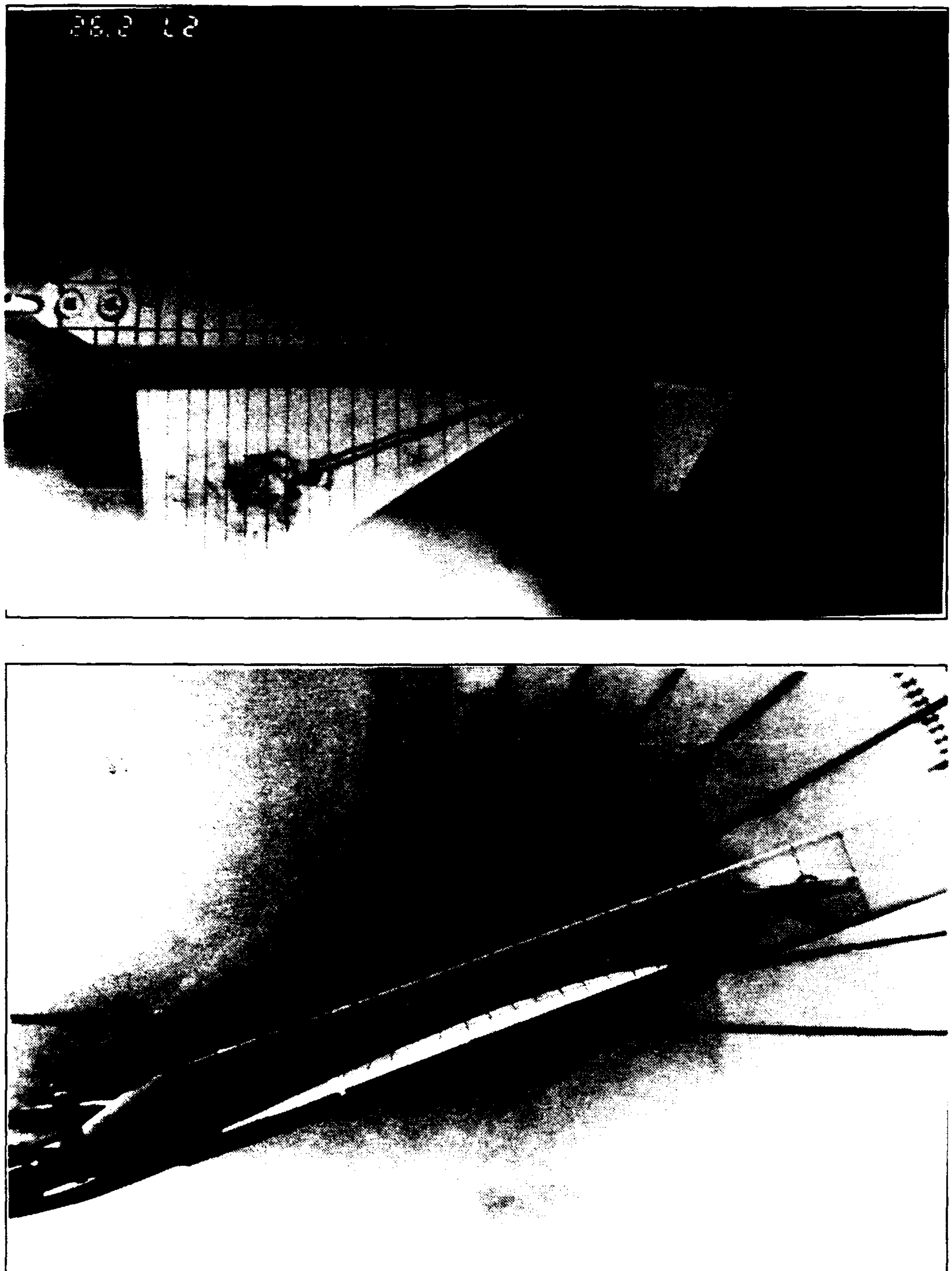

Figure 35. Wing Root Vortex Flow, Static Case, $\alpha=20^{\circ}$, $\delta=-10^{\circ}$

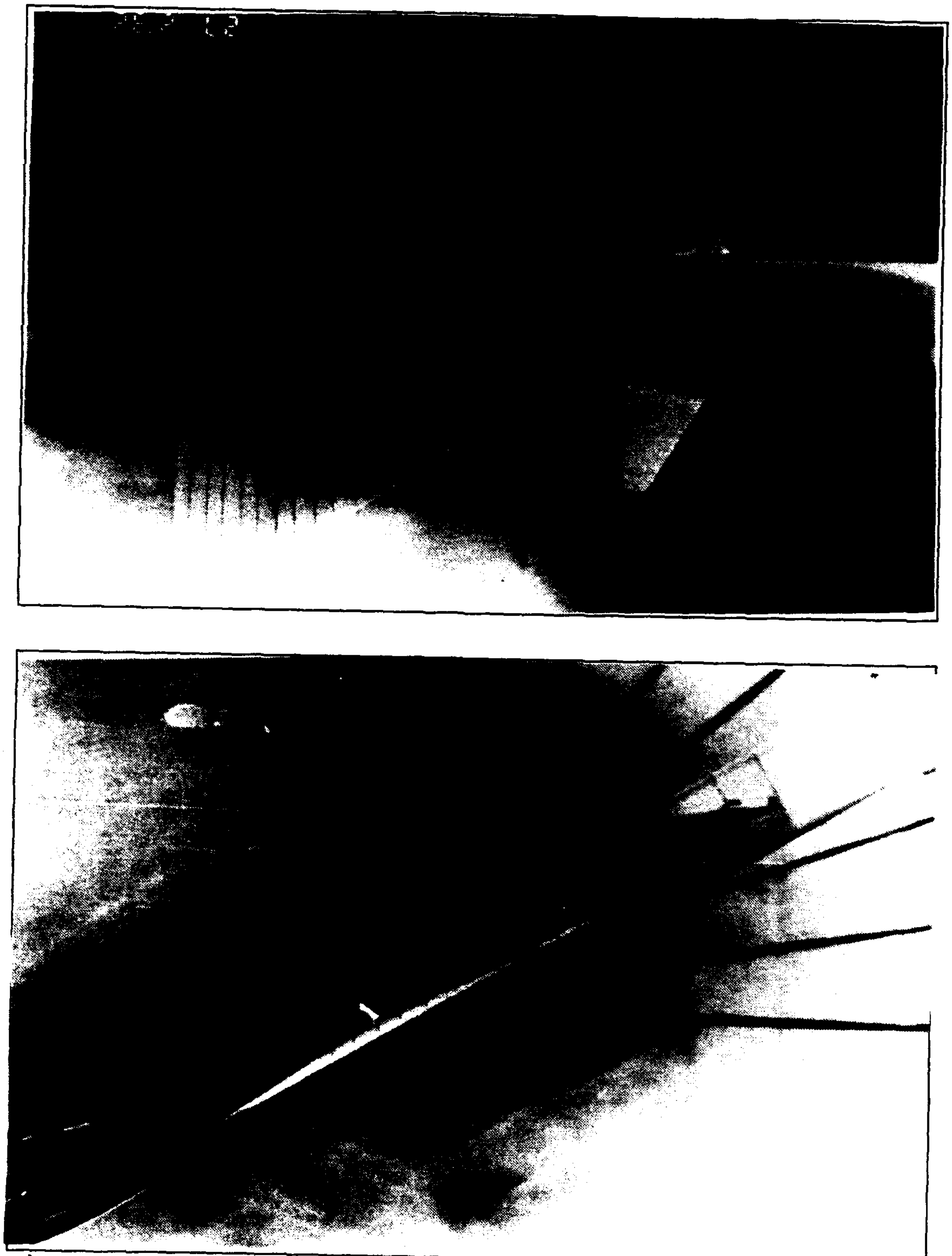

Figure 36. Wing Root Vortex Flow, Static Case, $\alpha=30^{0}$, $\delta=-10^{0}$

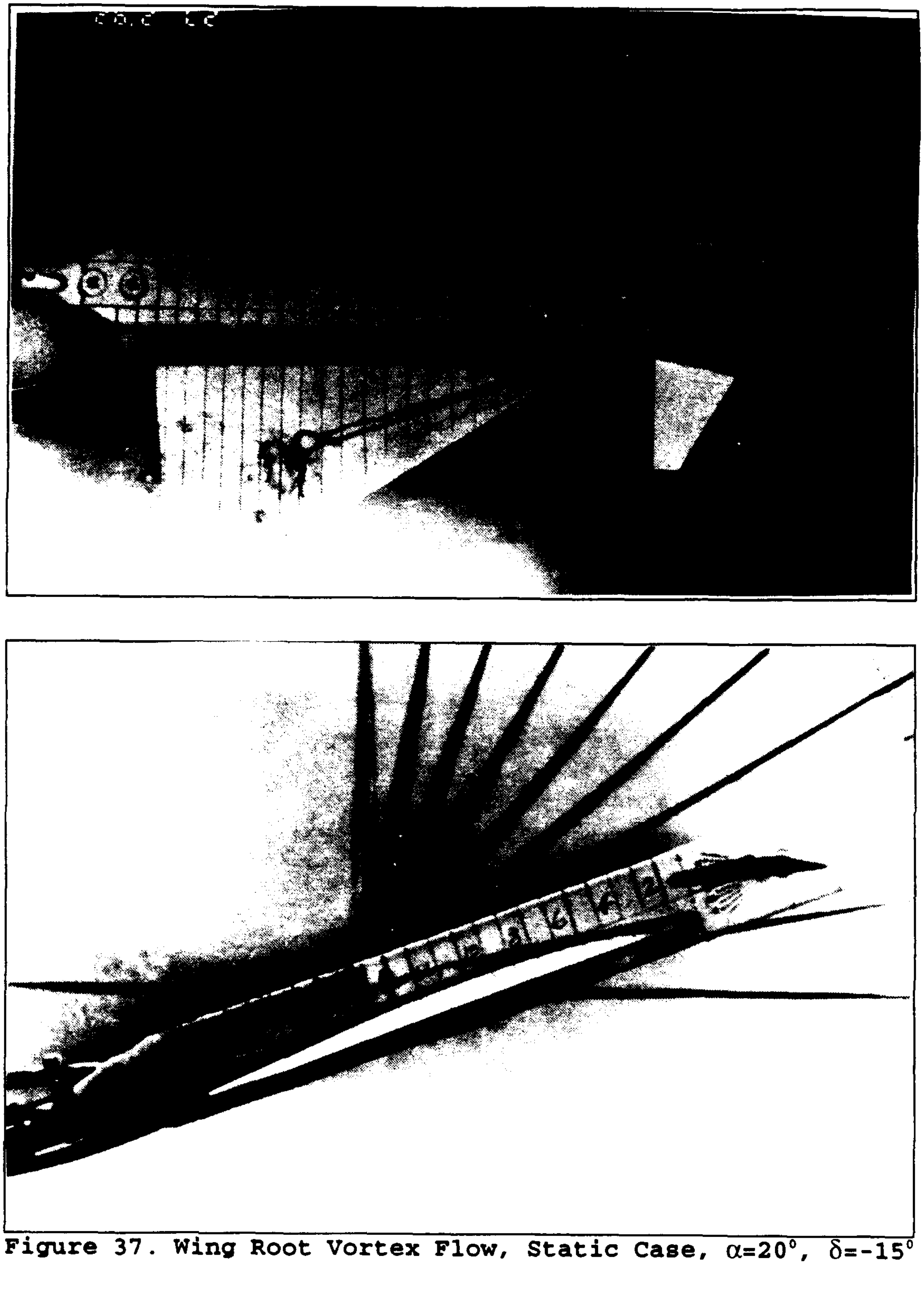

Figure 37. Wing Root Vortex Flow, Static Case, $\alpha=20°$, $\delta=-15°$

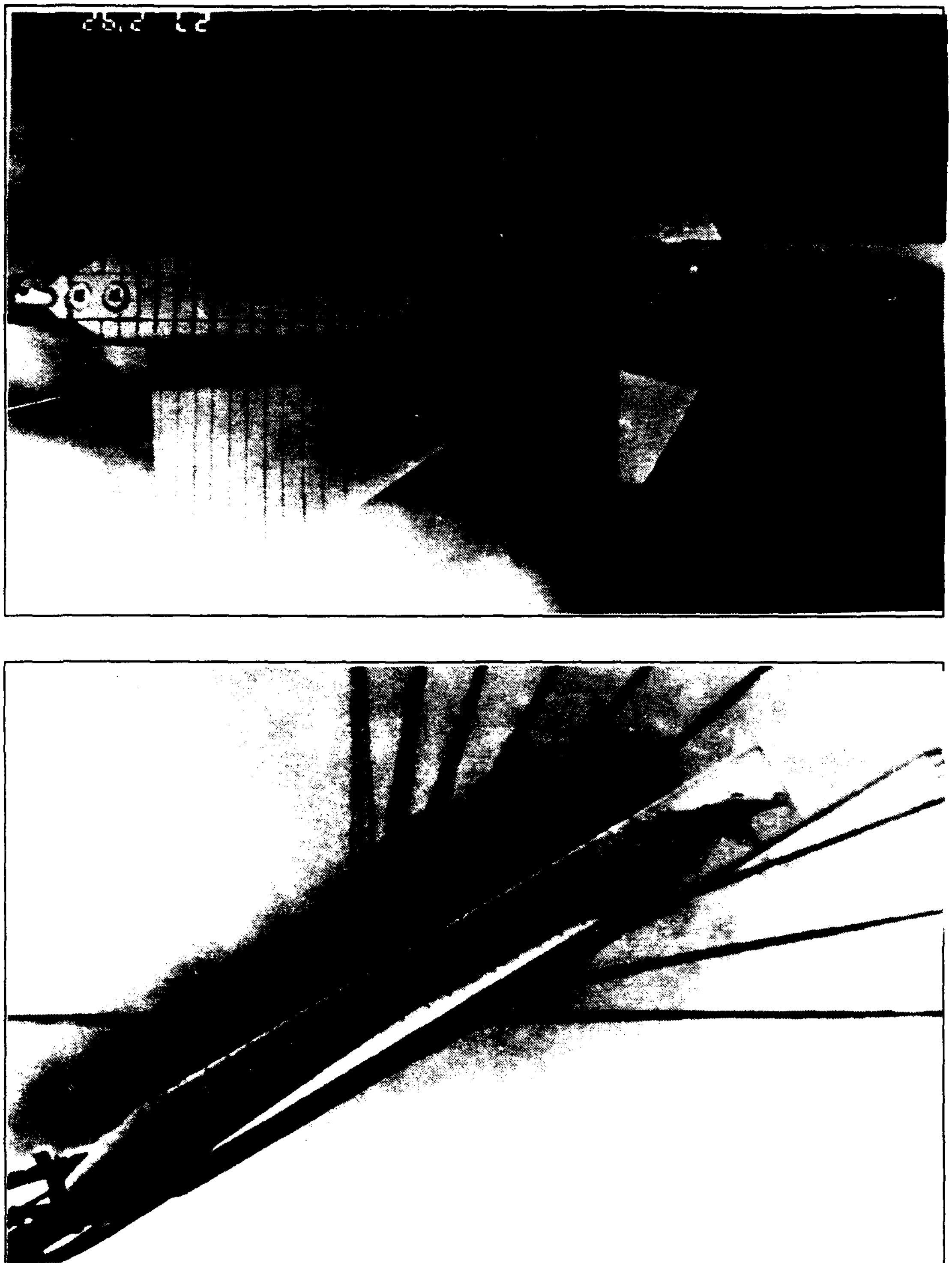

Figure 38. Wing Root Vortex Flow, Static Case, $\alpha=30^{\circ}$, $\delta=-15^{\circ}$

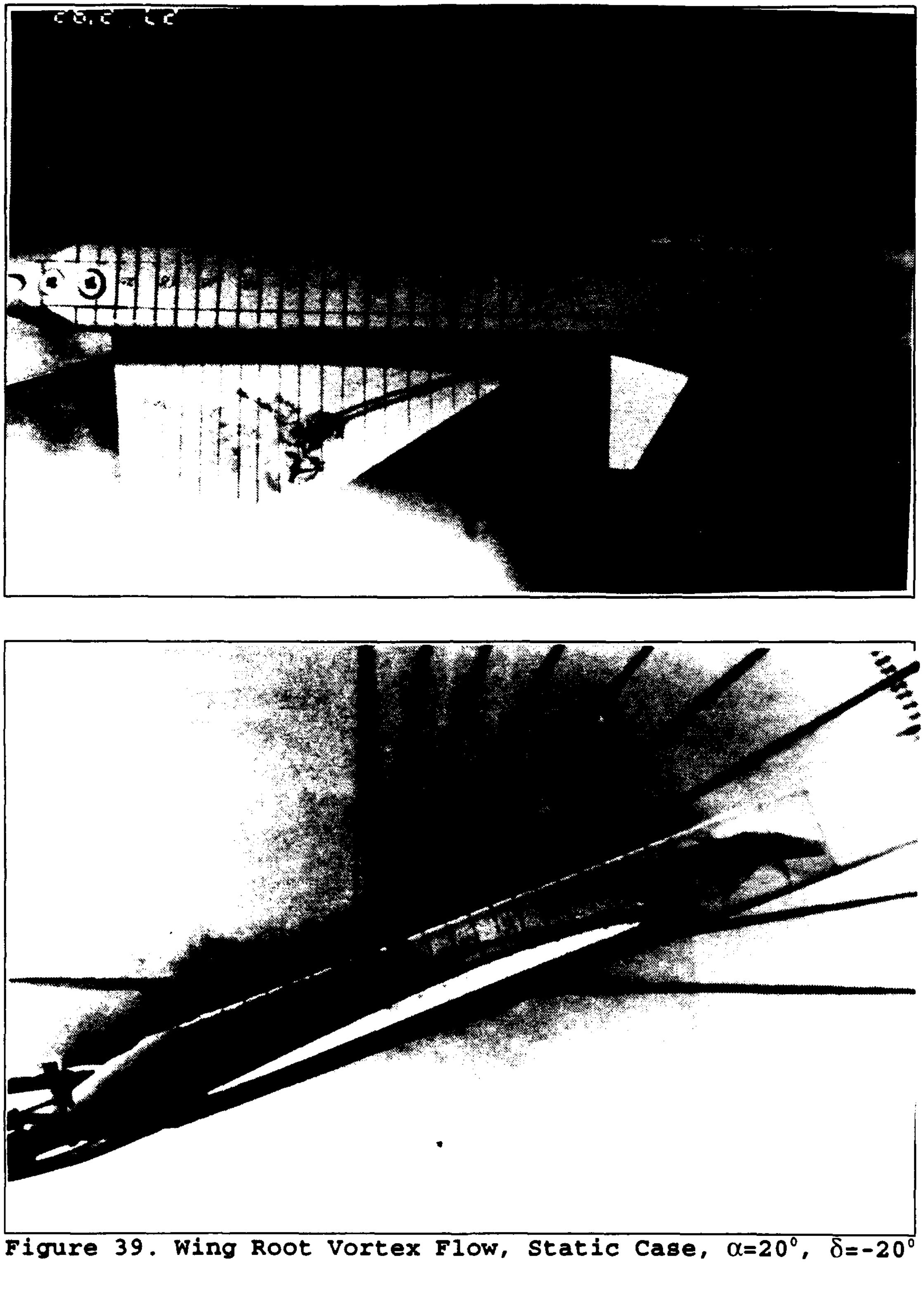

Figure 39. Wing Root Vortex Flow, Static Case, $\alpha=20^{\circ}$, $\delta=-20^{\circ}$

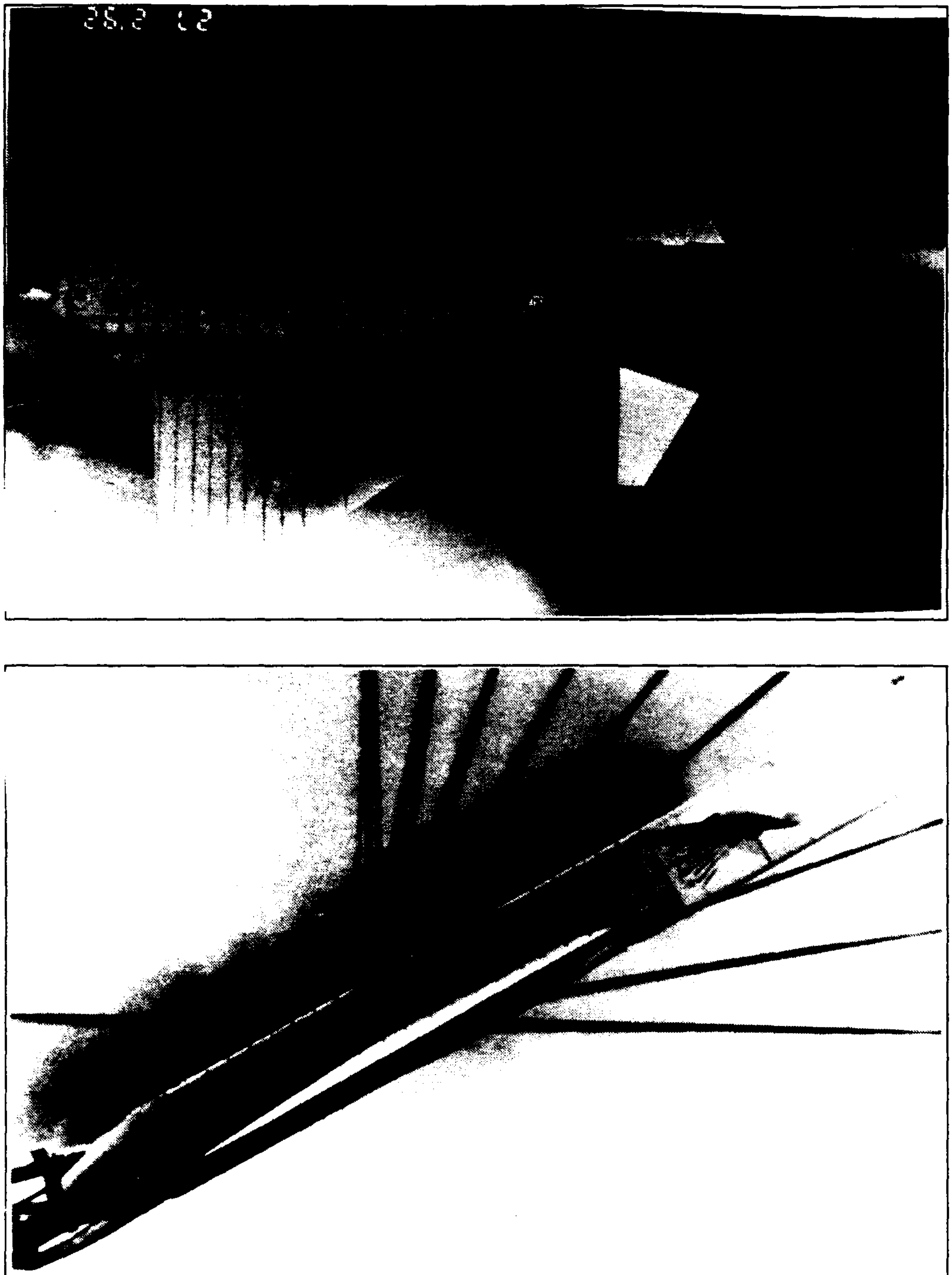

Figure 40. Wing Root Vortex Flow, Static Case, $\alpha=30^\circ$, $\delta=-20^\circ$

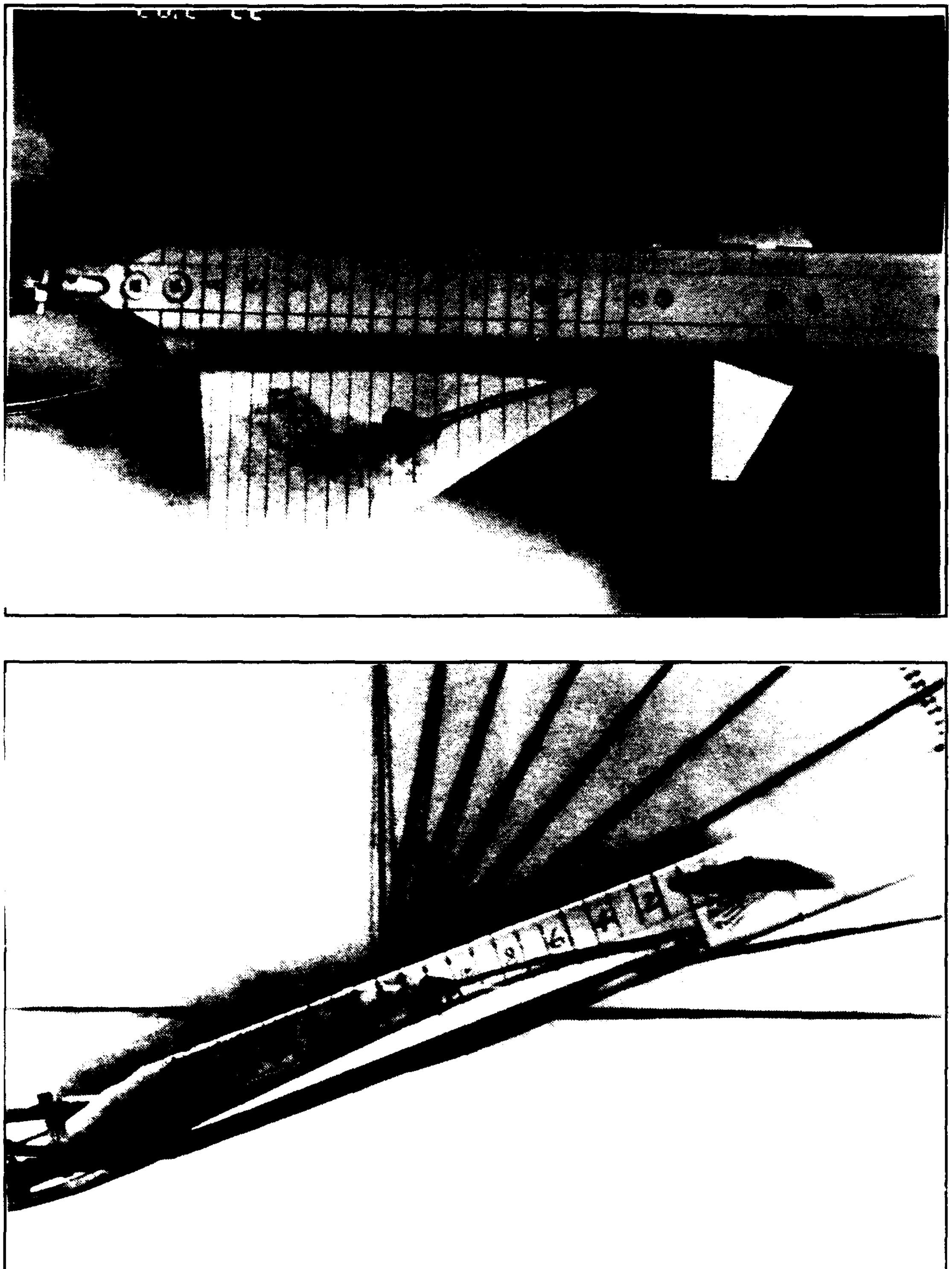

Figure 41. Wing Root Vortex Flow, Static Case, $\alpha=20^0$, $\delta=-25^0$

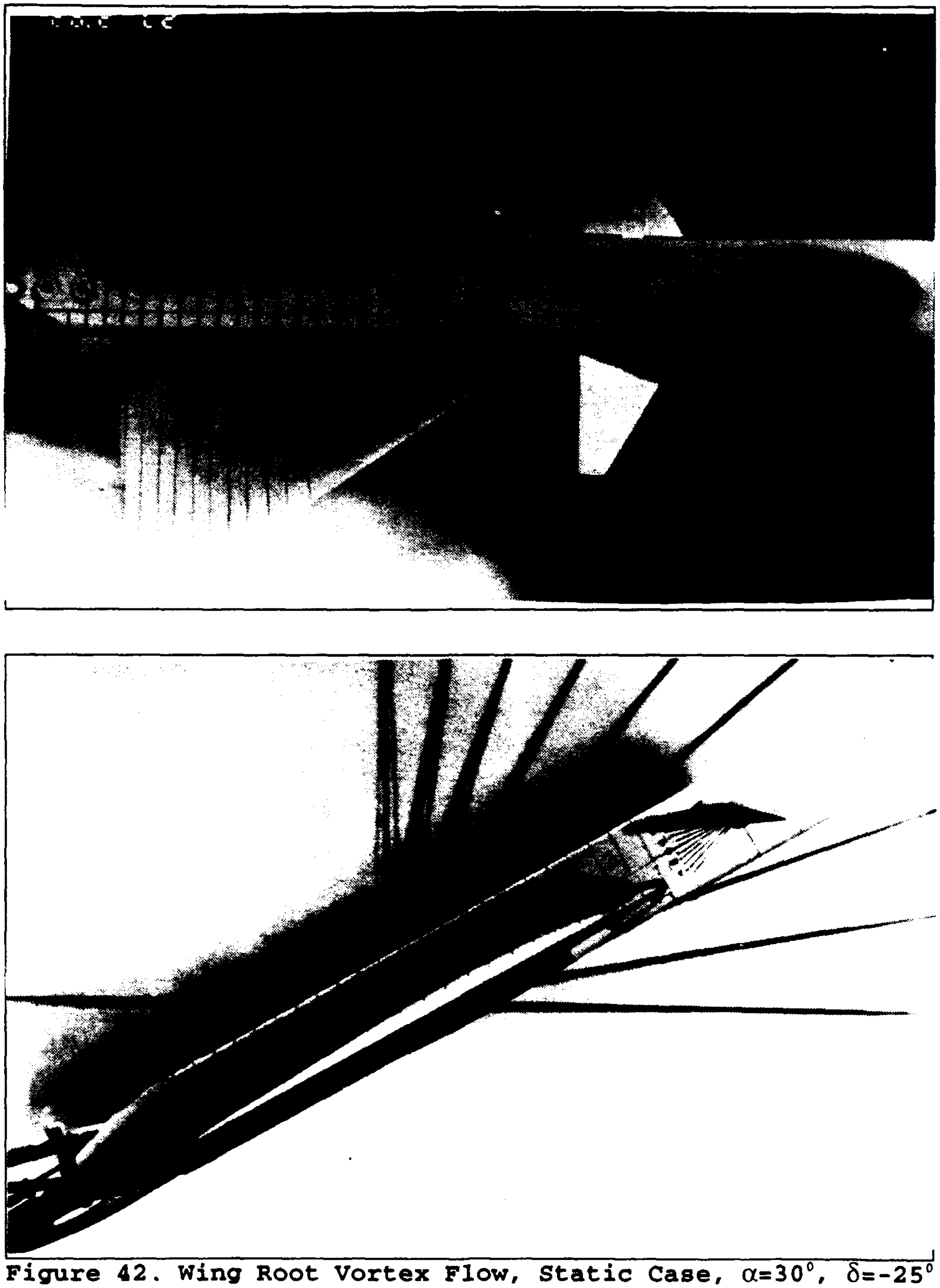

Figure 42. Wing Root Vortex Flow, Static Case, $\alpha=30^{\circ}$, $\delta=-25^{\circ}$

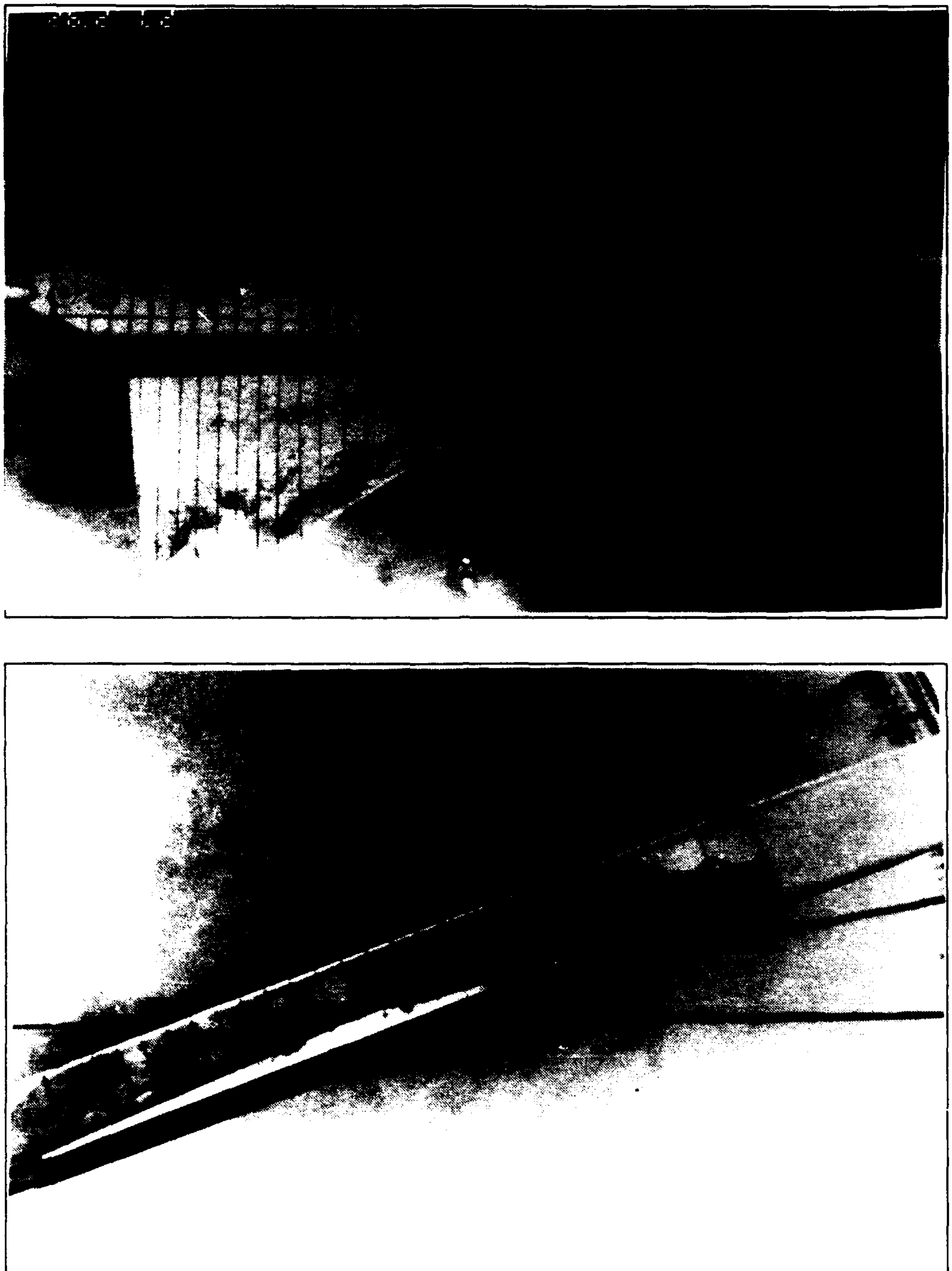

Fihure 43. Wing Root Vortex Flow, α=20°, K=0, δ_a=+/-5°, K_c=1.7

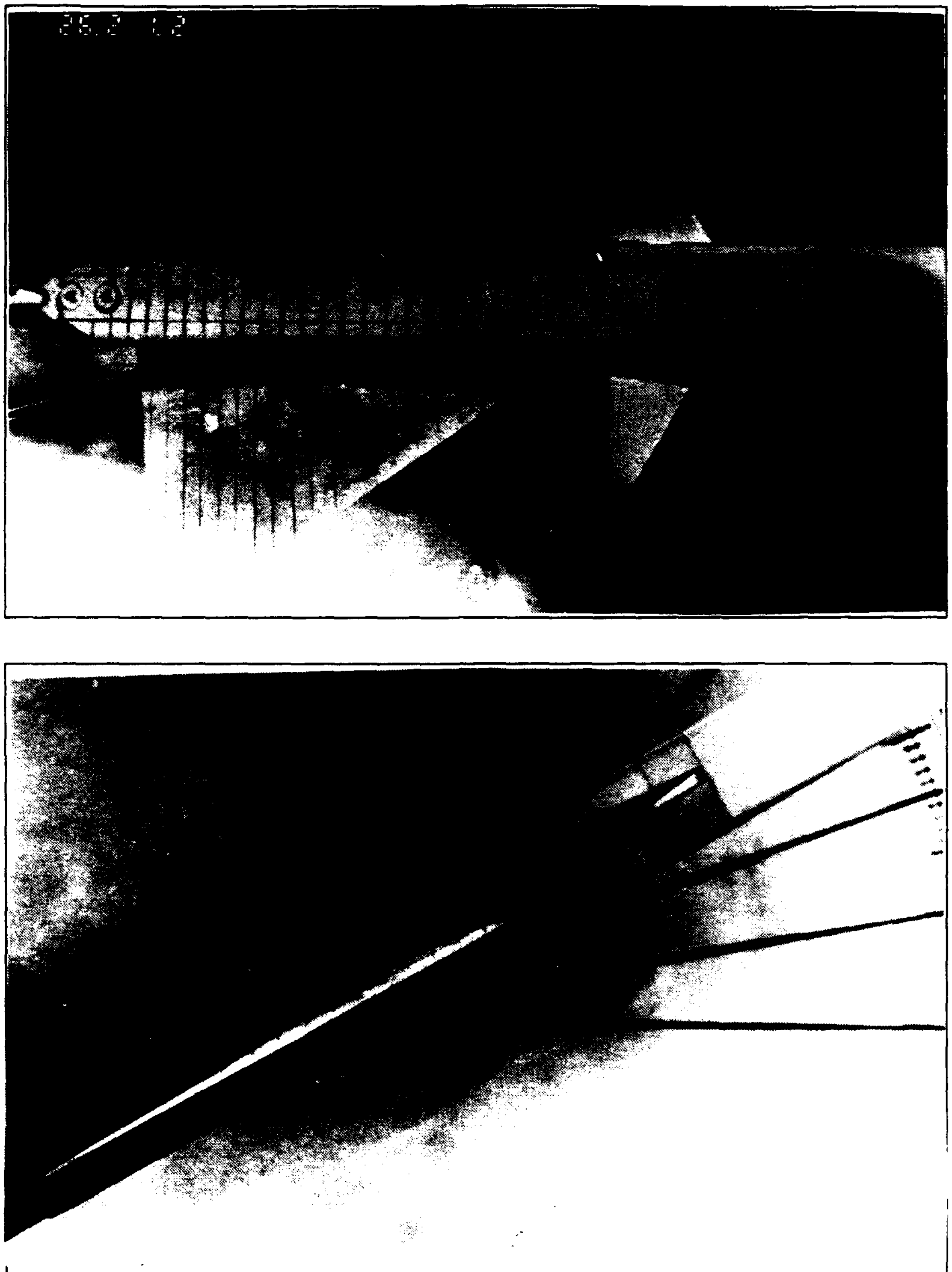

Figure 44. Wing Root Vortex Flow, $\alpha=30^{\circ}$, K=0, $\delta_a=+/-5^{\circ}$, $K_c=1.7$

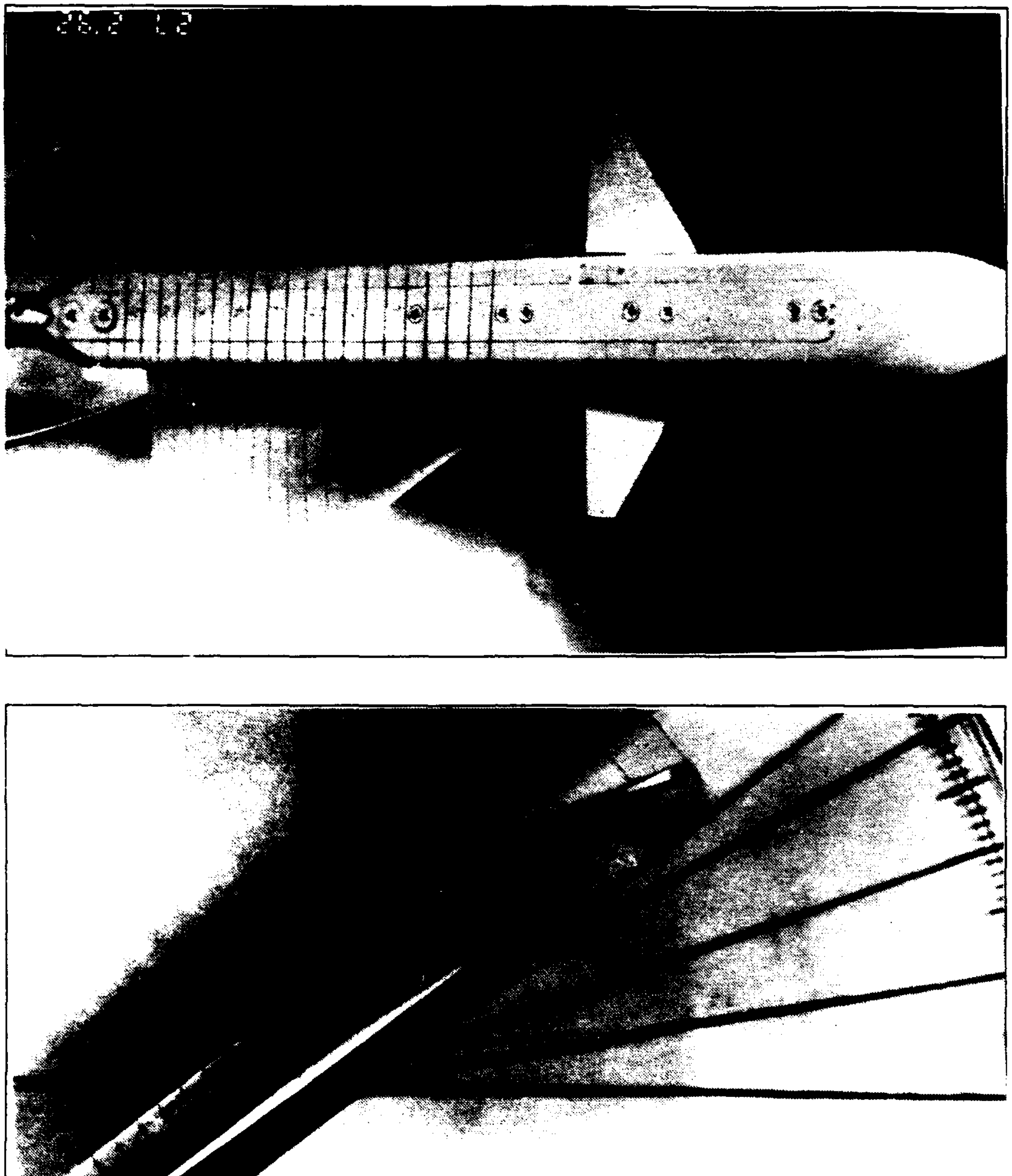

Figure 45. Wing Root Vortex Flow, $\alpha=40^{\circ}$, $K=0$, $\delta_{a}=+/-5^{\circ}$, $K_{c}=1.7$

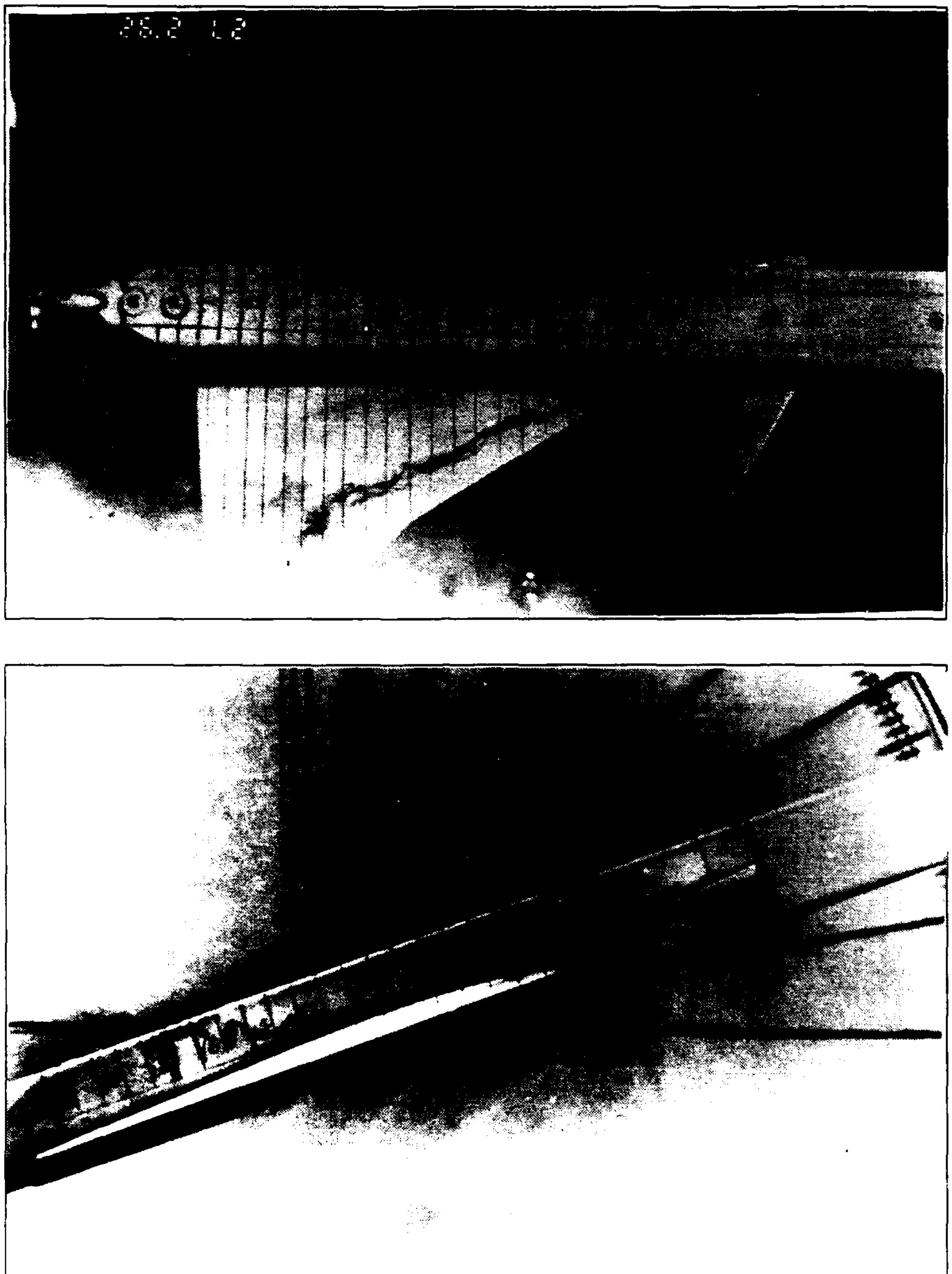

Figure 46. Wing Root Vortex Flow, $\alpha=20^{\circ}$, K=0, $\delta_a=+/-5^{\circ}$, $K_c=10.4$

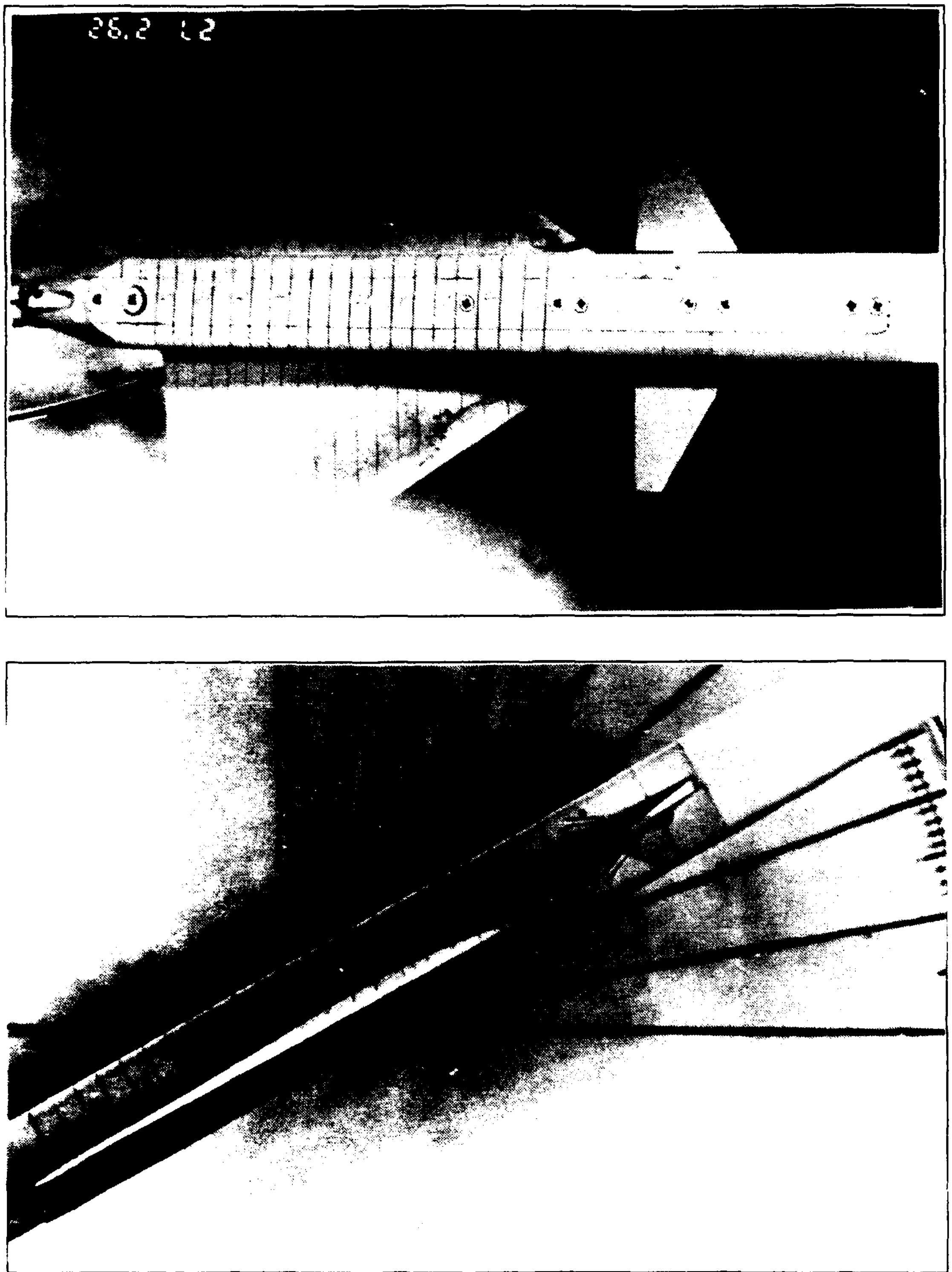

Figure 47. Wing Root Vortex Flow, $\alpha=30^\circ$, $K=0$, $\delta=+/-5^\circ$, $K_c=10.4$

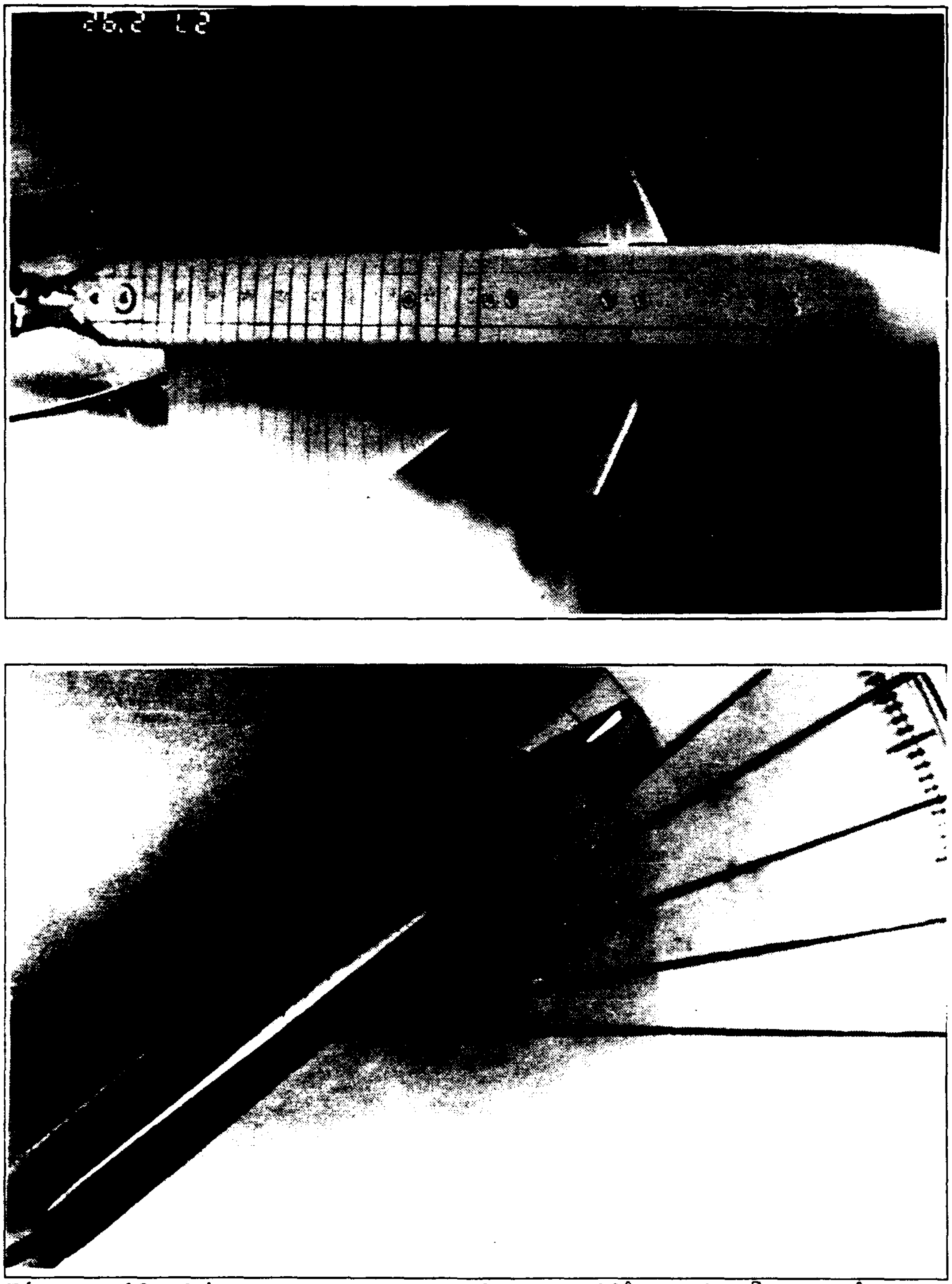

Figure 48. Wing Root Vortex Flow, $\alpha=40^\circ$, $K=0$, $\delta_a=+/-5^\circ$, $K_c=10.4$

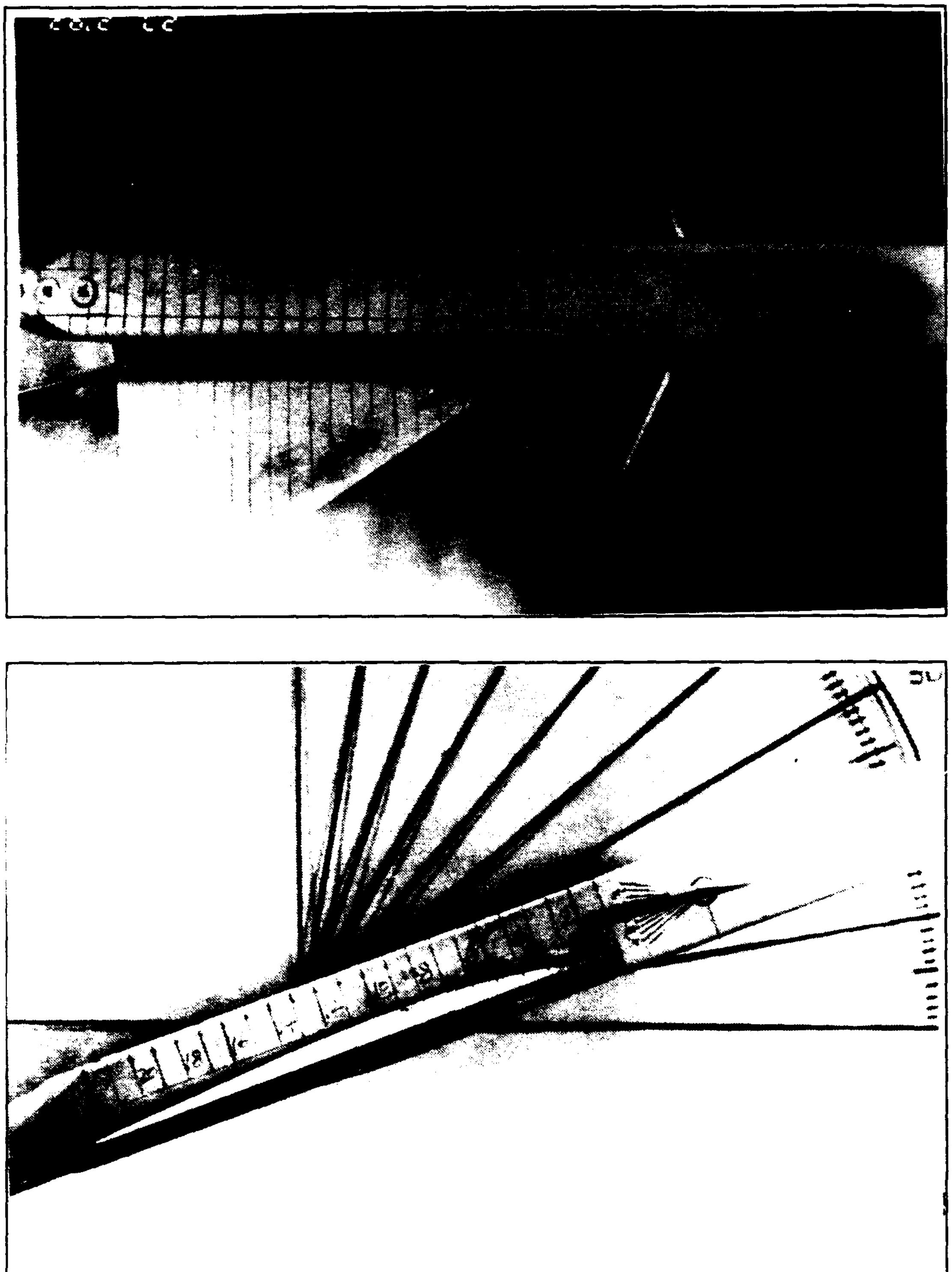

Figure 49. Wing Root Vortex Flow, $\alpha=20^0$, K=0, $\delta=+/-25^0$, $K_C=1.7$

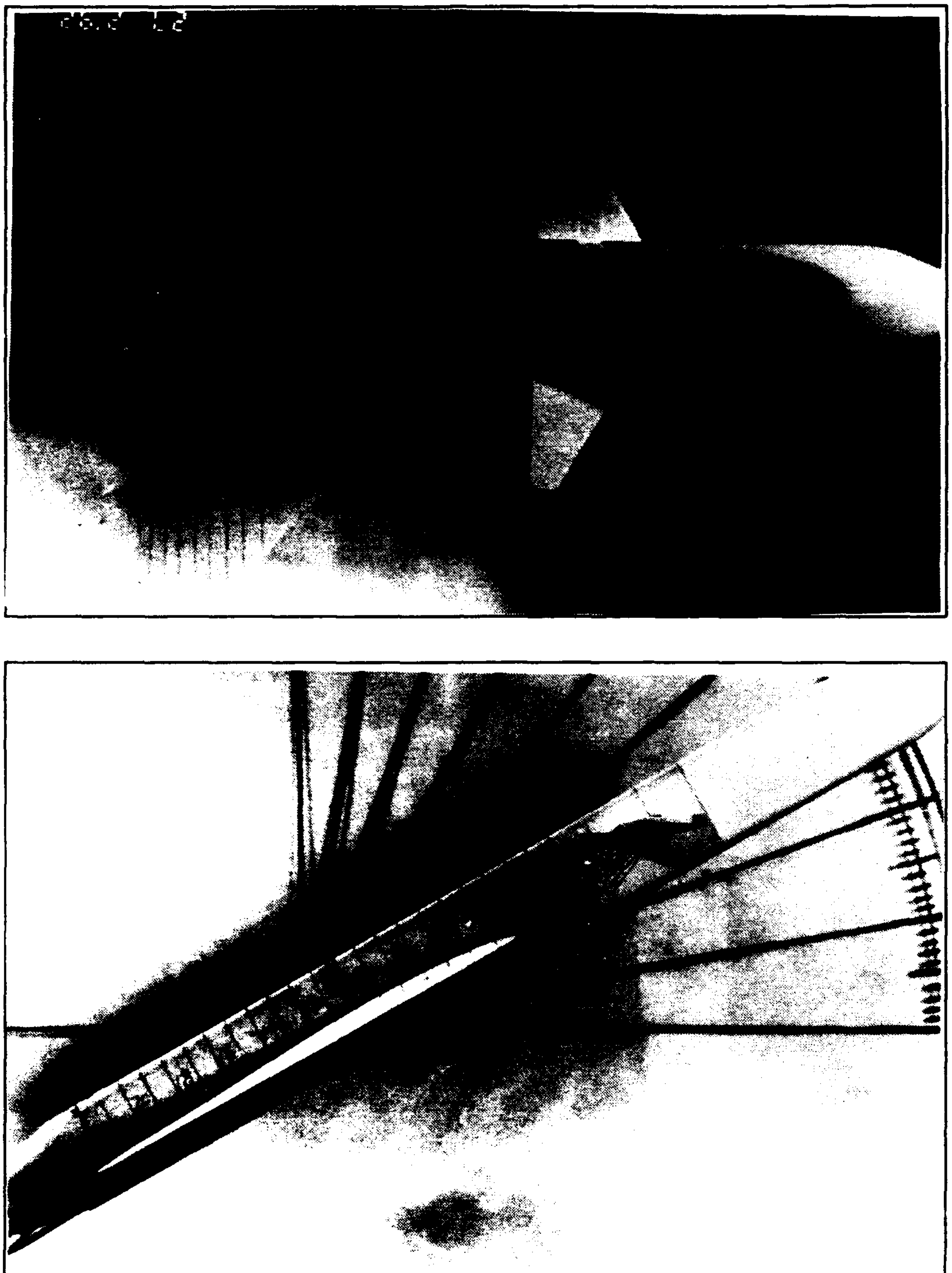

Figure 50. Wing Root Vortex Flow, $\alpha=30^0$, K=0, $\delta_a=+/-25^0$, $K_C=1.7$

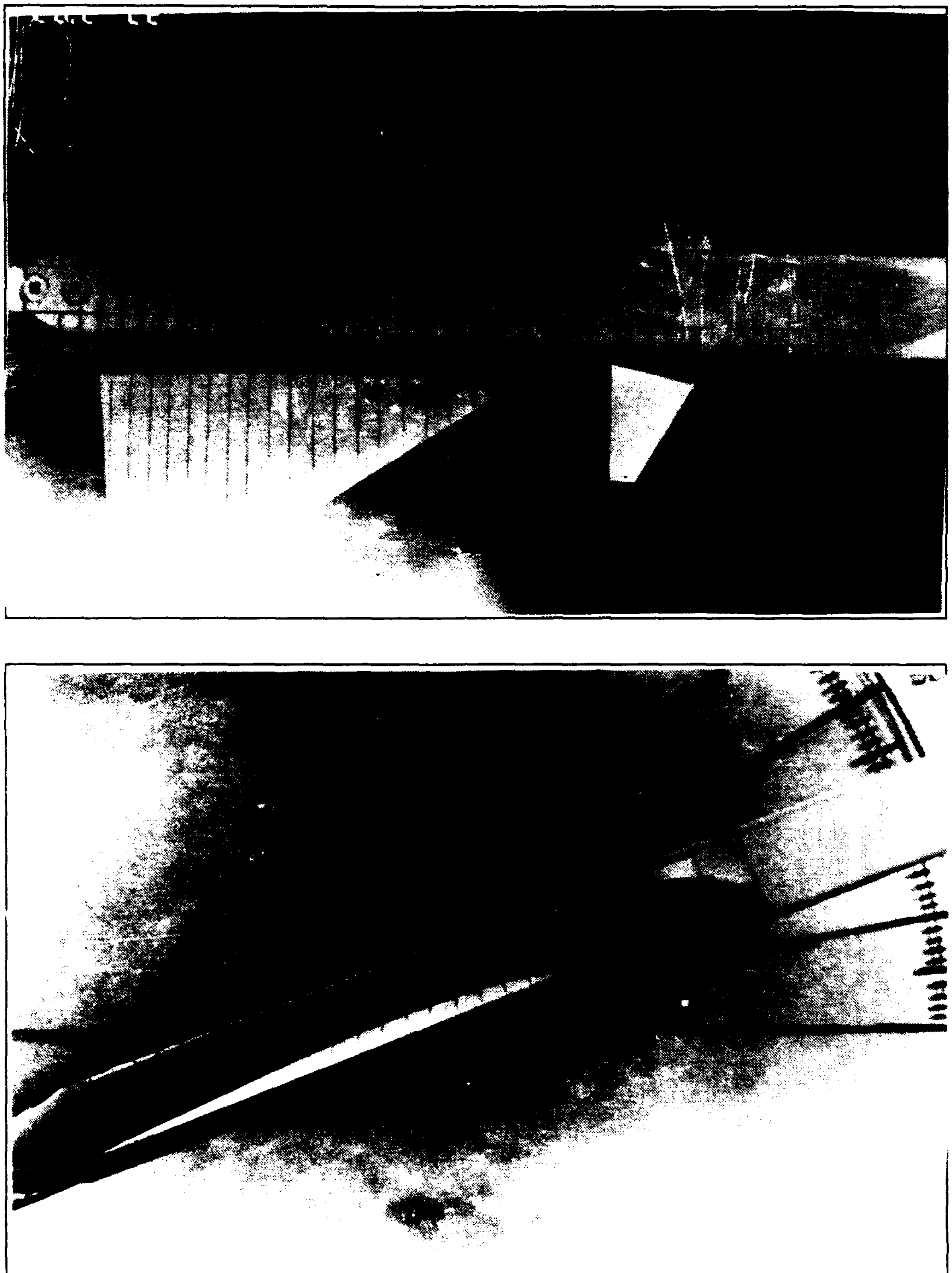

Figure 51. Wing Root Vortex Flow, $\alpha=20°$, $K=0$, $\delta_a=+/-25°$, $K_c=10.4$

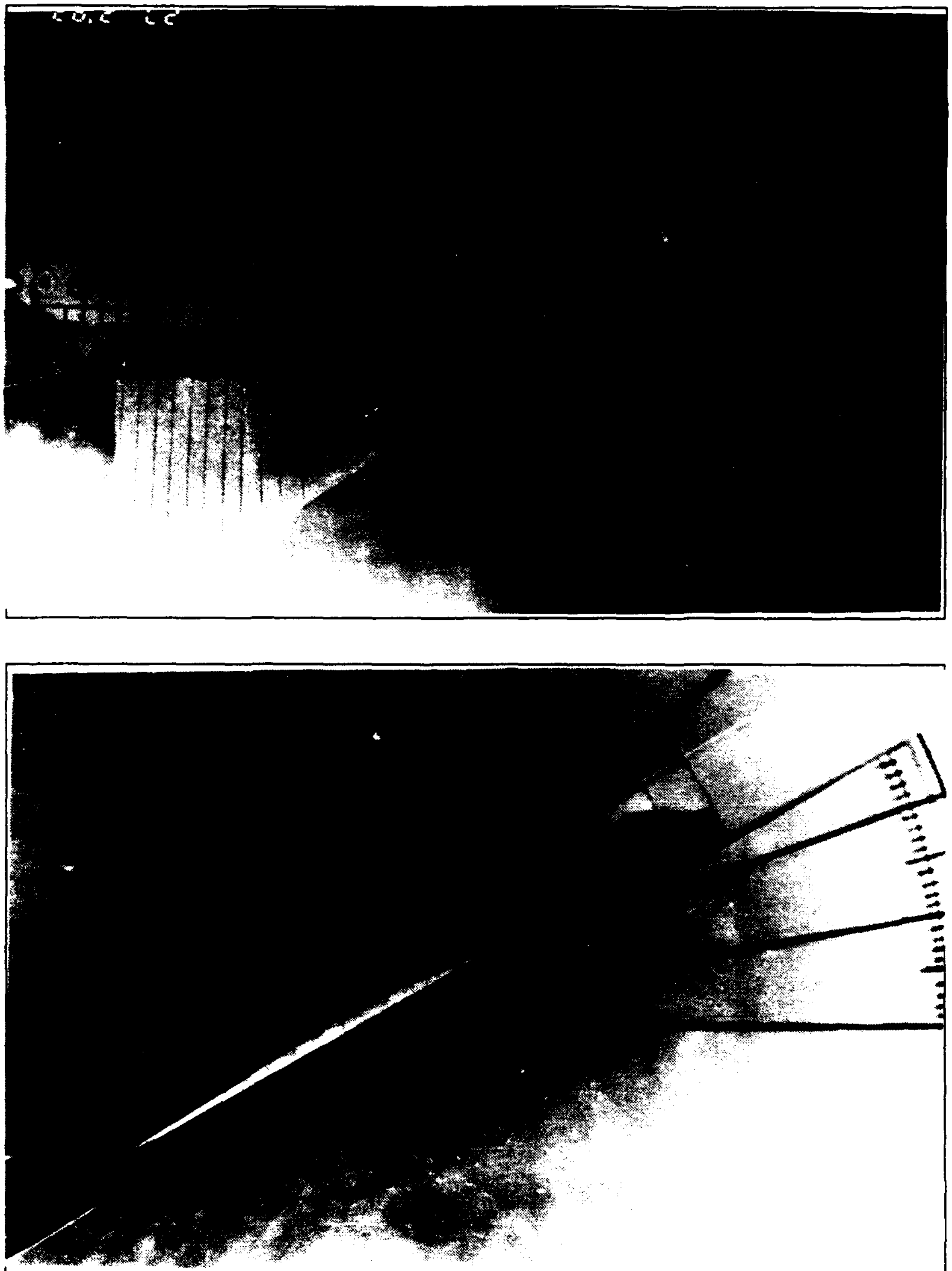

Figure 52. Wing Root Vortex Flow, $\alpha=30^{\circ}$, $K=0$, $\delta_a=+/-25^{\circ}$, $K_c=10.4$

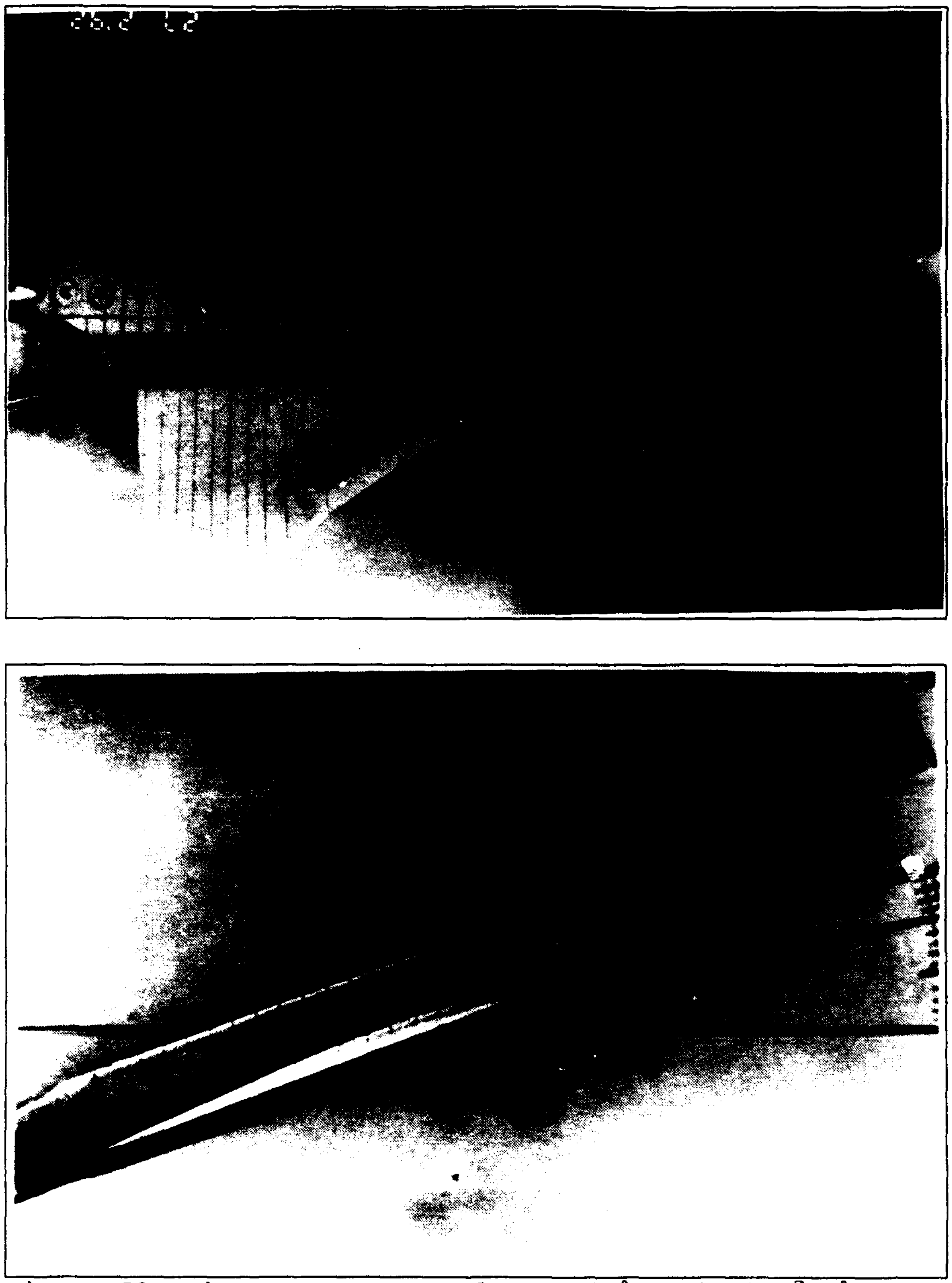

Figure 53. Wing Root Vortex Flow, $\alpha=20^{\circ}$, $K=0.08$, $\delta=0^{\circ}$, $K_c=0$

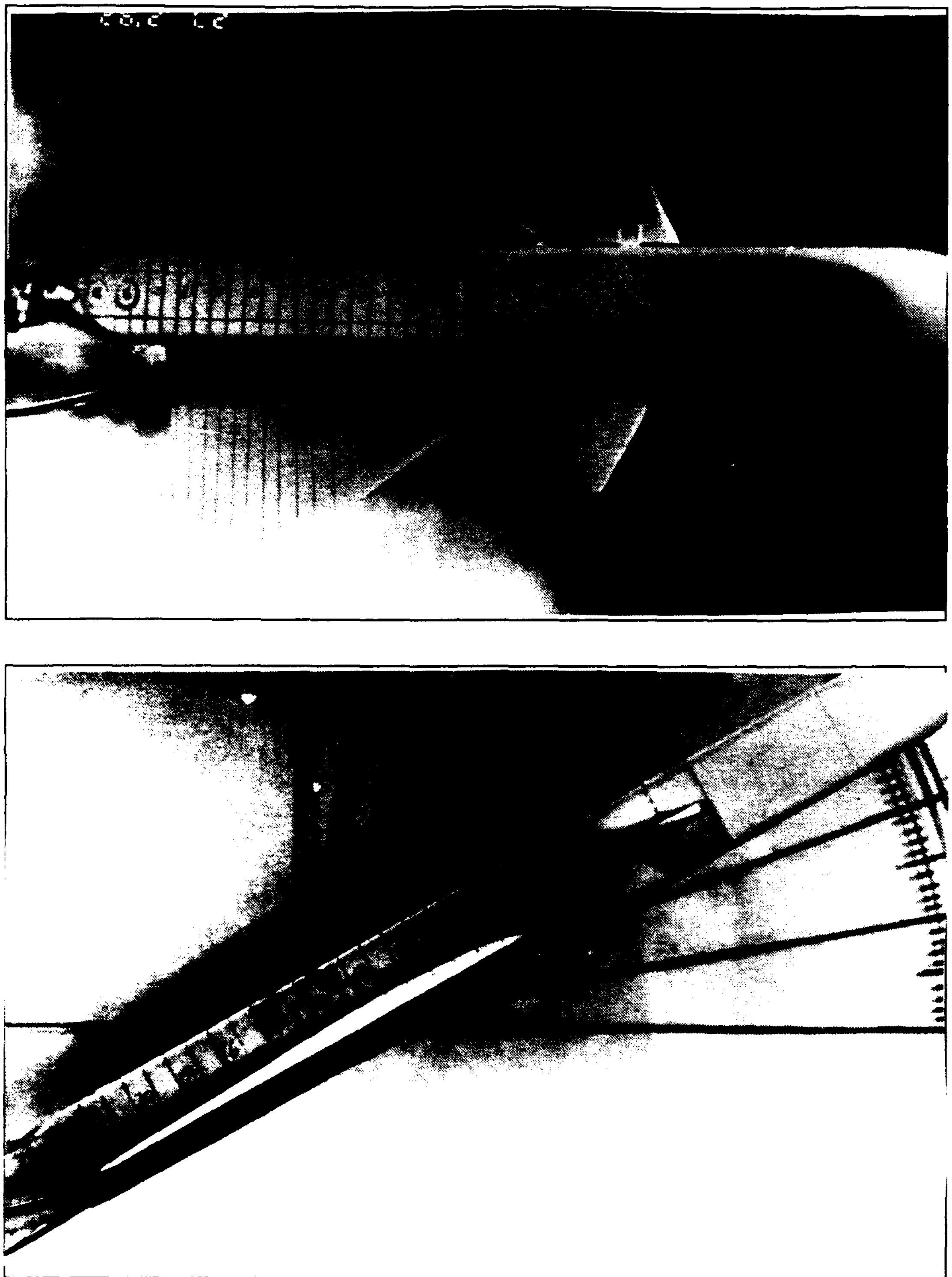

Figure 54. Wing Root Vortex Flow, α=30°, K=0.08, δ=0°, K_c=0

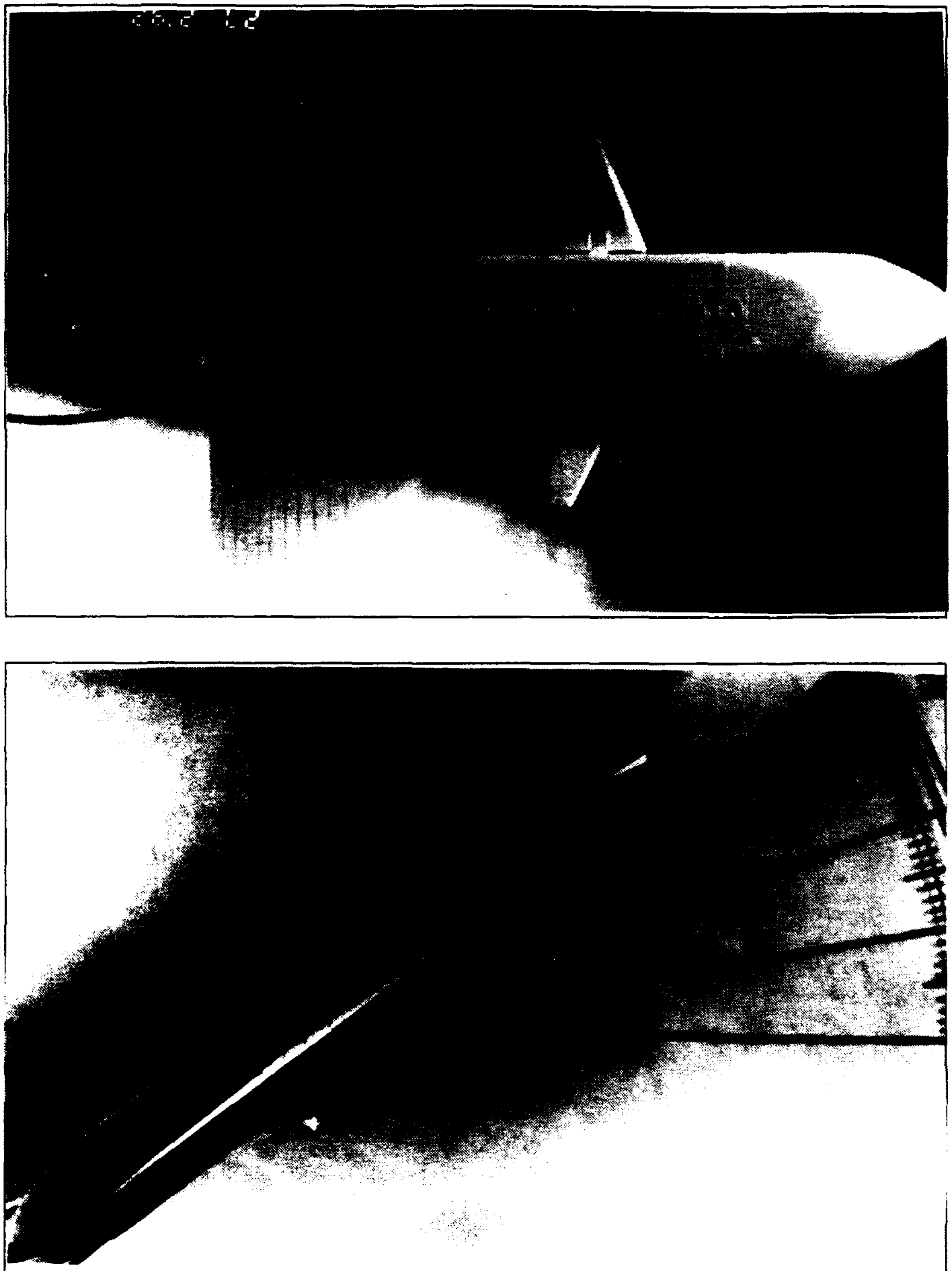

Figure 55. Wing Root Vortex Flow, $\alpha=40^{\circ}$, $K=0.08$, $\delta=0^{\circ}$, $K_c=0$

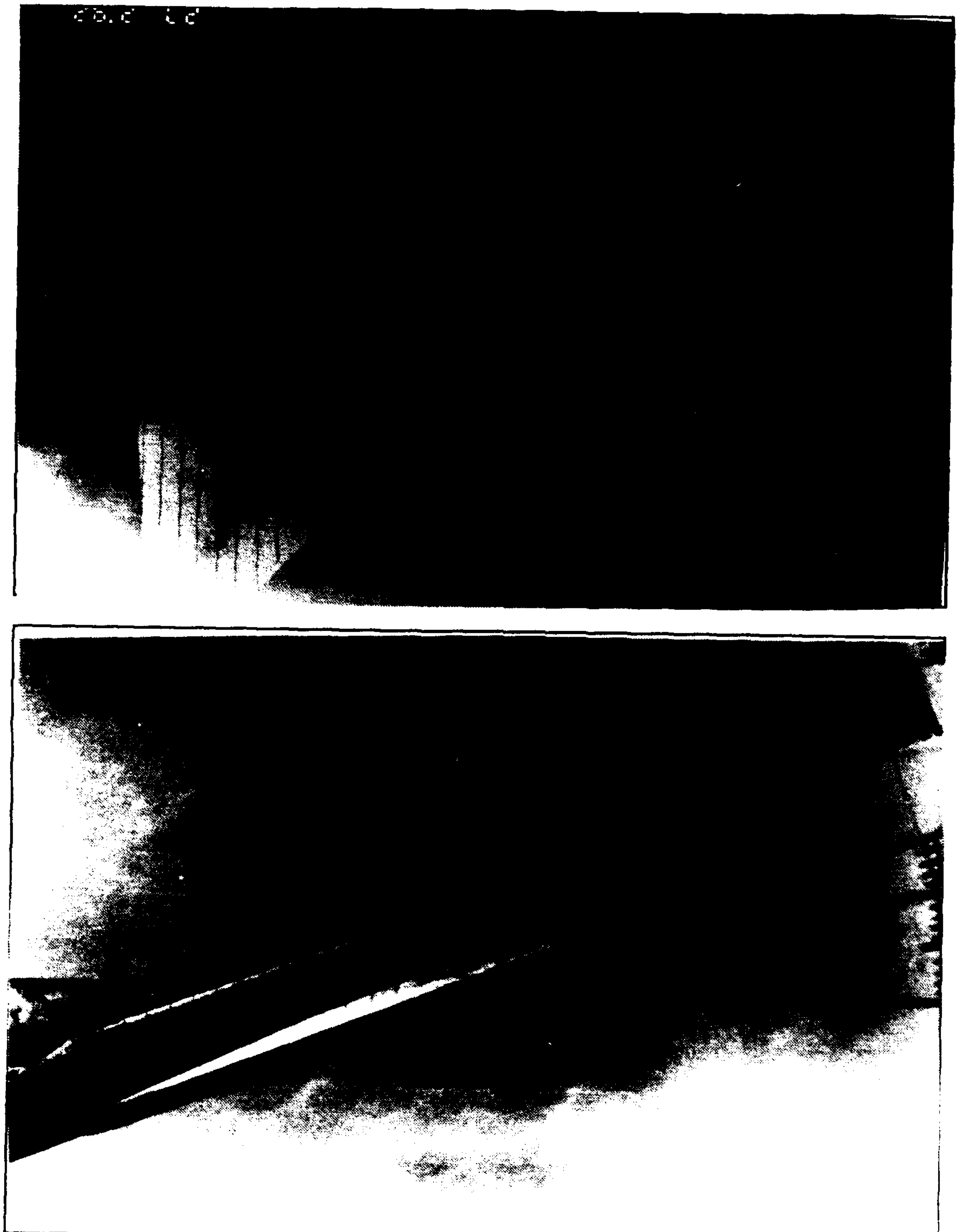

Figure 56. Wing Root Vortex Flow, $\alpha=20^0$, $K=0.16$, $\delta=0^0$, $K_C=0$

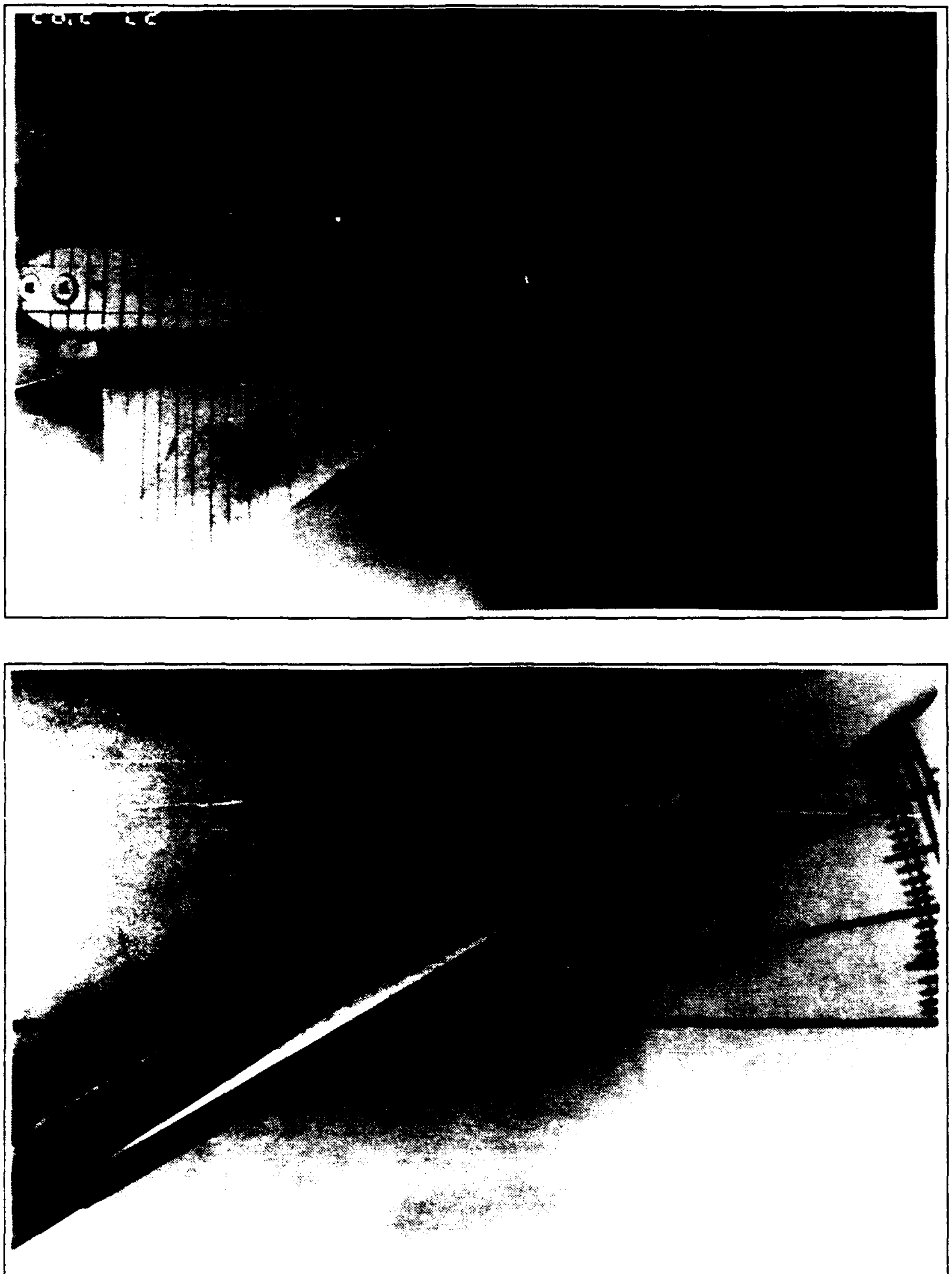

Figure 57. Wing Root Vortex Flow, $\alpha=30^{\circ}$, $K=0.16$, $\delta=0^{\circ}$, $K_c=0$

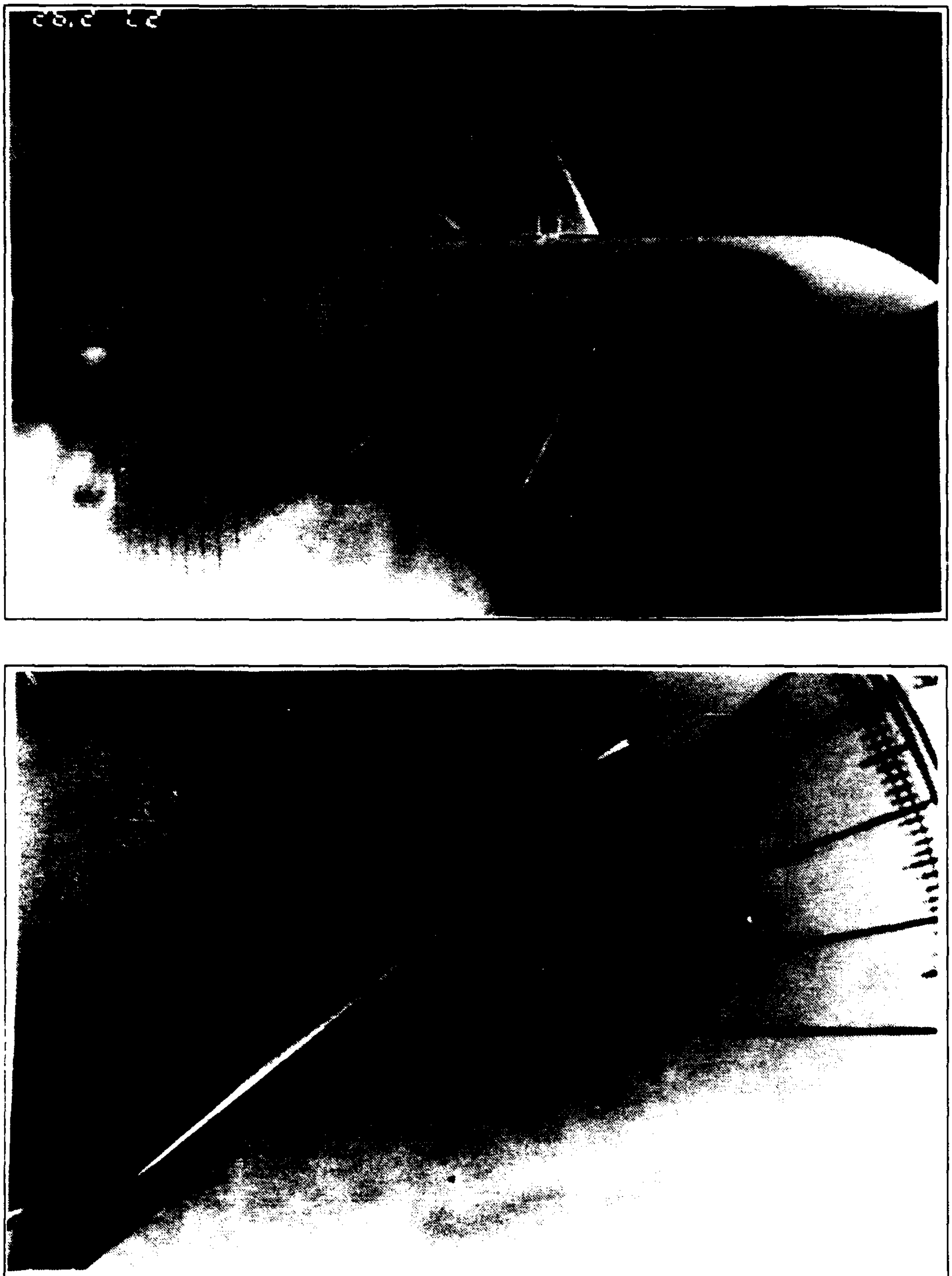

Figure 58. Wing Root Vortex Flow, $\alpha=40^{\circ}$, $K=0.16$, $\delta=0^{\circ}$, $K_c=0$

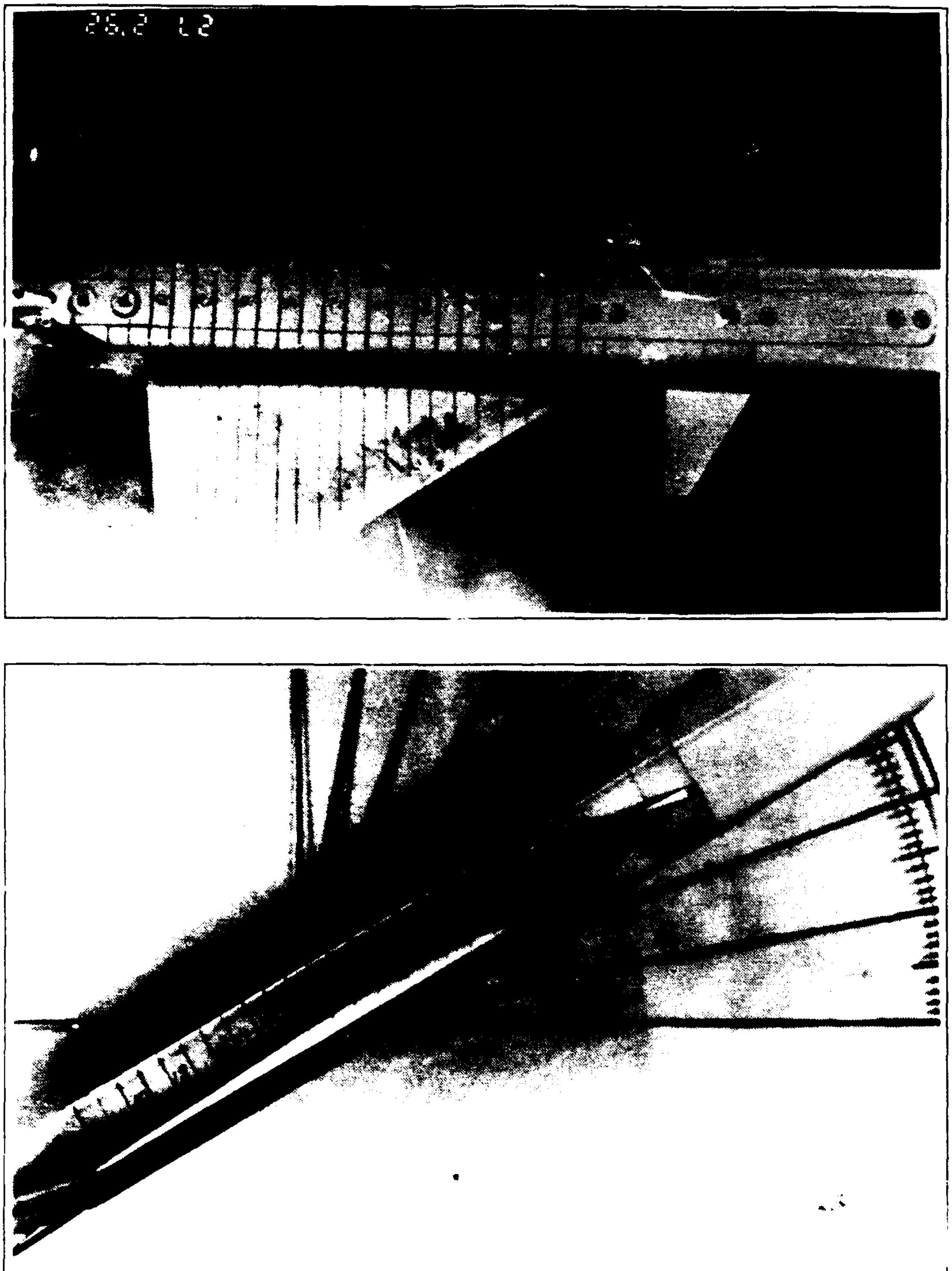

Figure 59. Wing Root Vortex Flow, $\alpha=30^\circ$, $K=-0.08$, $\delta=0^\circ$, $K_c=0$

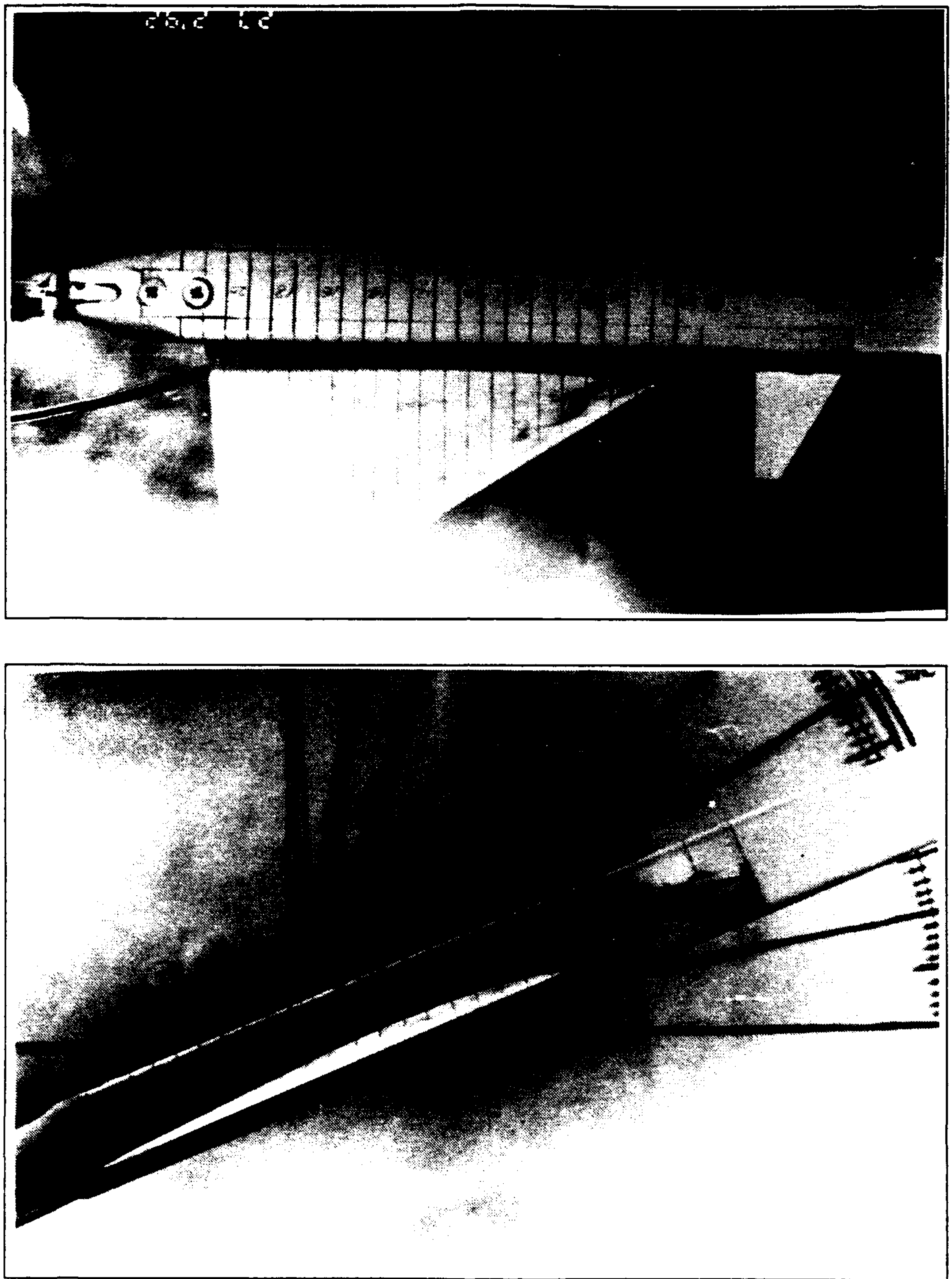

Figure 60. Wing Root Vortex Flow, $\alpha=20^{\circ}$, $K=-0.08$, $\delta=0^{\circ}$, $K_c=0$

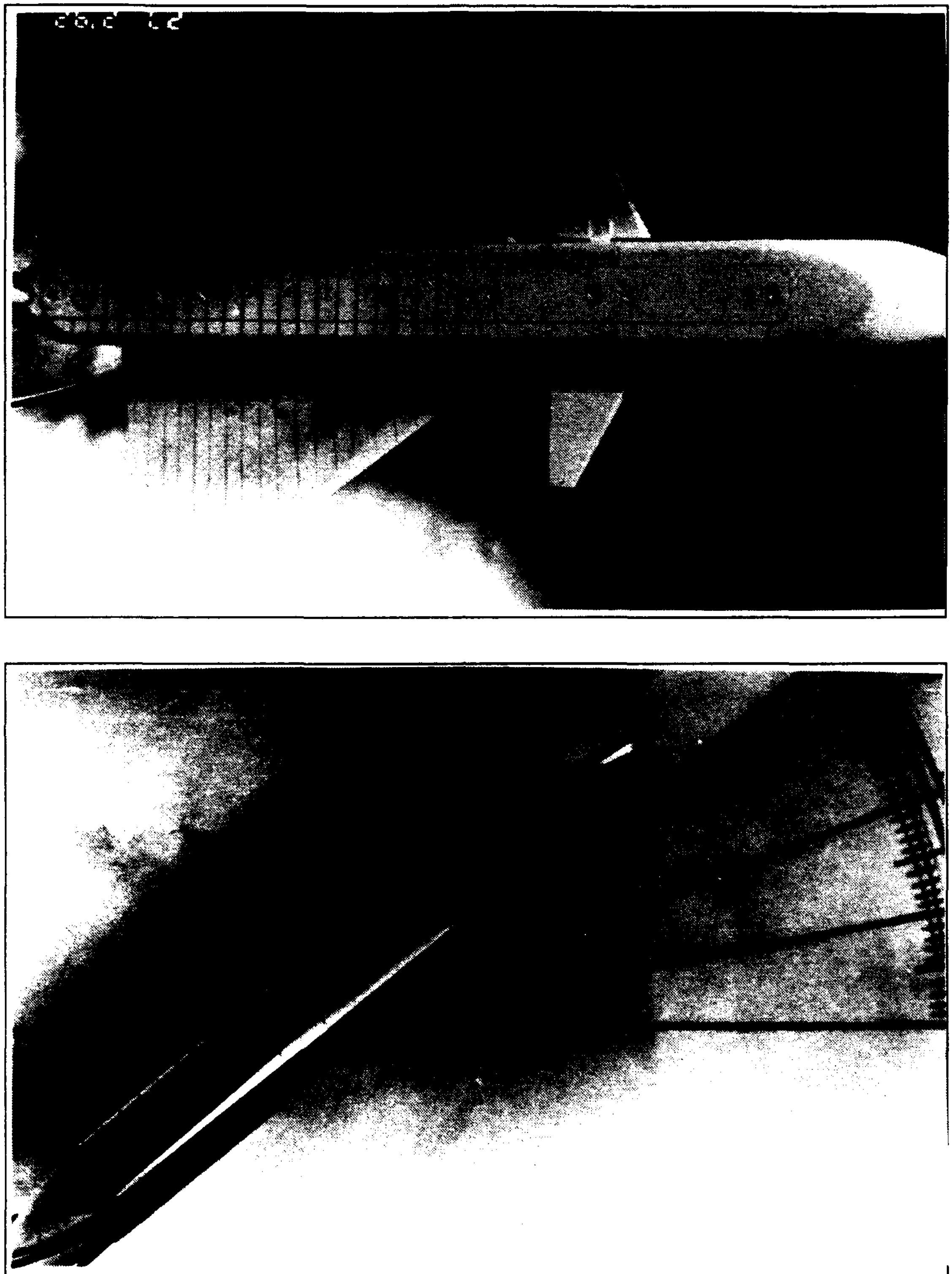

Figure 61. Wing Root Vortex Flow, $\alpha=40^{\circ}$, $K=-0.16$, $\delta=0^{\circ}$, $K_c=0$

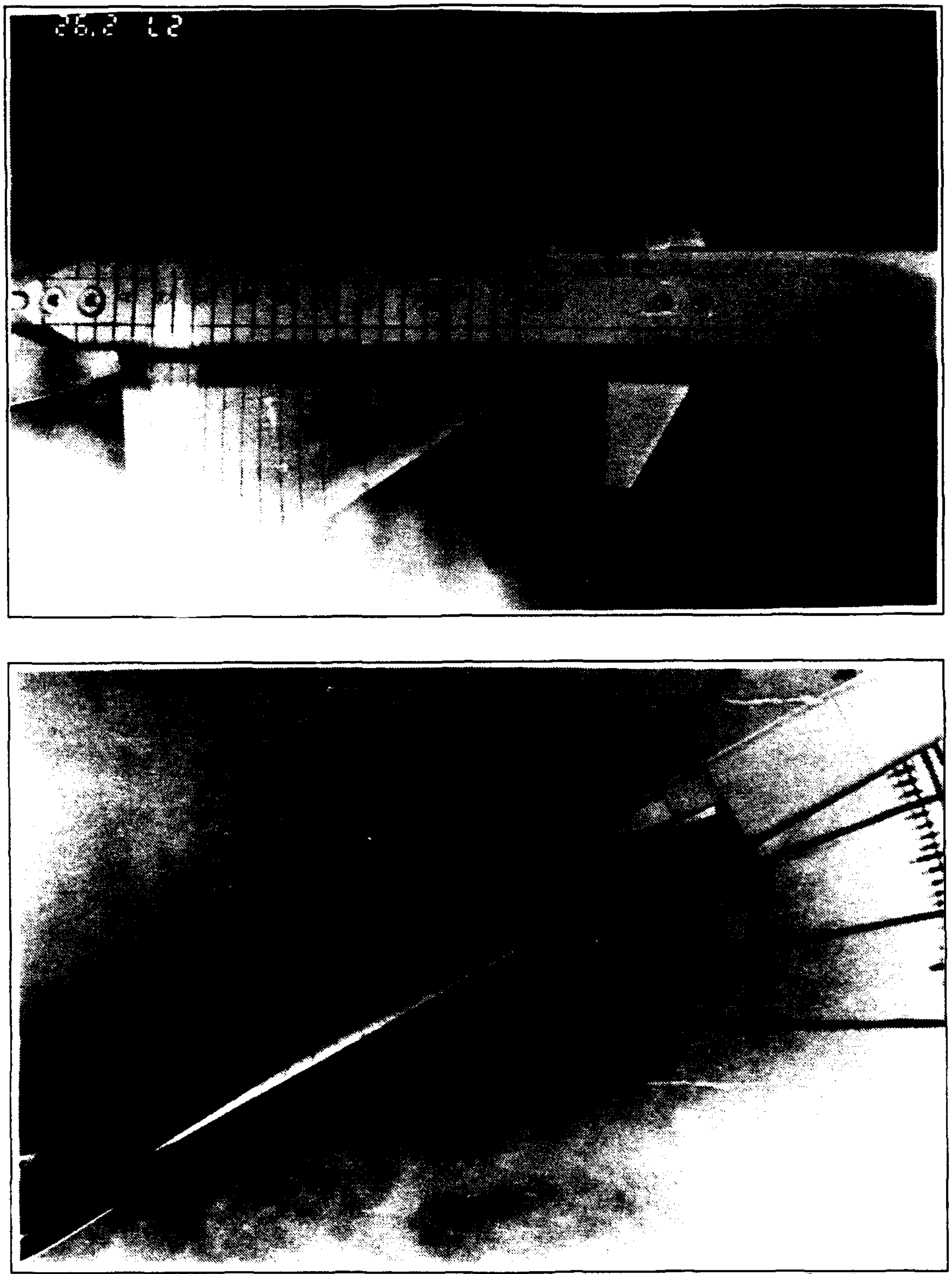

Figure 62. Wing Root Vortex Flow, $\alpha=30^\circ$, $K=-0.16$, $\delta=0^\circ$, $K_c=0$

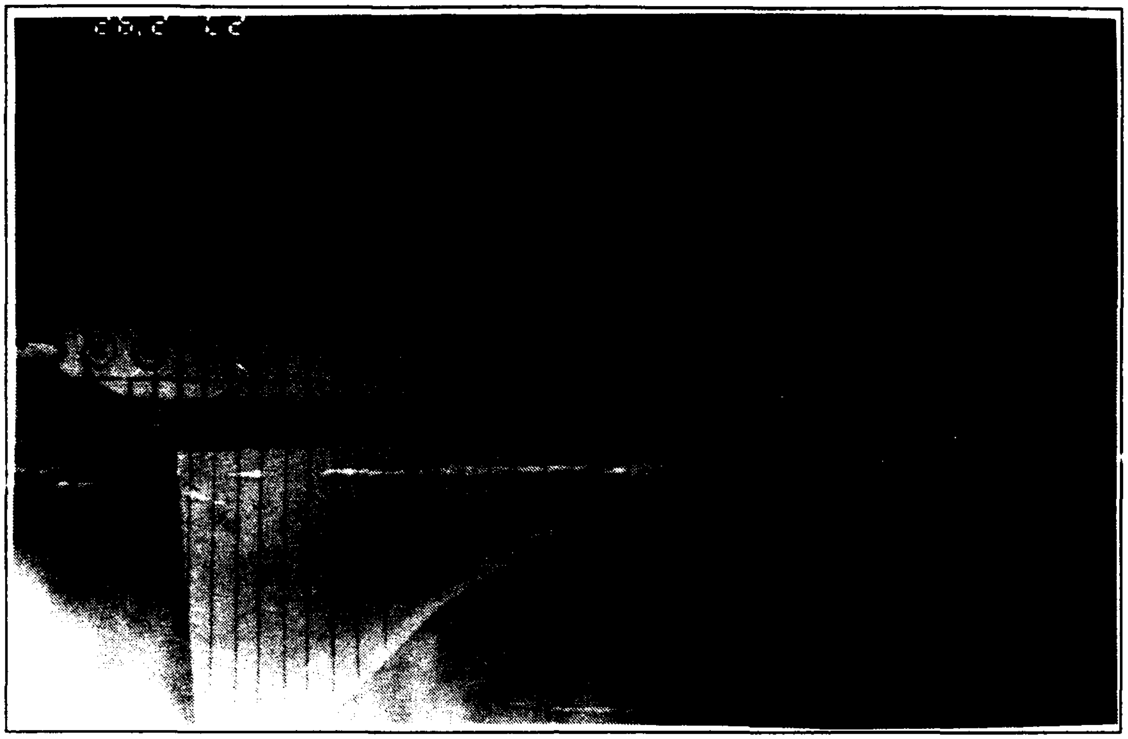

Figure 63. Wing Root Vortex Flow, $\alpha=20^{\circ}$, K=-0.16, $\delta=0^{\circ}$, $K_c=0$

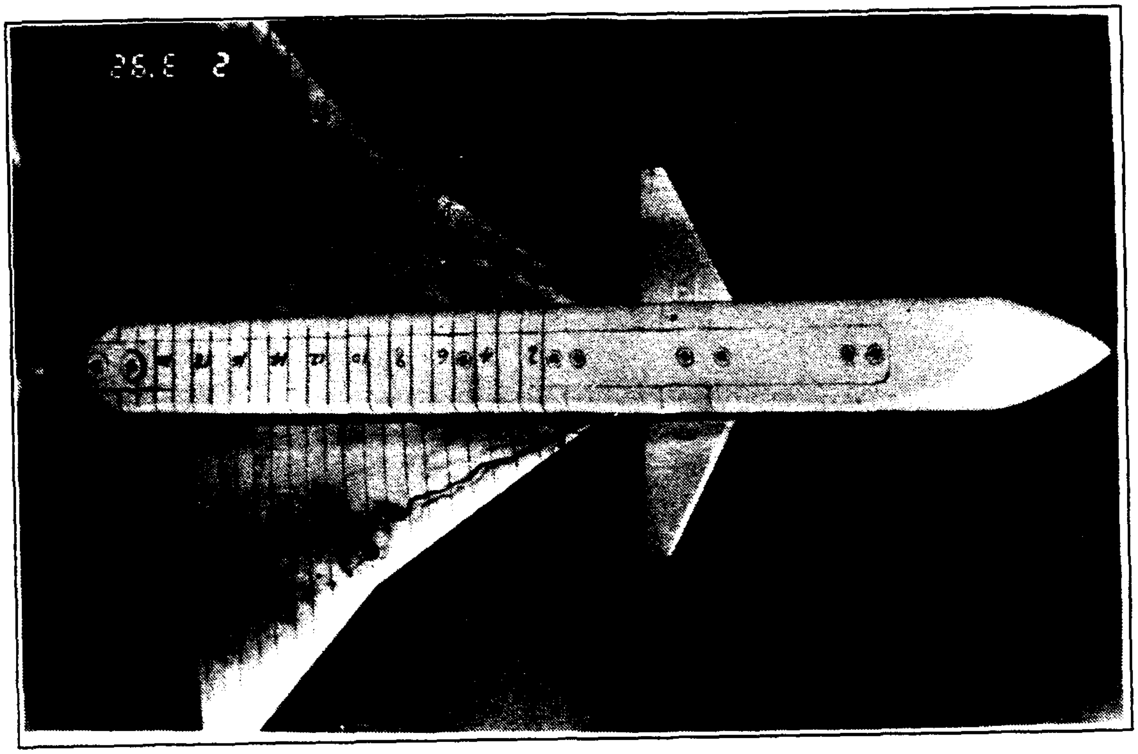

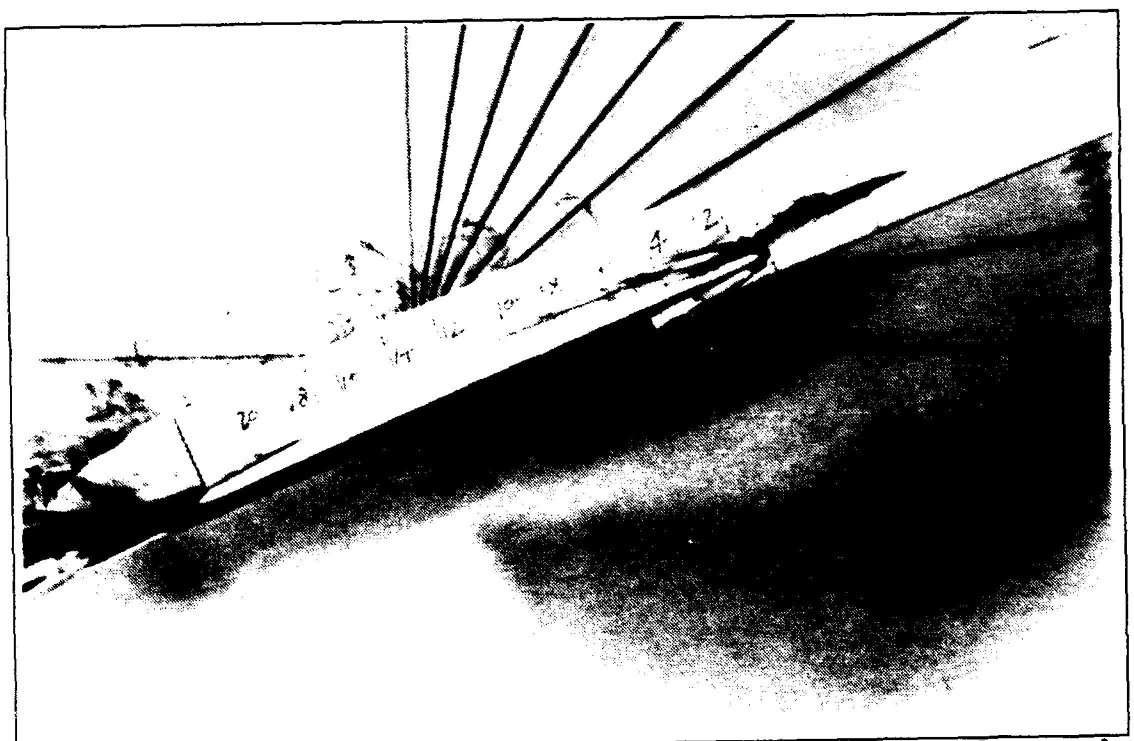

Figure 64. Wing Root Vortex Flow, α=20°, K=0.08, δ_a=+/-5°, K_c=1.7

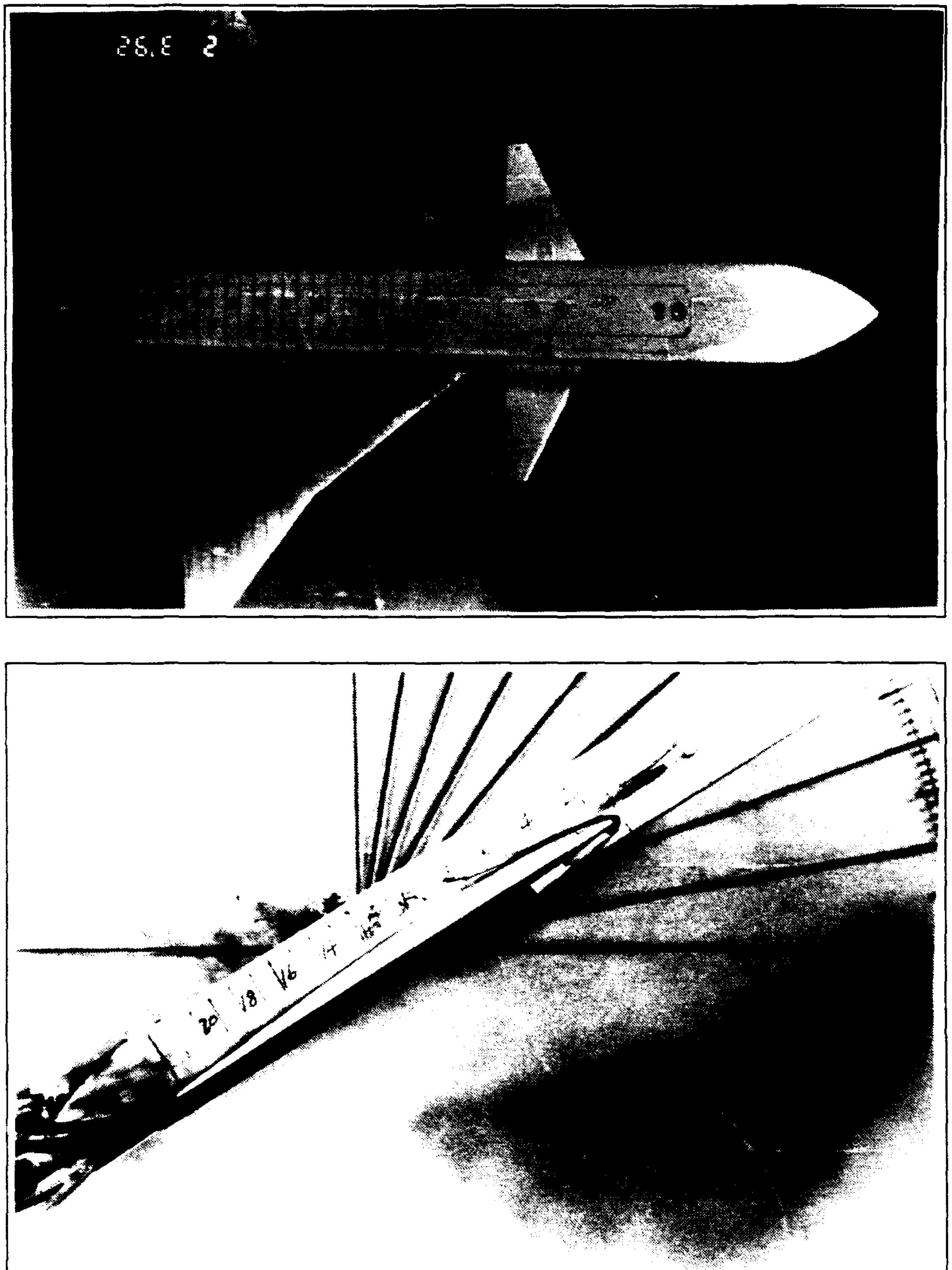

Figure 65. Wing Root Vortex Flow, $\alpha=30^\circ$, $K=0.08$, $\delta_a=+/-5^\circ$, $K_c=1.7$

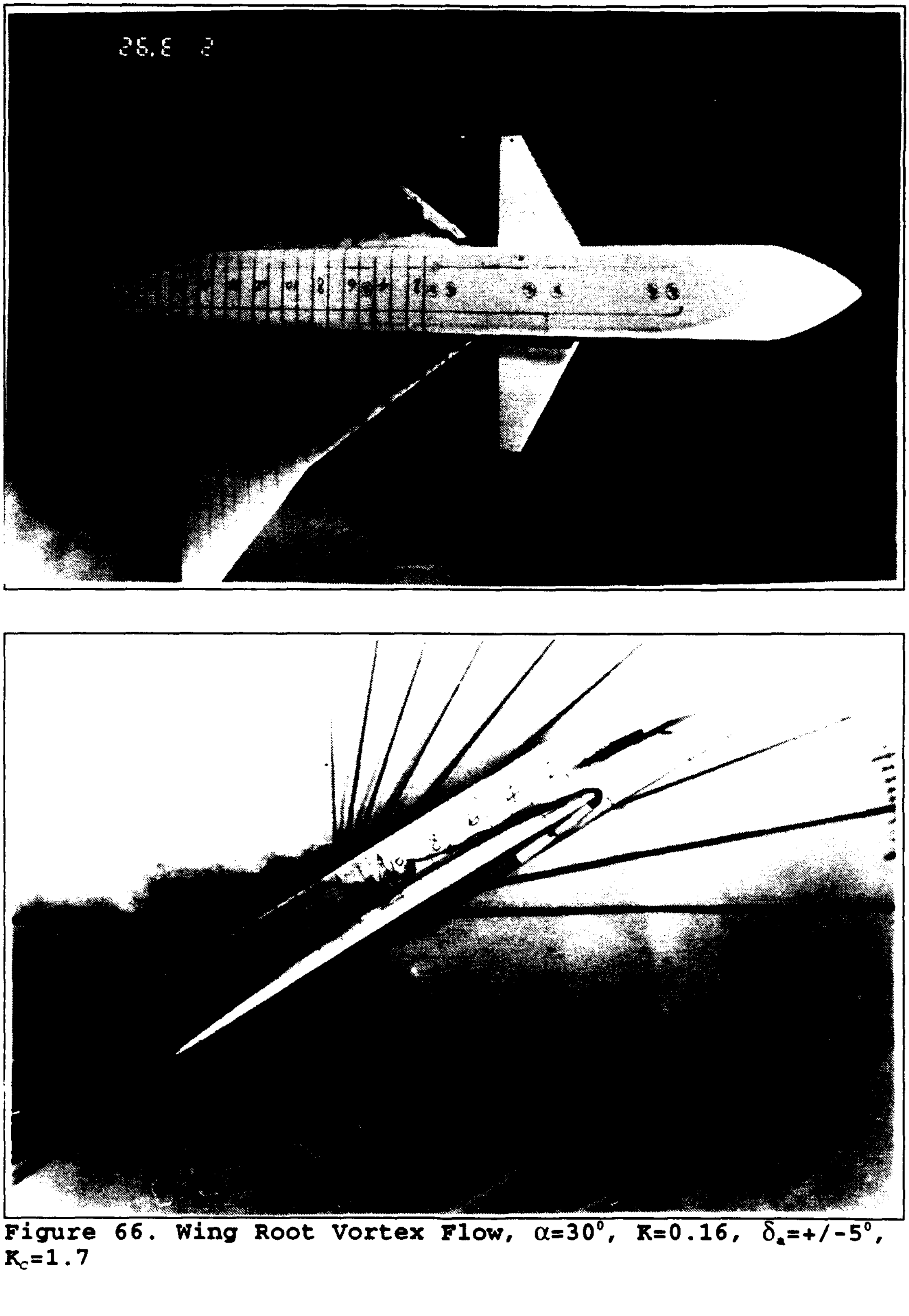

Figure 66. Wing Root Vortex Flow, $\alpha=30^\circ$, $K=0.16$, $\delta_a=+/-5^\circ$, $K_c=1.7$

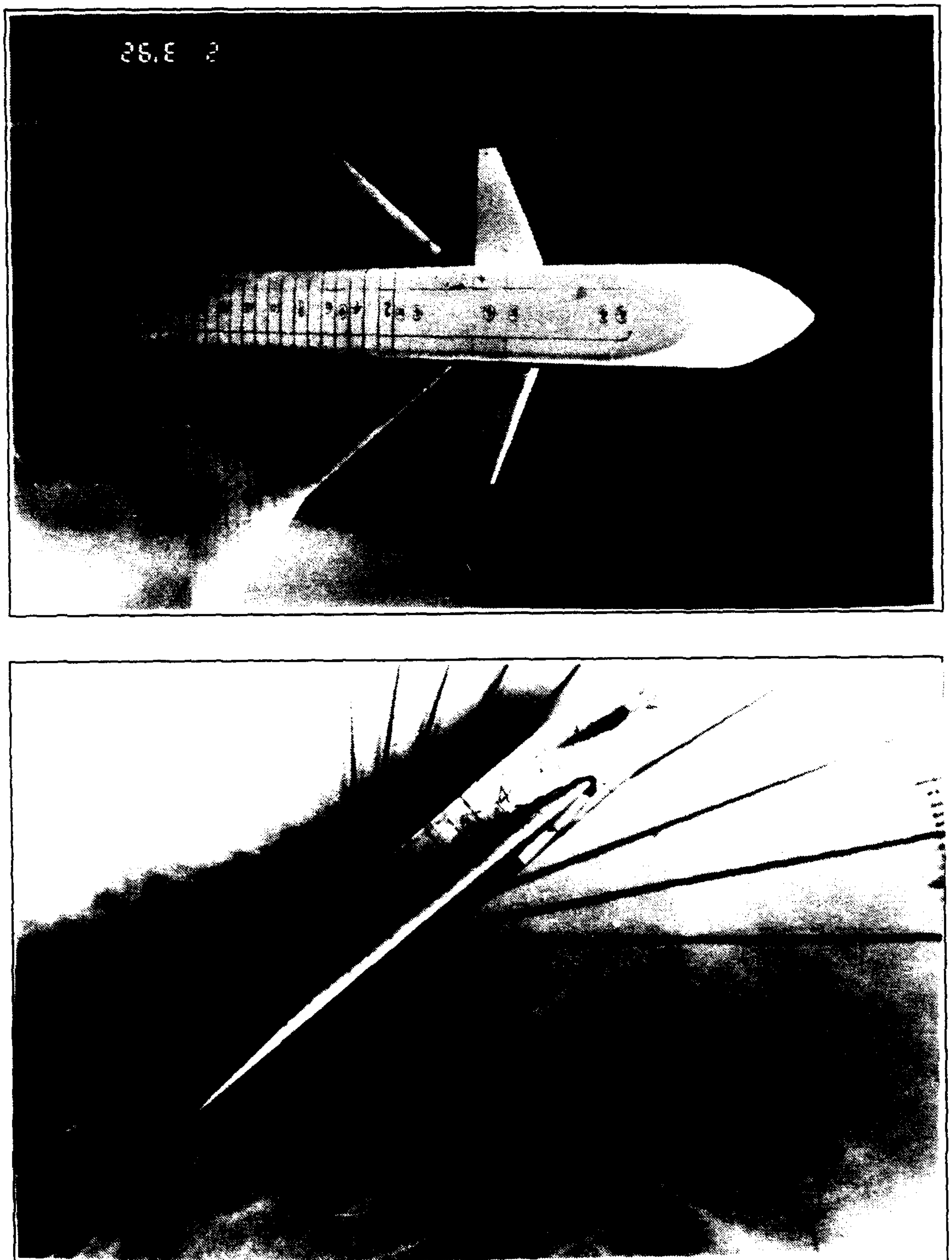

Figure 67. Wing Root Vortex Flow, $\alpha=40^{\circ}$, K=0.16, $\delta=+/-5^{\circ}$, $K_c=1.7$

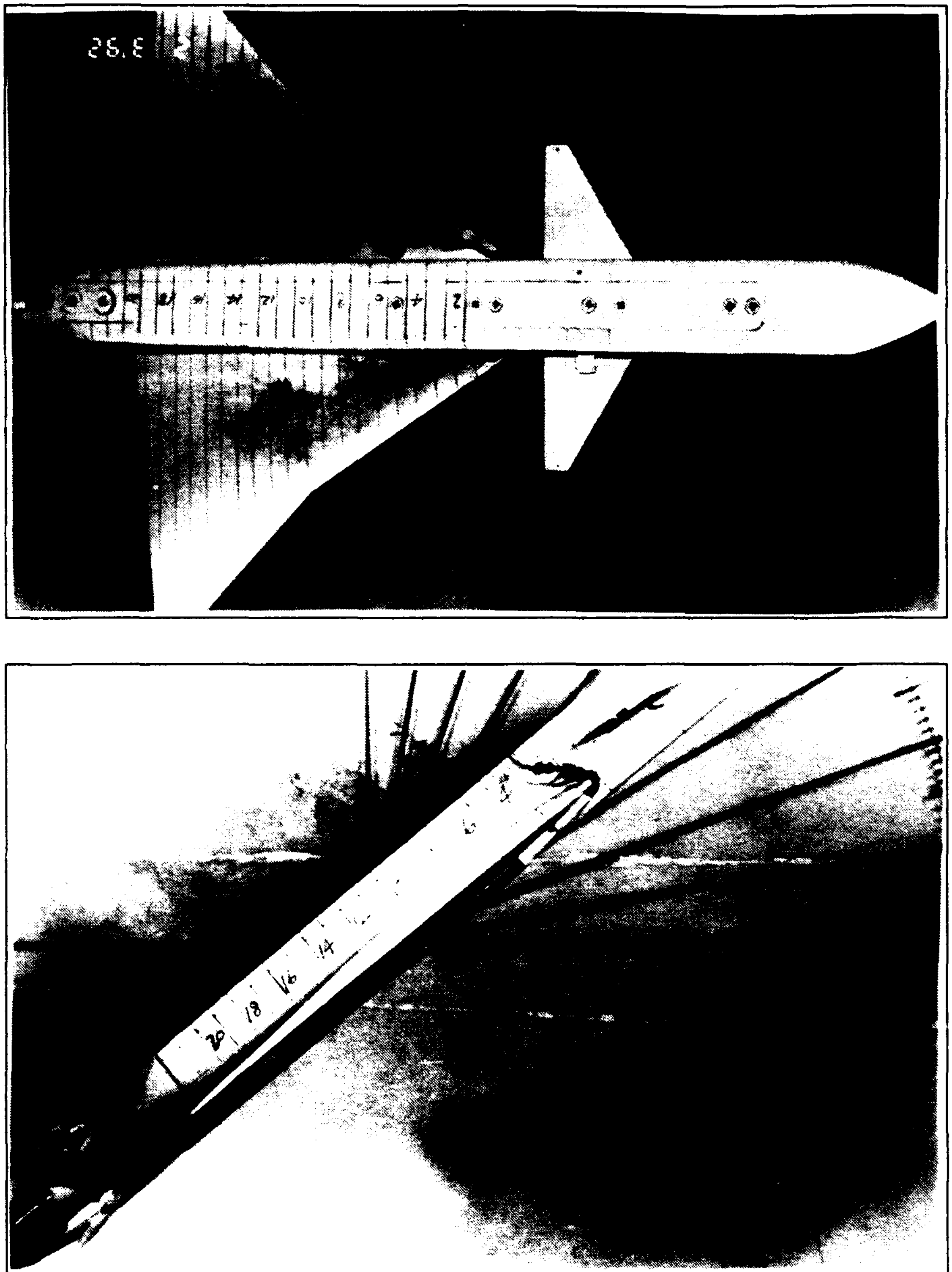

Figure 68. Wing Root Vortex Flow, $\alpha=40^{\circ}$, $K=-0.08$, $\delta_a=+/-5^{\circ}$, $K_c=1.7$

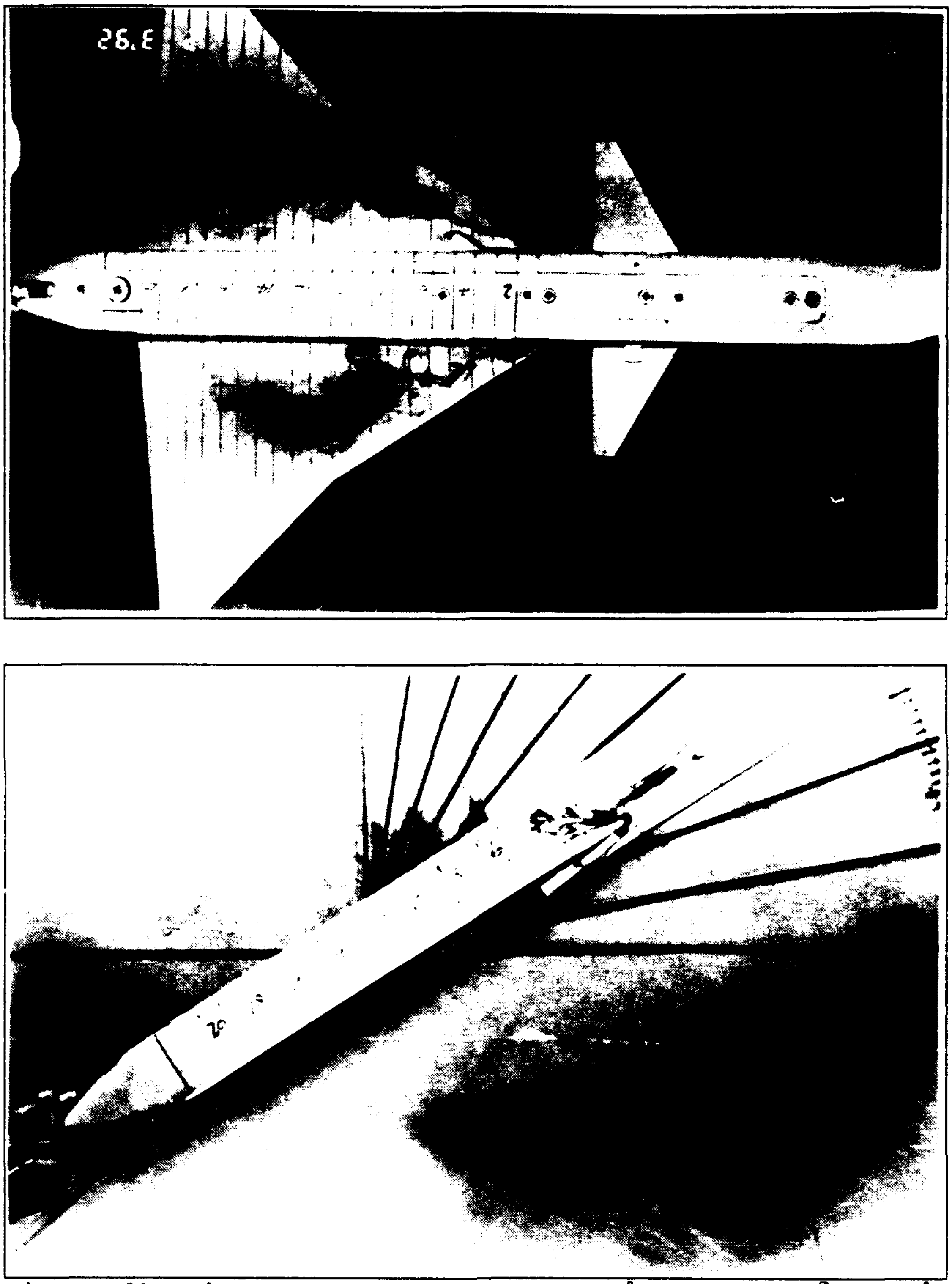

Figure 69. Wing Root Vortex Flow, $\alpha=30^{\circ}$, $K=-0.08$, $\delta_a=+/-5^{\circ}$, $K_c=1.7$

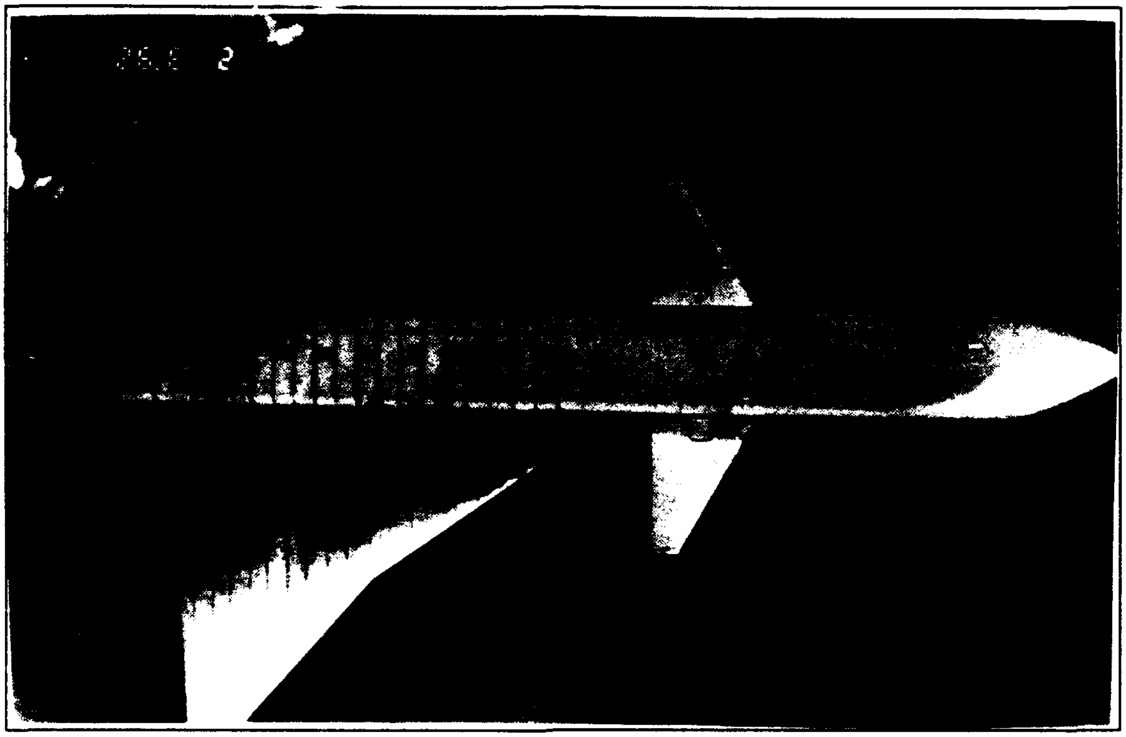

Figure 70. Wing Root Vortex Flow, $\alpha=40^{\circ}$, K=-0.16, $\delta_a=+/-5^{\circ}$, $K_c=1.7$

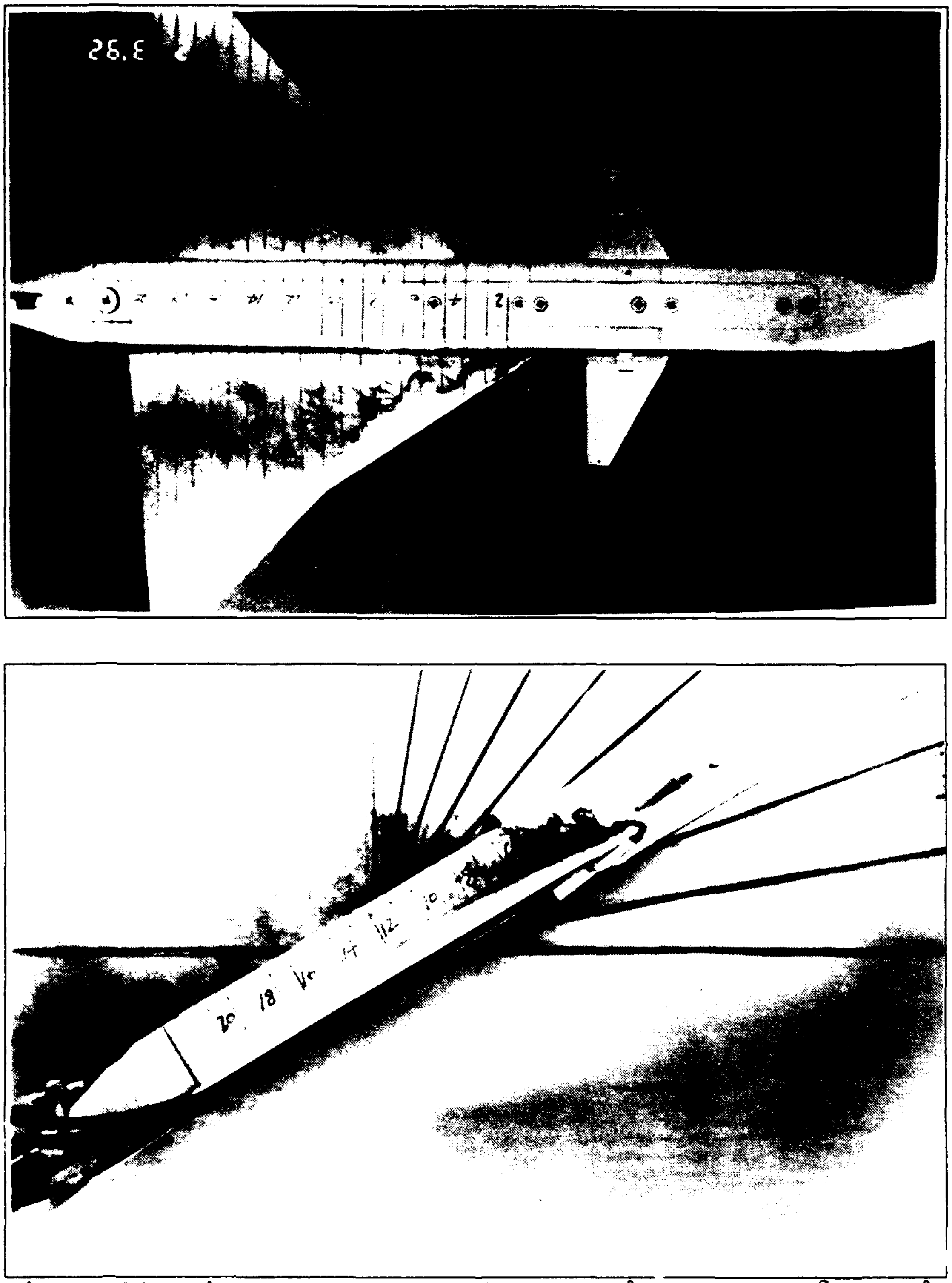

Figure 71. Wing Root Vortex Flow, $\alpha=30^\circ$, K=-0.16, $\delta_a=+/-5^\circ$, $K_c=1.7$

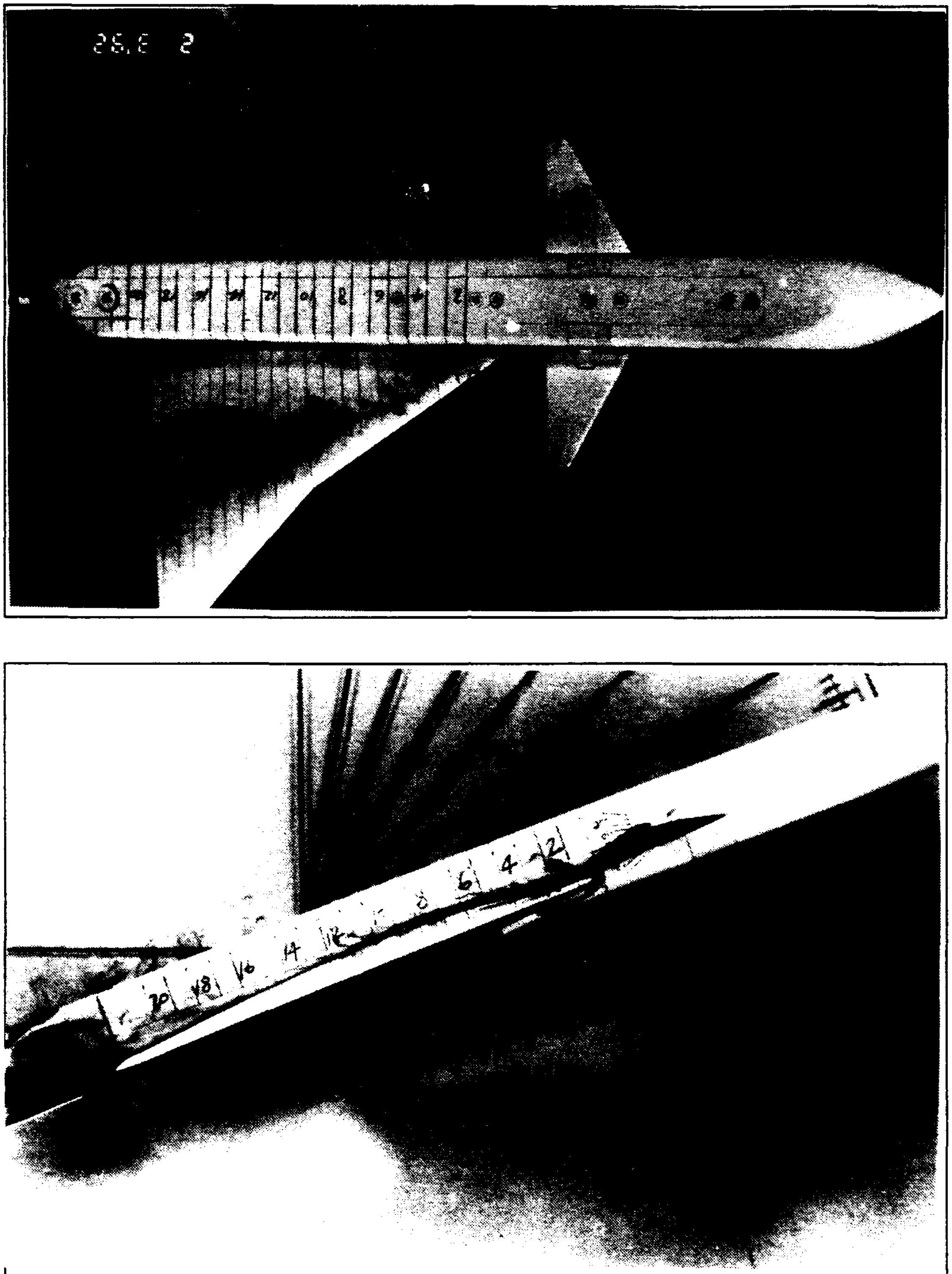

Figure 72. Wing Root Vortex Flow, $\alpha=20^{\circ}$, $K=0.08$, $\delta_a=+/-5^{\circ}$, $K_c=10.4$

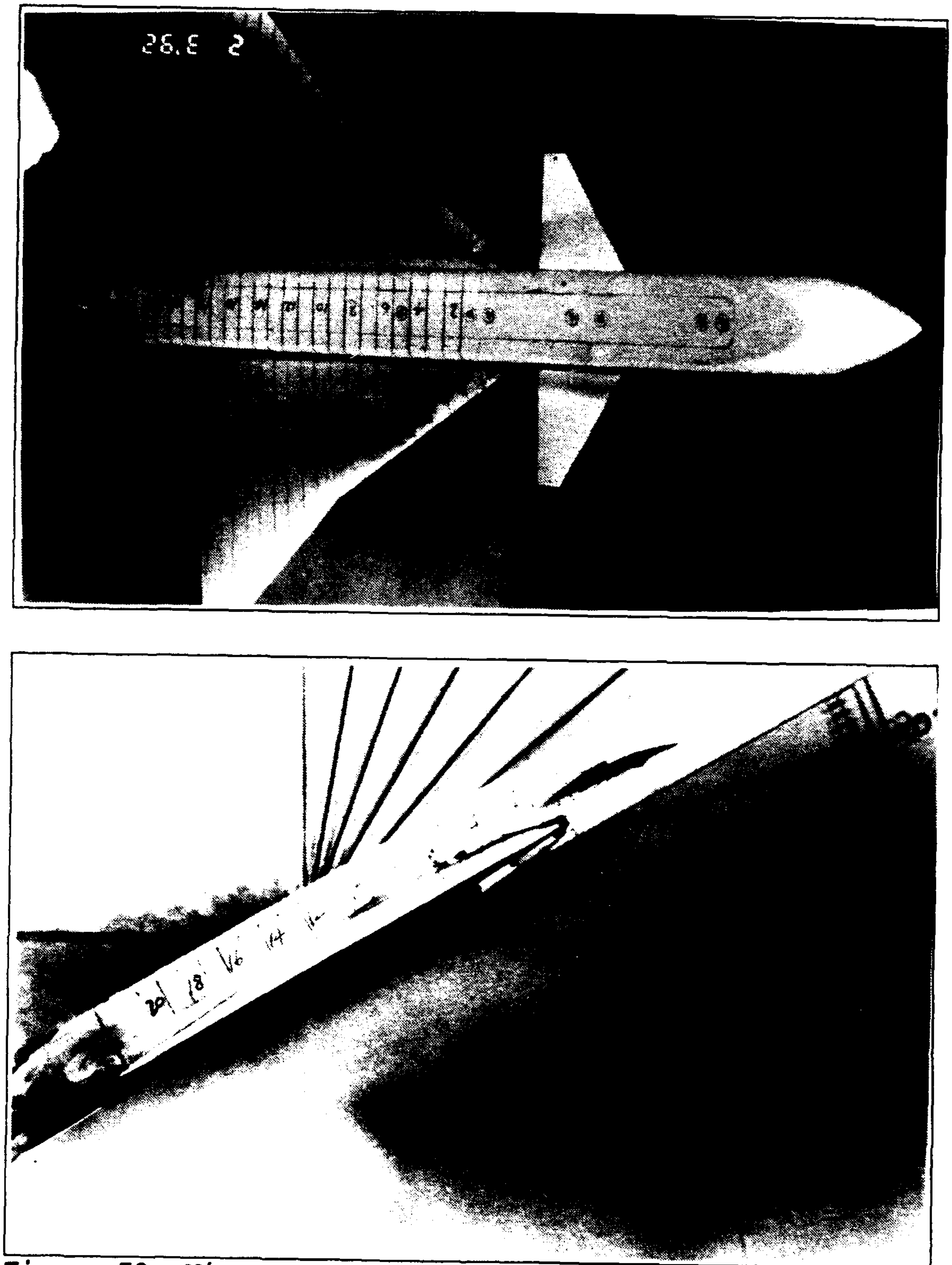

Figure 73. Wing Root Vortex Flow, $\alpha=30^{0}$, K=0.08, δ_a=+/-5°, K_C=10.4

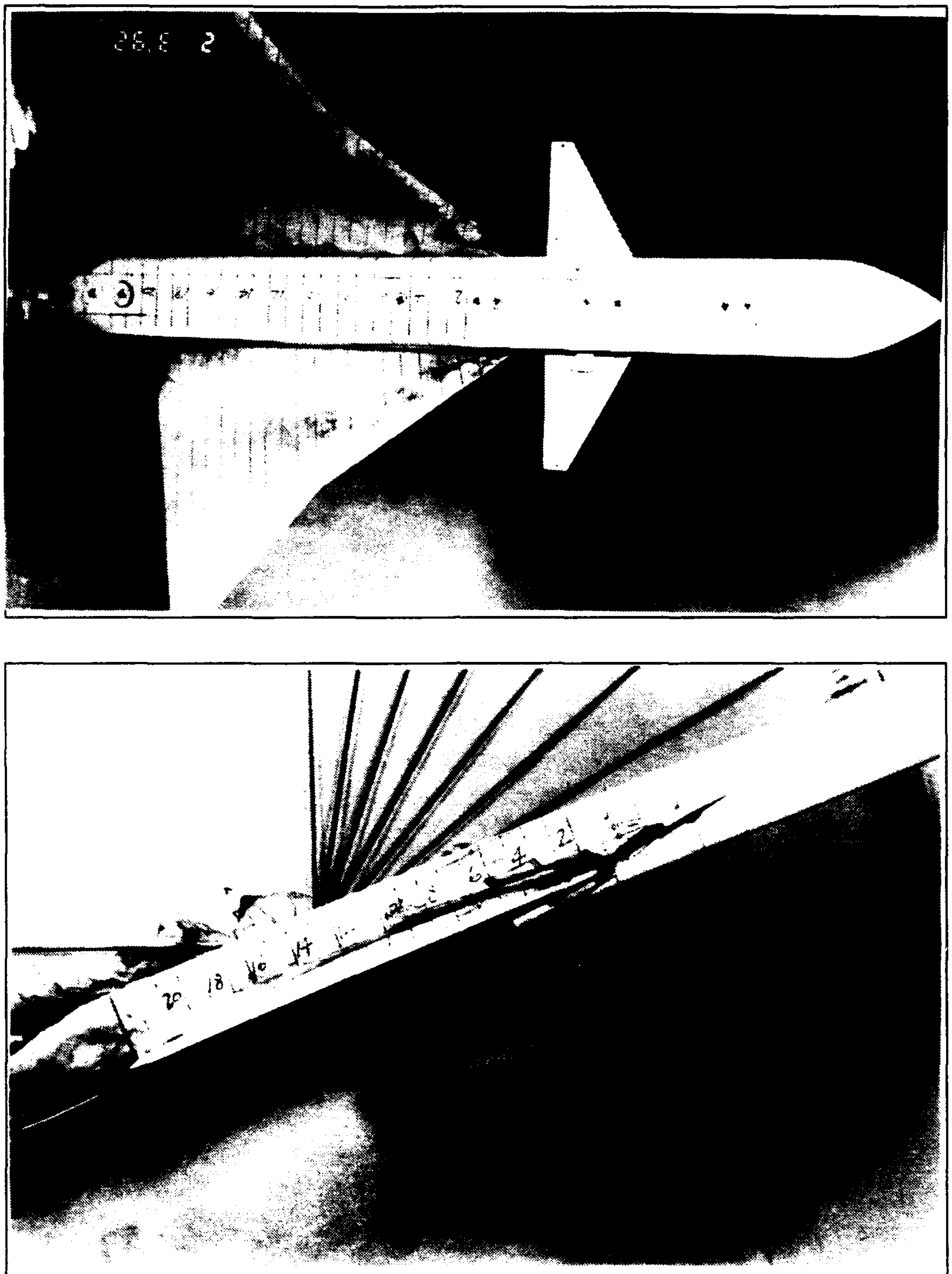

Figure 74. Wing Root Vortex Flow, $\alpha=20^\circ$, K=0.16, $\delta_a=+/-5^\circ$, $K_c=10.4$

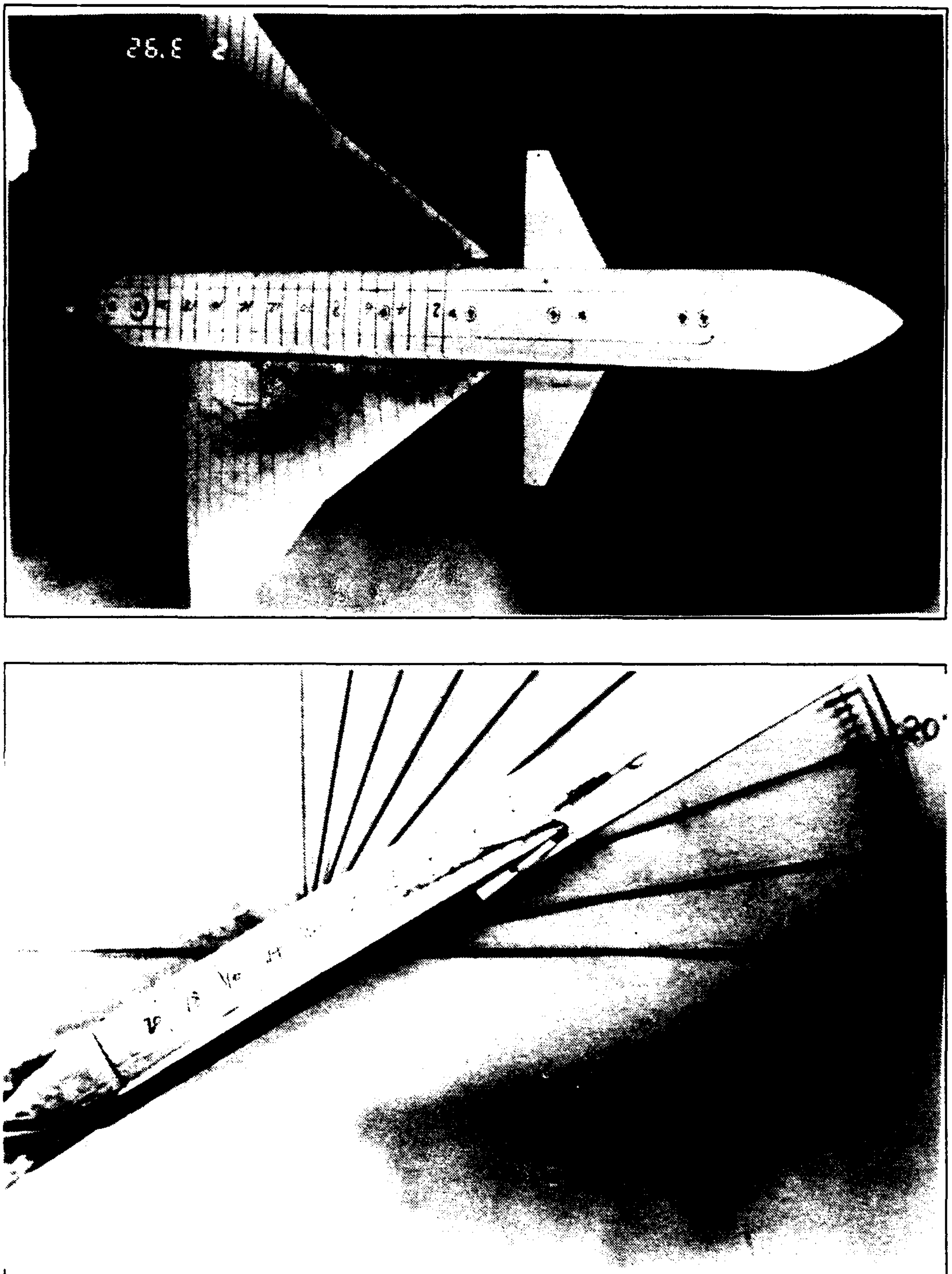

Figure 75. Wing Root Vortex Flow, $\alpha=30^0$, K=0.16, δ_a=+/-5^0, K_c=10.4

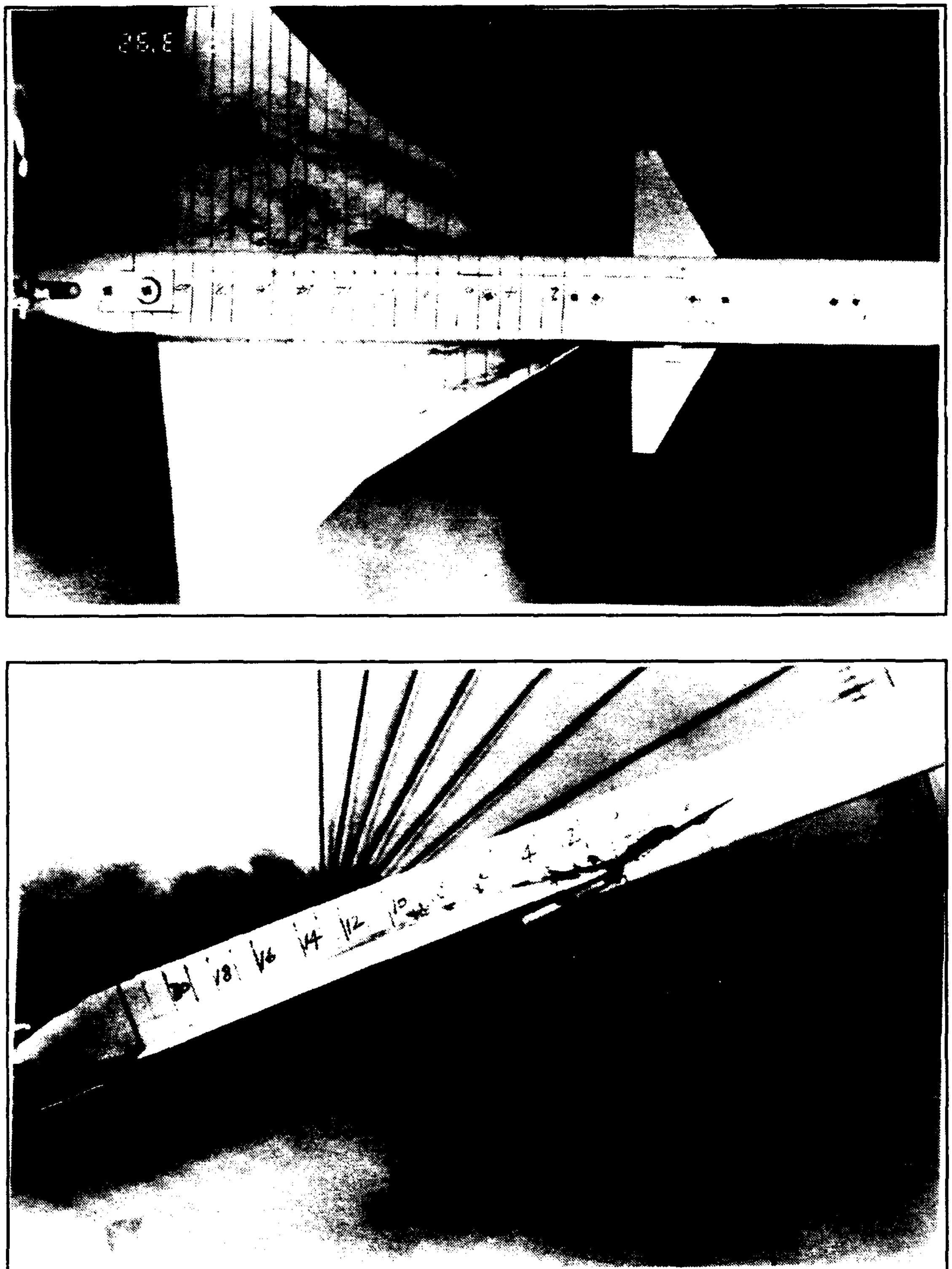

Figure 76. Wing Root Vortex Flow, $\alpha=20^0$, $K=-0.08$, $\delta_a=+/-5^0$, $K_C=10.4$

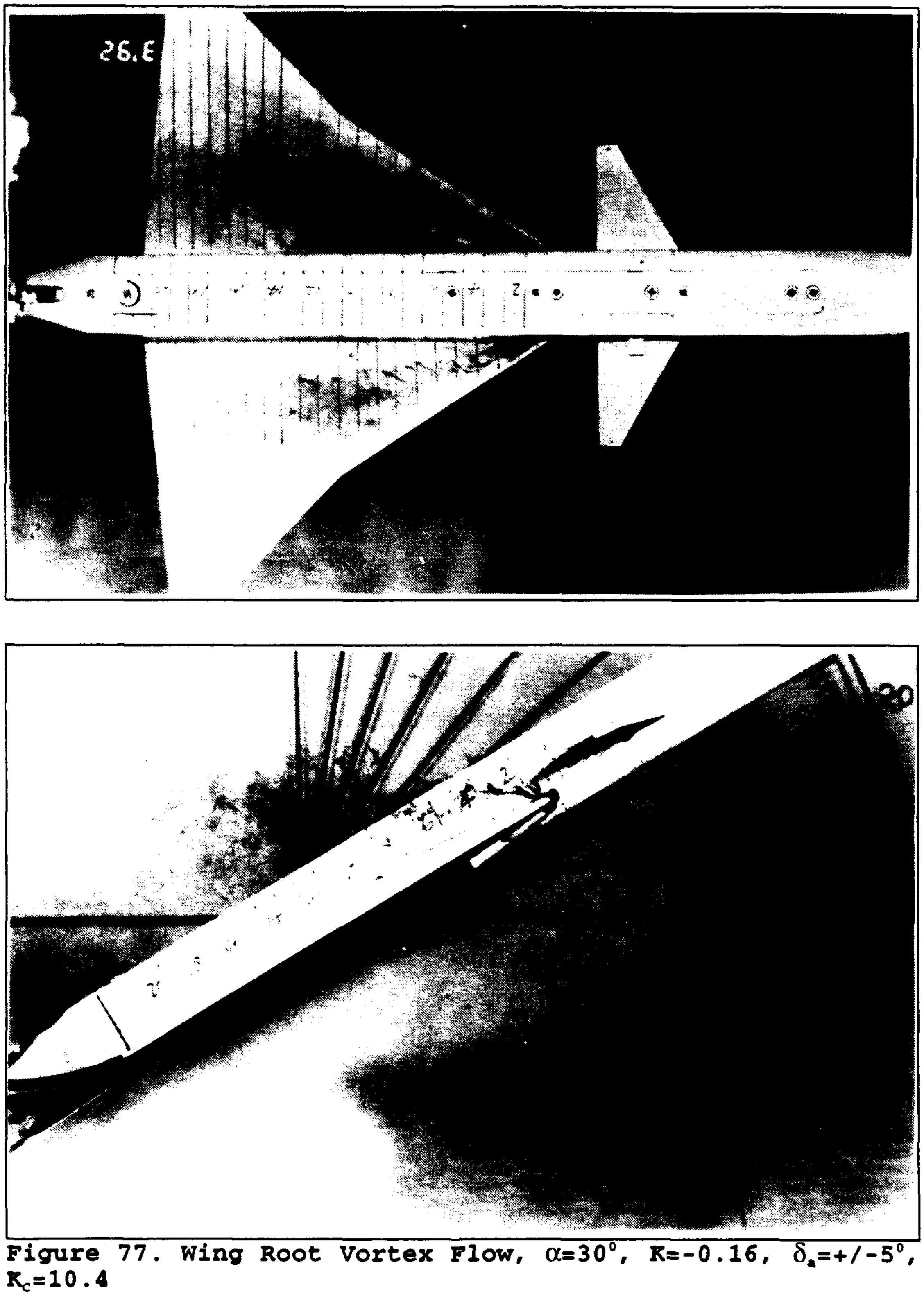

Figure 77. Wing Root Vortex Flow, $\alpha=30^{\circ}$, $K=-0.16$, $\delta_a=+/-5^{\circ}$, $K_c=10.4$

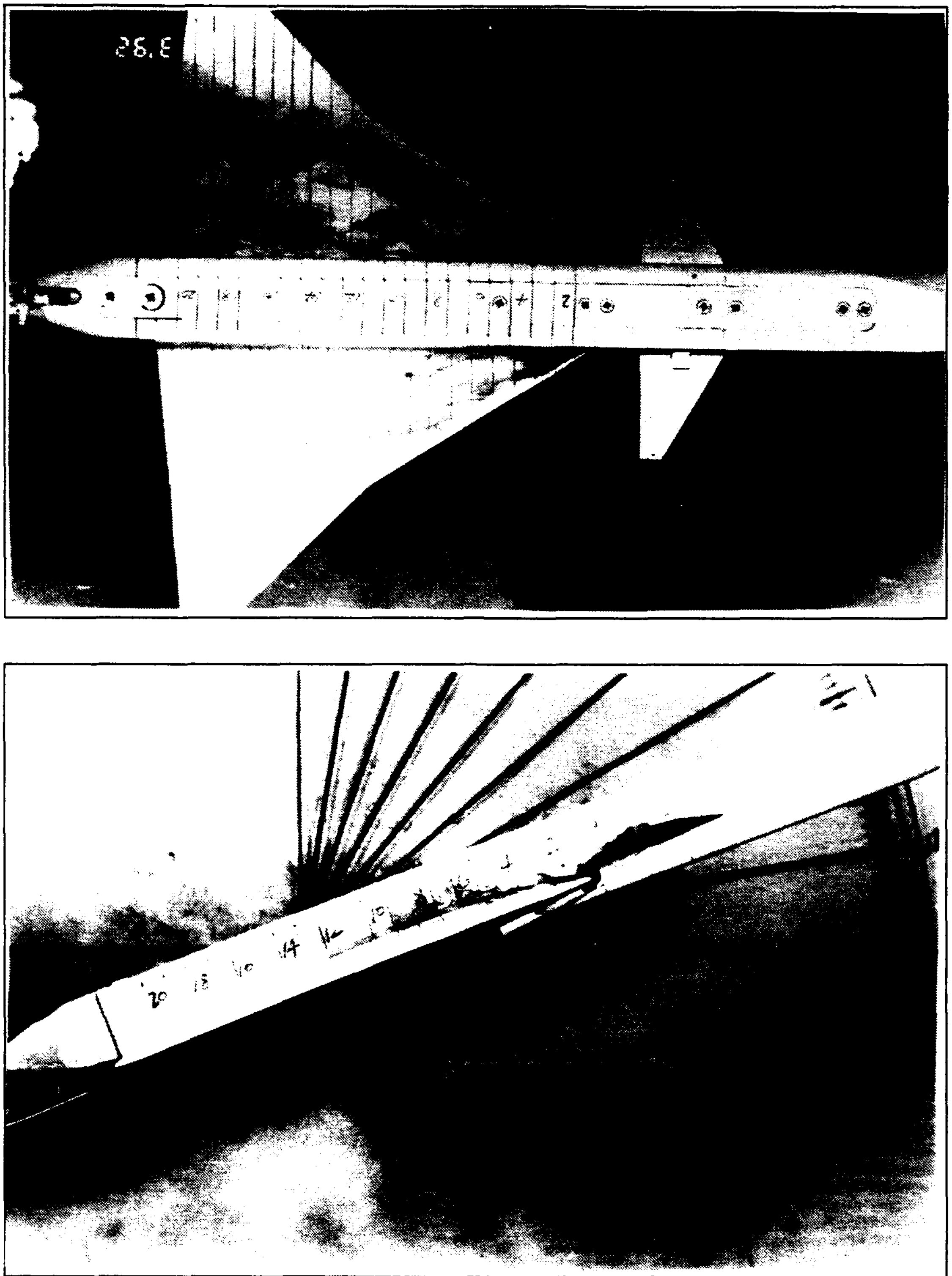

Figure 78. Wing Root Vortex Flow, α=20°, K=-0.16, δ_a=+/-5°, K_c=10.4

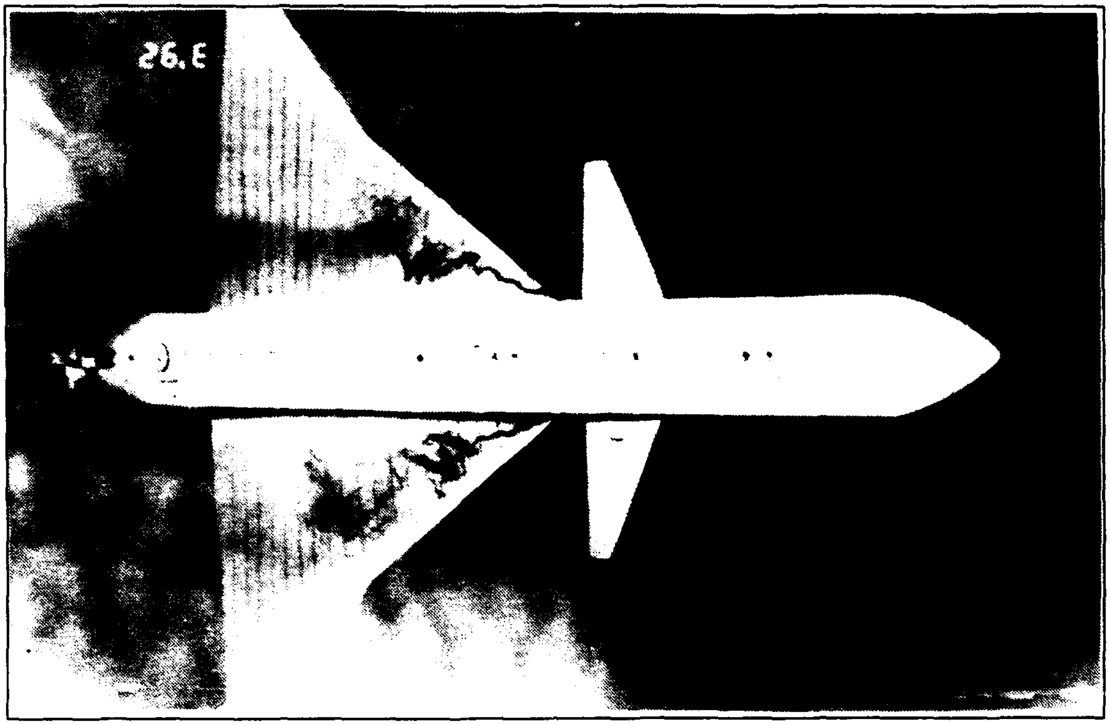

Figure 79. Wing Root Vortex Flow, $\alpha=30^{\circ}$, $K=0.16$, $\delta_a=+/-25^{\circ}$, $K_c=1.7$

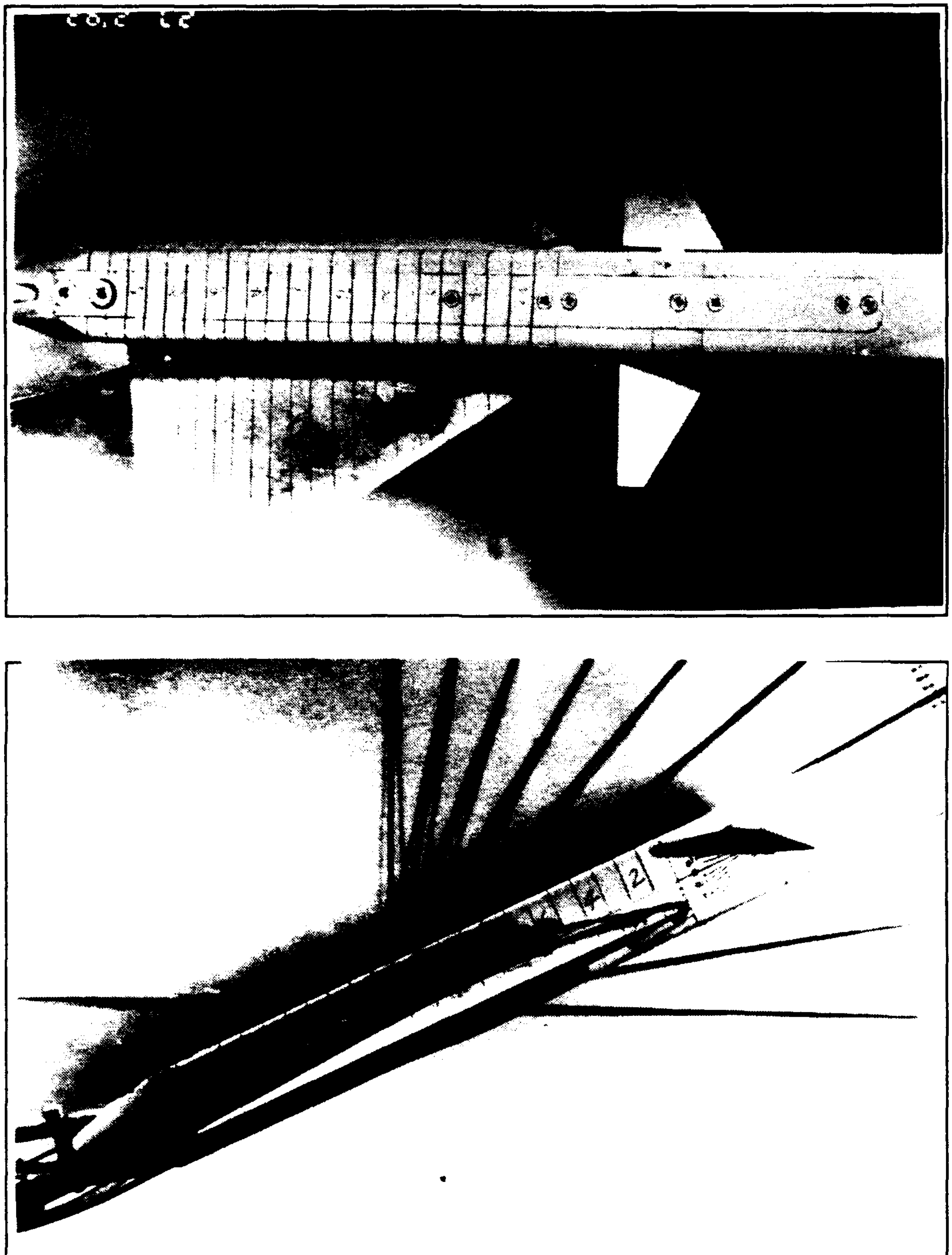

Figure 80. Wing Root Vortex Flow, $\alpha=20^0$, $K=-0.16$, $\delta_a=+/-25^0$, $K_C=1.7$

APPENDIX C. EXPERIMENTAL RESULTS (GRAPHS)

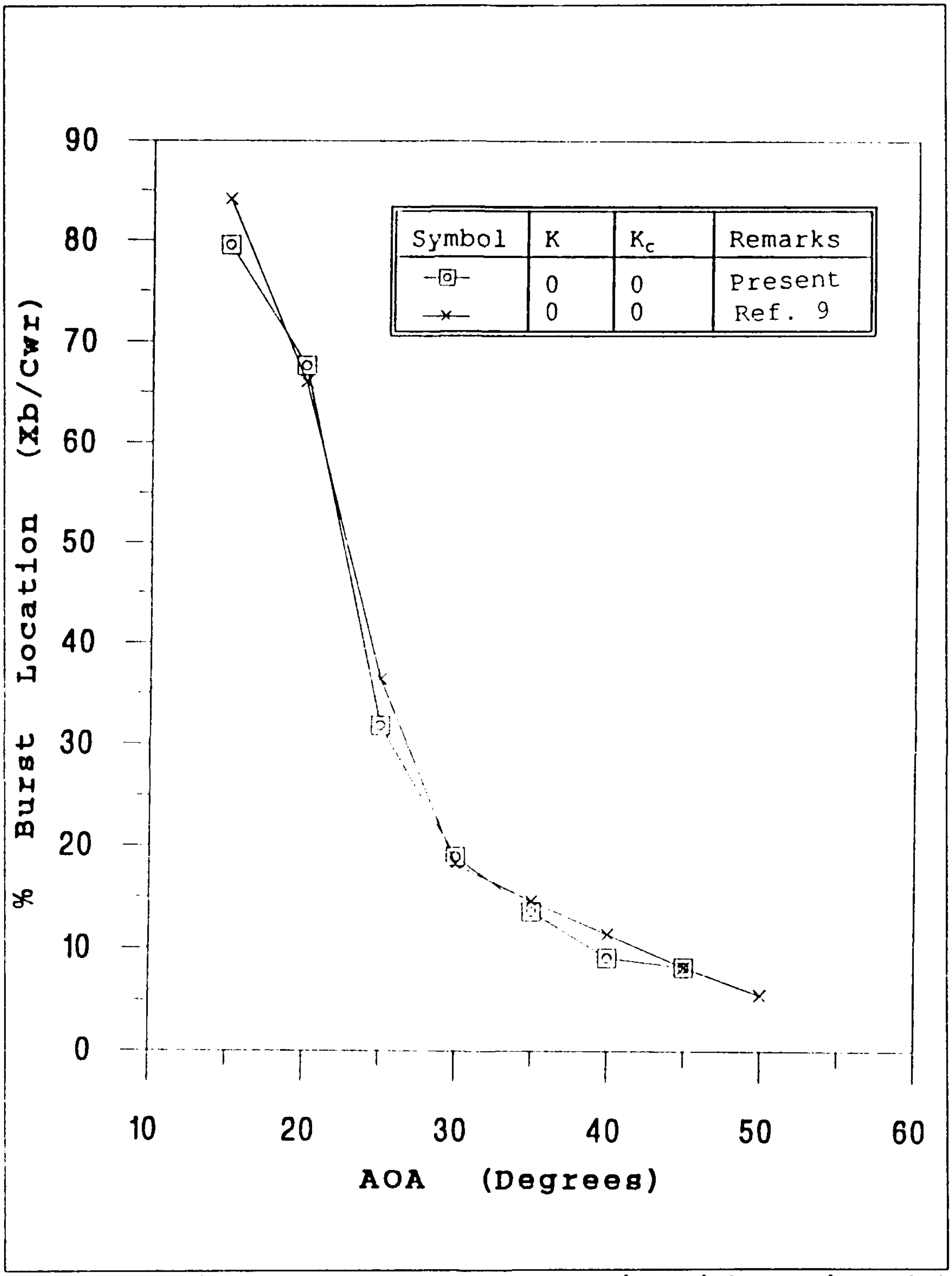

Figure 81. Wing Root Vortex Burst Location with Static Model and Static Canard at $\delta=0°$

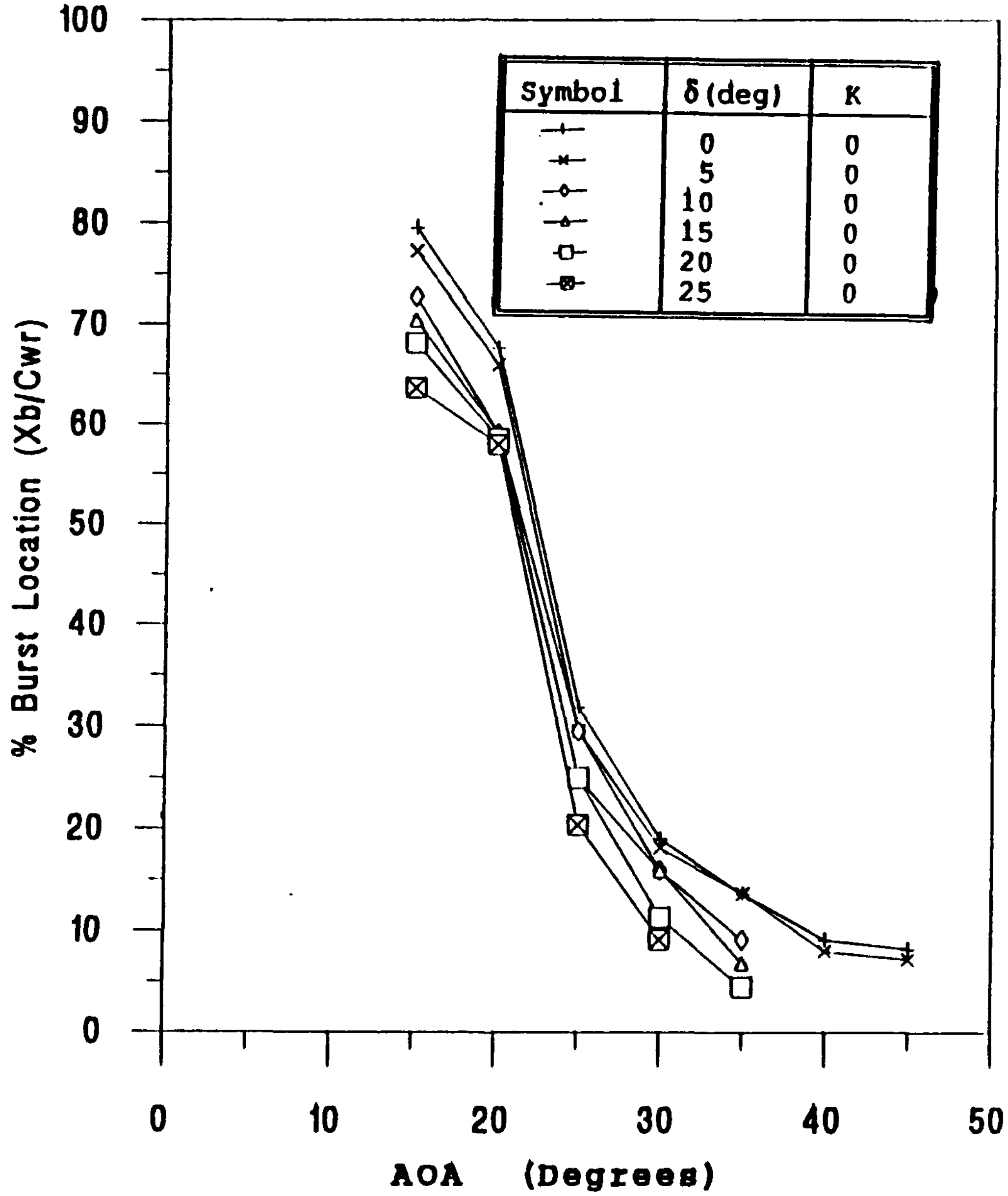

Figure 82. Wing Root Vortex Burst Location with Static Model and Static Canard

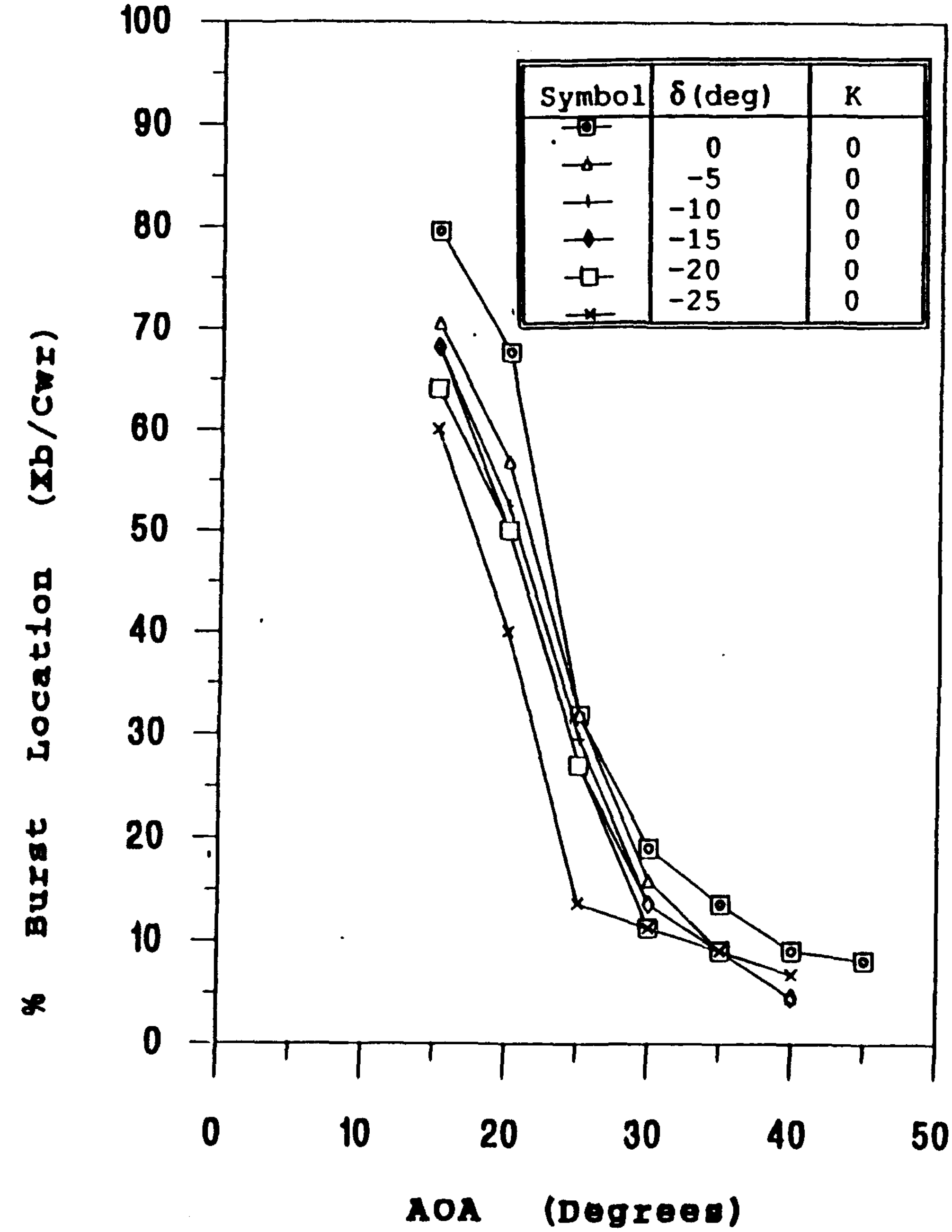

Figure 83. Wing Root Vortex Burst Location with Static Model And Canard

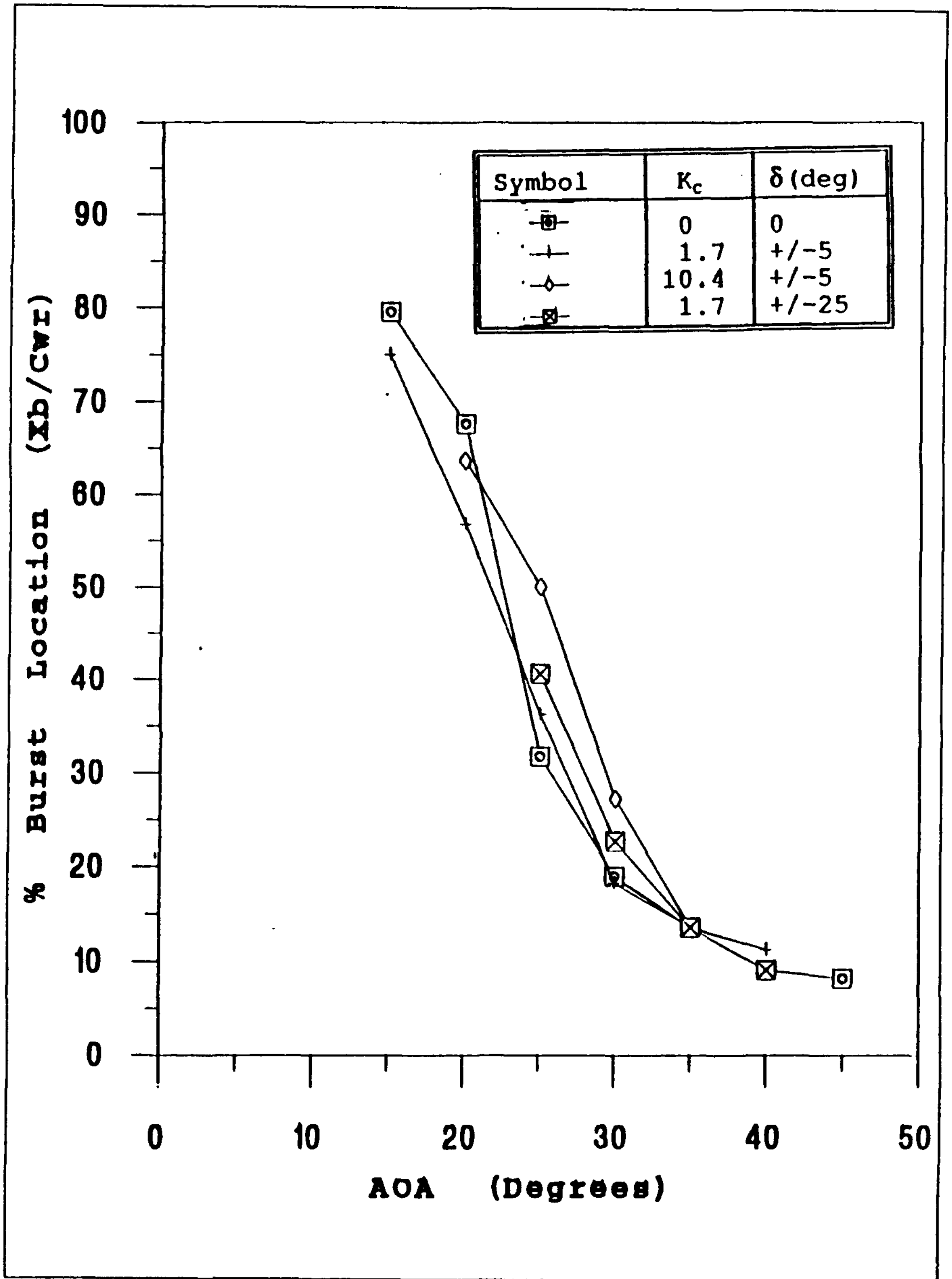

Figure 84. Wing Root Vortex Burst Loaction at $\delta=0^{\circ}$, K=0 with Oscillating Canard

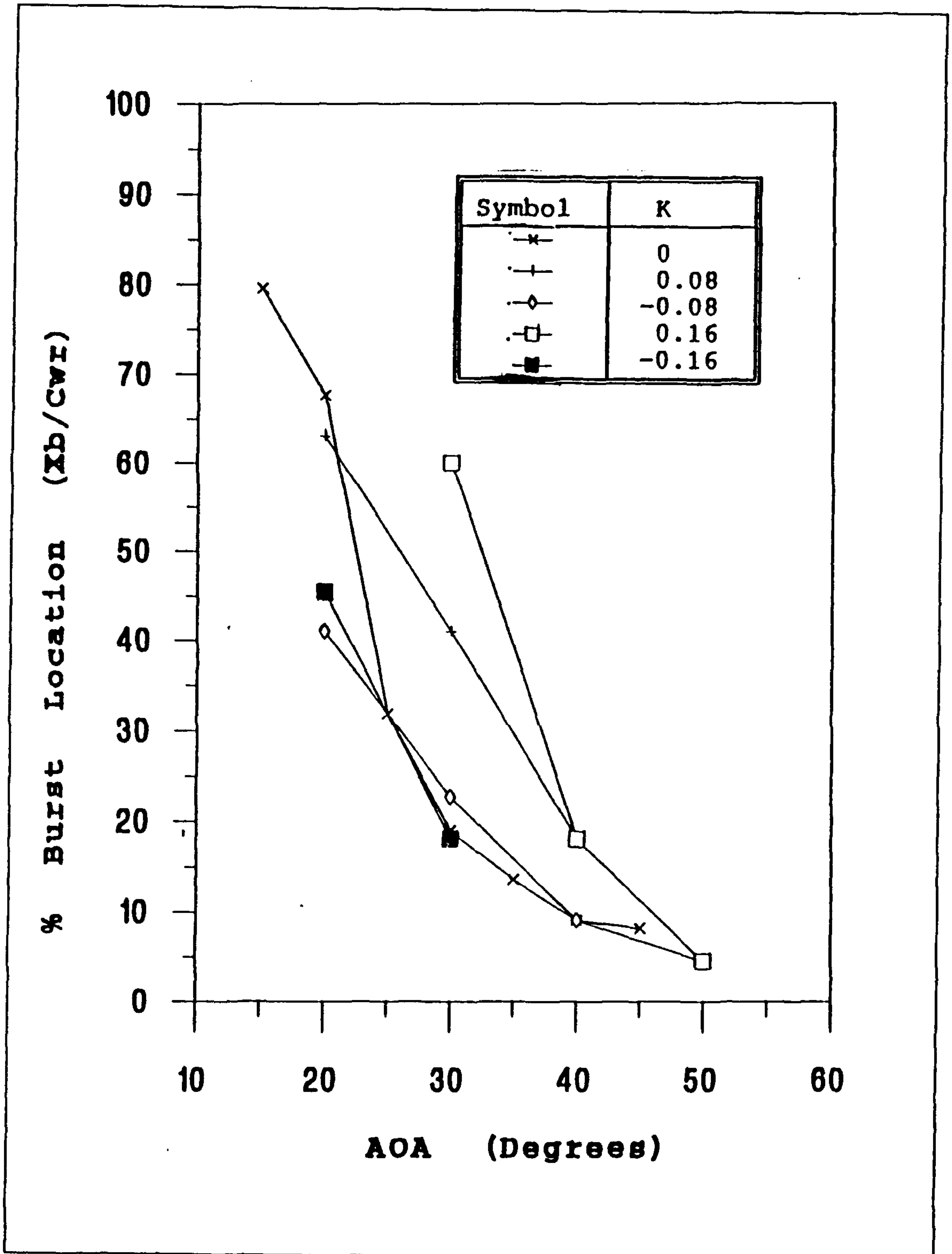

Figure 85. Wing Root Vortex Burst Location with Pitching Model and Static Canard ($\delta=0°$)

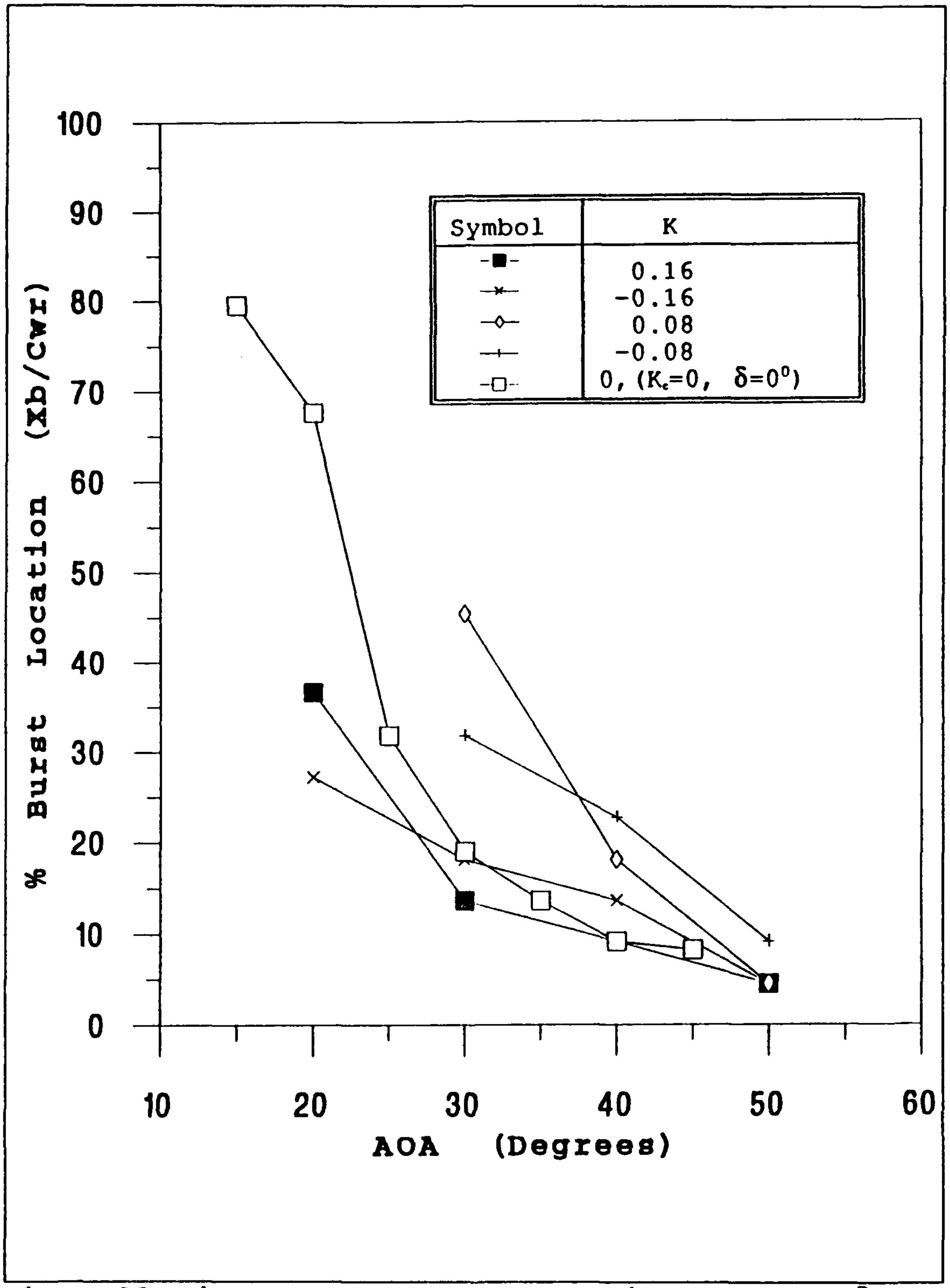

Figure 86. Wing Root Vortex Burst Location at K_c=1.7, δ_a=+/-5° with Pitching Model

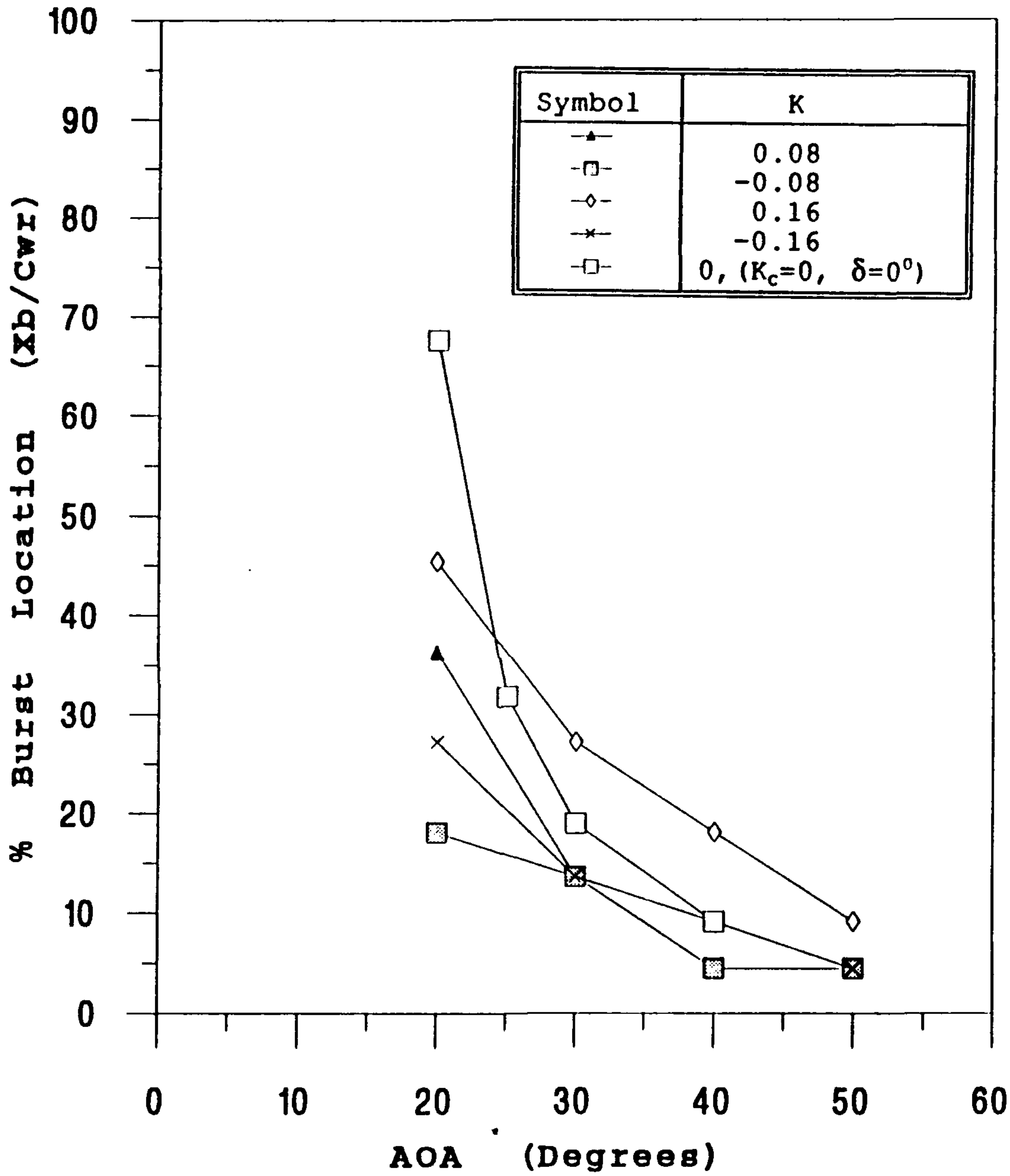

Figure 87. Wing Root Burst Vortex Location at K_c=10.4, δ_a=+/-5° with Pitching Model

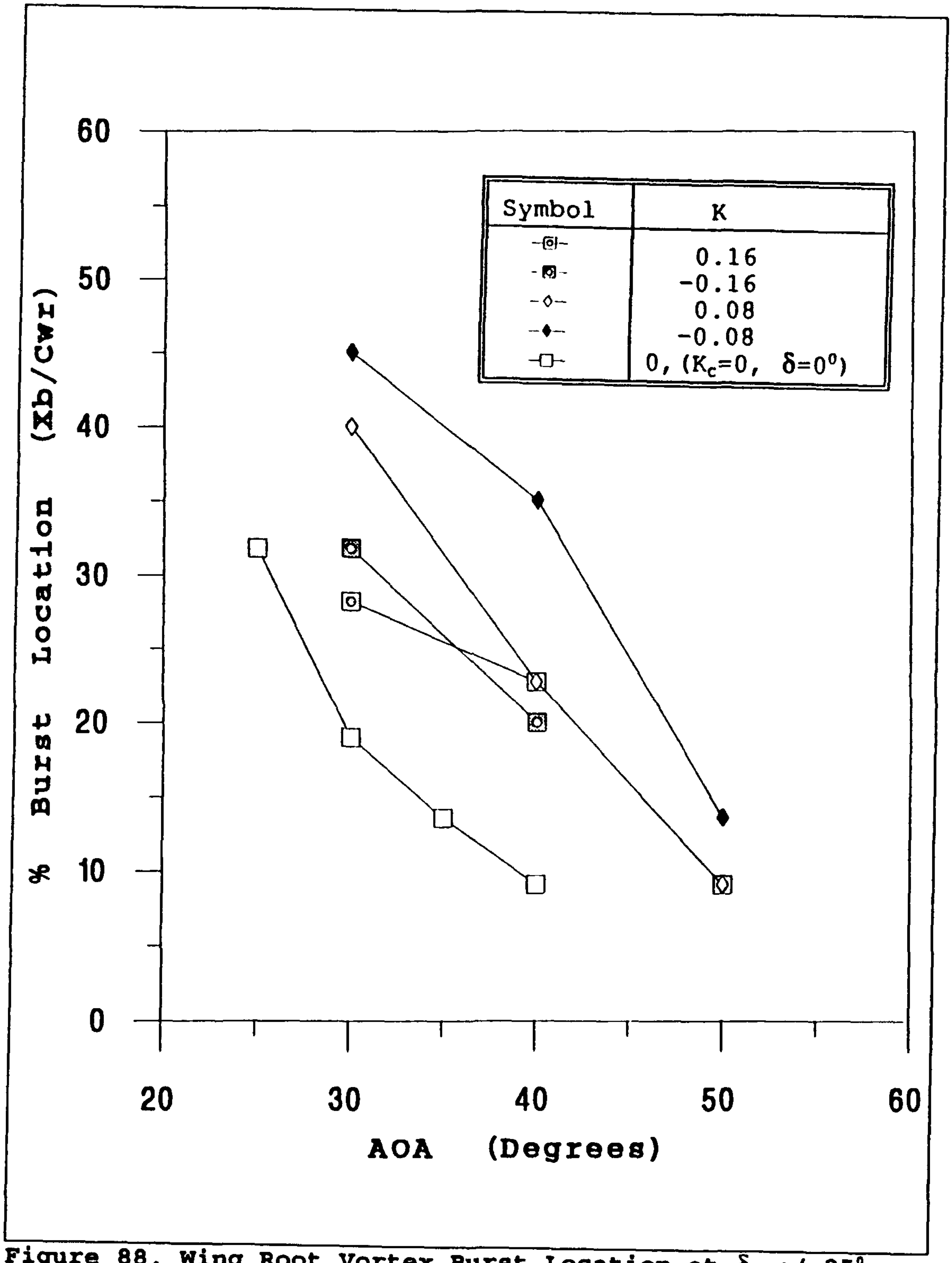

Figure 88. Wing Root Vortex Burst Location at δ_a=+/-25°, K_c=1.7 with Pitching Model

INITIAL DISTRIBUTION LIST

		No. of Copies
1.	Defense Techical Information Center Cameron Station Alexandria, VA 22304-6145	2
2.	Library, Code 52 Naval Postgraduate School Monterey, CA 93943-5000	2
3.	Chairman, Code AA/Co Naval Postgraduate School Monterey, CA 93943-5000	1
4.	Professor S.K. Hebbar, Code AA/Hb Naval Postgraduate School Monterey, CA 93943-5000	4
5.	Professor M.F. Platzer, Code AA/Pl Naval Postgraduate School Monterey, CA 93943-5000	1
6.	Liu, Da-Ming #19-1, Lane 119, Ho-Ping E. Road, Taipei, Taiwan Republic of China	2
7.	Naval Academy Library Tsoying, Kaoshiung, Taiwan, Republic of China	1
8.	Mr. Marvin Walters Naval Air Development Center Street Road, Warminster, PA 18974-5000	1
9.	Michael J. Harris Aircraft Division Code Air-913 Naval Air Systems Command	1

Washington, D.C. 20361-9320